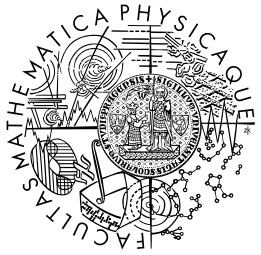

FACULTY
OF MATHEMATICS
AND PHYSICS
Charles University

DOCTORAL THESIS

Jiří Vackář

Automated determination of earthquake source parameters

Department of Geophysics

Supervisor of the doctoral thesis:	prof. RNDr. Jiří Zahradník, DrSc.
Study programme:	physics
Study branch:	geophysics

Prague 2017

I declare that I carried out this doctoral thesis independently, and only with the cited sources, literature and other professional sources.

I understand that my work relates to the rights and obligations under the Act No. 121/2000 Sb., the Copyright Act, as amended, in particular the fact that the Charles University has the right to conclude a license agreement on the use of this work as a school work pursuant to Section 60 subsection 1 of the Copyright Act.

In Prague date May 21, 2018 signature of the author

First of all, I would like to thank my supervisor, Prof. Jiří Zahradník, for his help, guidance, and patience, careful reading of the manuscript, and that he was always ready to discuss any particular problem. My special thanks belong to František Galovič and Jan Burjánek for many inspiring ideas and long discussions. I also thank to Jakub Velímský for his help with proof of equation 3.5.

I also thank all the teachers and students at the Department of Geophysics in Prague for creating friendly and inspiring atmosphere. All these years at the department have been a great pleasure. A lot of thanks also to my family, for their support and understanding during my study.

I want to thank all institutions as well as their employers who operates seismic networks. The research described in this thesis would not be conceivable without a large amount of high quality seismic data. Data used in this thesis are mostly from Switzerland [Swiss Seismological Service (SED) at ETH Zurich, 1983]. Other agencies that provide data that is archived at the SED and accessible for this study are: Geophysical Observatory Fürstenfeldbruck (Ludwig-Maximilians-University, Munich), GERESS (Hannover), GRSN/SZGRF (Erlangen), INGV/MEDNET (Rome), Landes-Erdbebendienst (Freiburg i. B.), OGS/CRS (Udine/Trieste), RENASS (Strasbourg), RSNI/DipTeris (Genova), SISMALP (Grenoble), SNRS (Ljubljana), TGRS (Nice), ZAMG (Vienna), UPSL (Patras; including 10 joint Patras-Prague stations), HUSN (Athens).

This research received funding from SCIEX Scholarship Fund and significant part of the work was done during my fellowship at ETH Zurich. Support from Charles University through projects GAUK-496213, SVV-2013-267308, and SVV 2014-260096 is thankfully acknowledged. This work was also supported by the Grant Agency of the Czech Republic through grants GAČR 210/11/0854 and GAČR 14-04372S.

Title: Automated determination of earthquake source parameters

Author: Jiří Vackář

Department: Department of Geophysics

Supervisor: prof. RNDr. Jiří Zahradník, DrSc., Department of Geophysics

Abstract: The thesis deals with methods for automated inversion of seismic source parameters. We studied the influence of structure model used and show an example how the existing model can be improved. We have developed a new, fully automated tool for the centroid moment tensor (CMT) inversion in a Bayesian framework. It includes automated data retrieval from ArcLink server or local data storage. Step-like disturbances are detected using modeling of the disturbance according to instrument parameters and such components are automatically excluded from further processing. Frequency ranges for the filtration and time windows for the inversion are determined automatically due to epicentral distance. Full-waveform inversion is performed in a space-time grid around a provided hypocenter. A data covariance matrix calculated from pre-event noise yields an automated weighting of the station recordings according to their noise levels and also serves as an automated frequency filter suppressing noisy frequency ranges. The method is tested on synthetic and observed data. It is applied on a dataset from the Swiss seismic network and the results are compared with the existing high-quality MT catalog. The software package programmed in Python is designed to be as versatile as possible in order to be applicable in various networks ranging from local to regional. The method can be applied either to the everyday network data flow, or to process large pre-existing earthquake catalogues and data sets.

Keywords: earthquake source observations, centroid moment tensor, inverse theory, full waveform inversion, automated data processing

Název práce: Automatizace určování zdrojových parametrů zemětřesení

Autor: Jiří Vackář

Katedra: Katedra geofyziky

Vedoucí disertační práce: prof. RNDr. Jiří Zahradník, DrSc., Katedra geofyziky

Abstrakt: Tato práce se zabývá metodami pro automatické určení parametrů seismického zdroje. Studovali jsme vliv použitého rychlostního modelu a ukazujeme příklad, jak tento model může být vylepšen pomocí naměřených dat. Vyvinuli jsme nový, zcela automatický nástroj pro určení momentového tenzoru v bayesovské formulaci. Tento nástroj zahrnuje automatické stahování dat z ArcLink serveru nebo načtení lokálně uložených dat. Jsou detekovány instrumentální poruchy a zasažené komponenty jsou automaticky vyloučeny z dalšího zpracování. Principem této detekce je modelování poruchy dle instrumentální odezvy přístroje a porovnání této modelované poruchy s naměřeným záznamem. Frekvenční rozsahy pro filtraci záznamů a časová okna pro inverzi jsou určována automaticky dle epicentrální vzdálenosti. Jádrem metody je inverze celých vlnových obrazů v prostoro-časové síti okolo zadaného hypocentra. V inverzi používáme kovarianční matici dat určenou z analýzy seismického šumu zaznamenaného před zemětřesením. Tato matice funguje jako vážení stanic dle úrovně jejich šumu a také jako automatický frekvenční filtr potlačující zašuměné frekvence. Metoda je v dizertaci testována jak na syntetických, tak na reálných datech. Je aplikována na data ze švýcarské seismické sítě (Swiss Digital Seismic Network) a její výsledky jsou porovnány s existujícím katalogem momentových tenzorů. Metoda je naprogramována v programovacím jazyku Python, s důrazem na co největší univerzalitu, aby byla použitelná v rozličných seismických sítích od lokálních po regionální. Metoda může být použita jak na aktuálně měřená data v reálném čase, tak na zpracování již naměřených dat a katalogů zemětřesení z minulosti.

Klíčová slova: studium ohniska zemětřesení, momentový tenzor, teorie obrácených úloh, inverze celých vlnových obrazů, automatické zpracování dat

Contents

Introduction

An earthquake is a very complex process and there are various types of them. The most common one, a tectonic earthquake, occurs where stress exceeds strength on an existing fault or is high enough to create a new fault. It results in a dominantly shear movement on the fault segment which locally decreases the stress level. The movement might be very fast and the entire process happens within a few seconds (or minutes for the largest events), resulting in an earthquake. The relaxation of stressed material releases energy, which is not only dissipated in the rupturing process, but also radiated as seismic waves. If the movement is slower (in order from minutes to years), seismic wave radiation is weaker or none, and the process is called slow slip or creep.

Special types of earthquakes are related to fluids, which can open cracks themselves, or their pressure can decrease a critical stress level to facilitate the rupturing start. There are plenty of types of seismicity connected to fluids, e.g. shallow earthquakes in geothermal regions, magma channels related seismicity in volcanic areas, and fluid injections in hydraulic fracturing. There are also earthquakes caused by explosions and implosions. The explosions are usually of antropogenic origin, the implosions are usually related to collapses of caves and mines or collapses of explosion generated cavities. Seismic waves can be also radiated by landslides, meteorite impacts, dam collapses etc. There are some other sources of seismic waves which are continuously present in the seismic records, all together called "seismic noise". Its sources are, e.g., oceanic waves interacting with the crust and wind, as well as sources of antropogenic origin like traffic, heavy industry etc.

The study of an earthquake source process is complicated by fact that almost never we have direct observation of faulting and often we have only surface recordings of ground motion at a few places. Recently, geodetic observations of the static displacements caused by (strong) earthquakes become also common. It is not possible to describe the rupturing process in all its complexity from this limited amount of data, so some simplifications always must be adopted.

Centroid moment tensor

Focal mechanisms of earthquakes are important for understanding physics of individual seismic events, and for studying seismotectonics of a region; they also serve as a basic input for seismic hazard assessment. Usually, the point source approximation and the moment tensor (MT) are used. Then we have to find 6 components of the moment tensor, 3 space coordinates of the centroid, and the centroid time, all together called the centroid-moment-tensor (CMT) solution.

Many methods have been proposed for CMT solutions (e.g. Bernardi et al. [2004], Cesca et al. [2010], E. and S. [2000], Liu et al. [2004], Pondrelli et al. [2002], Rueda and Mézcua [2005], and Scognamiglio et al. [2009] for more details, see the next section). They differ in ability to provide automatic solutions and they include consideration of the solution uncertainty to varying degrees. In this thesis we develop a method suitable for highly automated processing of individual events, that can handle both real time and off-line processing. We follow the

Bayesian approach to treat rigorously the uncertainty of the inversion.

In general, CMT determination using broadband waveforms is a non-linear inverse problem. Alternatively, a linear inverse problem can be solved just for MT components, assuming that the centroid position, centroid time, and source time function are known, using, for example, hypocenter parameters from an earthquake catalogue. The applicability of the latter simplification is highly limited, hence it is not applied here. In this work, we search the centroid position and time on a regular grid, while the MT is obtained in every space-time grid point by the linear least-squares method, i.e. analytically with minimal computational costs. The solutions from all grid points are then combined by the Bayesian approach. This combination of analytical solution and grid search, we call 'hybrid approach', enables to obtain solution of the non-linear 10-parameter inverse problem by a grid search in 4-dimensional parameter space. Compared to stochastic algorithms, we have full control over the density of the (space and time) sampling.

CMT uncertainty

The CMT determination should be accompanied by an assessment of its uncertainty, which defines a region in the model space containing the true solution with certain probability. The sources of uncertainty in a MT determination are: signals present in the waveforms generated by all other sources than the earthquake of interest (seismic noise and other seismic events), lack of knowledge of the Earth structure (Green's function modeling error), limited number of seismic recordings and/or their unfavorable spatial distribution, measuring errors (instrument noise) and possible instrument malfunction [Vackář et al., 2015], and assumptions used in the mathematical description of the earthquake source (point source approximation, fixed source time function etc.) If any of these aspects is ignored, the uncertainty evaluation may be biased.

Existing methods for estimating the CMT uncertainty reflect many of these aspects. They include, for example, construction of confidence regions by global search algorithms [Šílený, 1998], bootstrap and jackknifing techniques [Tichelaar and Ruff, 1989], calculation of various stability measures [Sokos and Zahradník, 2013], adding noise to real data [Vavryčuk, 2011], and using covariance matrix of the data, which is discussed below.

The uncertainty of the MT in the linear case, assuming Gaussian error distribution, can be described by a 6-D error ellipsoid [Zahradník and Custódio, 2012]. Křížová et al. [2013] show how to extend this approach to a non-linear inversion including source depth and time. Particularly important are the methods developed in a general framework of Bayesian formulation, where the solution of the inverse problem is given by the posterior probability density function (PPDF) of model parameters [Minson et al., 2013; Tarantola, 2005]. Examples of application of Bayesian approach to seismic source inversion are still rather rare. They include Wéber [2006] who applied such an approach to local CMT and its source time function, Dettmer et al. [2007] to sound velocity profiles, Duputel et al. [2012a] to CMT from W-phase, and Dettmer et al. [2014] to finite fault inversions. Stähler and Sigloch [2014, 2016] published fully Bayesian framework for inversion of earthquake depth, MT and source time function, including novel

misfit criterion called signal decorrelation.

Data covariance matrix

A key role in the Bayesian inversion is played by data and modeling covariance matrices, which quantify measurement and theory errors. In the Bayesian formulation, measurement (or data) errors come from uncertainties in the measurement, in case of CMT inversion they contain mainly seismic and instrument noise. Theory (or modeling) errors comes from imperfect modeling of physical reality, in our case they contain Green's function modeling error and simplifications in source description (point source etc.) For example, Duputel et al. [2012a] reflected in the covariance matrix the centroid location uncertainty (theory error) and the effect of an oversampled record by describing correlation of samples as an exponentially decaying function. Wéber [2006] generated synthetic seismograms for several reasonable velocity models and used their variance as an estimate of modeling error. Dettmer et al. [2007] estimated the data covariance matrix iteratively from data residuals. Bodin et al. [2012] and Dettmer et al. [2012] used hierarchical estimation of data covariance matrix, where the level of noise is considered as unknown hyperparameter. Hierarchical (parametric) approaches include error statistics in the inversion and are particularly attractive for trans-dimensional inversions, where the number of model parameters (called hyperparameter) is also inverted. Mustać and Tkalčić [2016] used the hierarchical Bayesian approach with a data covariance matrix based on a before-event-noise correlation function. Hallo and Gallovič [2016] developed a method to reflect the uncertainty of the velocity model in the data covariance matrix.

We follow a similar approach as Duputel et al. [2012a] and Mustać and Tkalčić [2016], but contrary to them, we do not normalize the covariance function amplitude. We include the estimated noise covariance function directly in the data covariance matrix, making the procedure simpler. The data covariance matrix then serves as an automated station weighting according to the noise level and it can also reflect directionality of the seismic noise and its correlation between components of the seismic station. Mustać and Tkalčić [ibid.] used Markov chain Monte Carlo method to solve for the PPDF problem, while we use a combination of grid-search with analytical solution, which makes the procedure faster.

Codes for automated CMT solution

There are a few services providing automated CMT solutions on a global scale, e.g. the Global Centroid Moment Tensor project (Global CMT, Ekström et al. [2012], `http://www.globalcmt.org/`), the U.S. Geological Survey (USGS, using W-phase inversion by Duputel et al. [2012b], `https://earthquake.usgs.gov/earthquakes/map/`), GEOFON (Bormann [2012], `http://geofon.gfz-potsdam.de/eqinfo/list.php?mode=mt`), and GEOSCOPE (using SCARDEC method, Vallée et al. [2011], `http://geoscope.ipgp.fr/index.php/en/`). These solutions are calculated mostly from teleseismic waves and are avalaible for magnitudes $M_W > 5.5$.

Over last decades, significant progress was done in methods and tools for

automated and near real-time CMT solutions in regional distances. Many of these tools are optimized for a specific region and some of them are or were used for creating a catalog of automated CMT solutions, e.g. Dreger [2003], whose method TDMT_INV was applied by many others worldwide. Similarly, Braunmiller et al. [2002] for European–Mediterranean region and Switzerland, Bernardi et al. [2004] for similar regions as the previous one, Rueda and Mézcua [2005] for Spain, Nakano et al. [2008] inverted CMT and source time function (STF) simultaneously for Indonesian earthquakes, Scognamiglio et al. [2009] for Italy, Cesca et al. [2010], who applied multi-step approach for Greece and NW Europe, Lee et al. [2013] for Taiwan, and Jian et al. [2018] also for Taiwan.

Triantafyllis et al. [2016] introduced SCISOLA code, a tool for real-time MT solutions, which can be run as a SeisComP3 module, and uses ISOLA code [Sokos and Zahradník, 2013] as a back-end.

Novel approaches to CMT solutions were discovered, e.g. using GPS displacement together with broad-band records [Käufl et al., 2015, and referenced therein] or using 3-D spectral element for pre-calculating Green's functions [Liu et al., 2004, applied in California]. As far as we know, none of the previously mentioned methods uses Bayesian approach.

Recently, a few methods for probabilistic CMT solutions were published. Stähler and Sigloch [2014, 2016] is focused on teleseismic events and obtaining STF. Lee et al. [2011] applied an automated and Bayesian method to Southern California, using pre-calculated 3-D Green's functions.

Aim of the thesis

Our intention is to contribute to automated processing of seismic data. The main aim of this thesis is to develop a Bayesian method for the CMT solution as well as introducing an open-source code ISOLA-ObsPy that solves the problem automatically with relatively low computational costs. Instead of extending ISOLA by these features and using it as a back-end, we have taken the opportunity to re-write the core of the inversion from scratch with improved computational efficiency and a more versatile code.

We assume that the seismic noise is the most important source of errors. Typically, this is a case encountered in low-frequency inversions of data with low signal-to-noise ratios. In our method, the noise enters the inversion process via covariance matrix.

Besides the main topic we also deal with two related problems—that of a suitable velocity model and instrumental disturbances.

Structure of the thesis

The thesis is structured as follows. In Chapters 1 and 2, we deal with velocity models which are necessary for meaningful earthquake source inversion. We studied fast long-period seismic waves, which could not be simulated in any of published velocity models, and explained them in terms of leaking modes. These two chapters are just loosely connected to the rest of the thesis. Nevertheless, we included them because they reflect evolution of our ideas during the PhD study.

Then (Chapter 3), we describe the Bayesian formulation of the CMT problem. We also derive a method to calculate marginal probability density of any combination of model parameters (including non-linear combinations). In Chapter 4 we describe some sources of error and how we can deal with such problems. Then (Chapter 5), we study a step-like instrumental disturbance in detail. In Chapter 6, we construct the data covariance matrix from the before-event noise and show how to visualize the effects of the data covariance matrix. Using methods described in four previous chapters, we introduce the code for fully automated CMT inversion in Chapter 7, including technical aspects of the developed code. In the first part of Chapter 8, we show the ability of the new method to improve the CMT estimates by means of a few synthetic tests. We show how the uncertainty of the inverse problem is influenced by the noise level and by the number of stations, and demonstrate the usefulness of the method in case of various noise level across the stations and in case of colored noise at all stations. In the second part of the chapter, we test our method on real data from the Swiss Digital Seismic Network and compare the results with the moment tensor catalog created manually by the author of this thesis using the SeisComP3 scmtv module. Finally (Chapter 9), we briefly describe outlook how the developed method can be extended to be even more versatile.

The main results of the work were published as three papers. The first of them, in chronological order, [Vackář et al., 2014] is reprinted as Chapter 2. The second one [Vackář et al., 2015] is included as Chapter 5. The most recent one [Vackář et al., 2017] covers most of topics of the thesis, so it is split into corresponding chapters, creating main parts of Chapters 3, 6, and 8. These chapters include not only the text published in the paper, but they are extended also by some additional texts, derivations, formulas, and tests.

1. Velocity models and their possible improvements

A velocity model is needed for any seismic source study. It is because we rarely have direct observation of the source, so we are dependent on information carried by seismic waves, whose propagation is strongly dependent on the velocity structure. The knowledge of the Earth structure is still improving and we have more detailed and more accurate velocity models both on global scale as well as in many regions. But there are plenty of regions, where the knowledge remains poor.

The Earth structure is heterogeneous on all scales from molecular to the main geological units. There are two main groups of velocity models: 3-D and 1-D. The 3-D models reflect both vertical and horizontal variability of the velocity, but the resolution is always limited, because we have just finite amount of data used for creation of the model. Moreover, the 3-D models usually use smooth gradient between discretization points, so they do not reflect existing fast variations along geologic discontinuities. The 1-D models neglect horizontal heterogeneity approximating real structure just by a few horizontal layers with constant velocity or its vertical gradient. So that every velocity model is just a simple approximation of complex reality. The usability of every model has a high-frequency limit, where the modeled and observed seismic waves start to differ significantly.

The velocity model is often a limiting factor for the accuracy of the study and tor the amount of resolved details, especially in regions where the knowledge of the Earth interior is poor. In such cases, we can try to improve the velocity model. There are some methods how an existing 1-D model can be enhanced, e.g. by inversion of dispersion curves to a velocity model [Novotný et al., 2001; Novotný et al., 2015].

In the following chapter, which was published as Vackář et al. [2014], we show an example, how we dealt with observation of fast long-period seismic waves, which could not be simulated in any of published velocity models for a specific region, and how we improved the velocity model to make possible simulating leaking modes.

2. Strong fast long-period waves in the Efpalio 2010 earthquake records: explanation in terms of leaking modes

Paper by Vackář, J., J. Zahradník, and E. Sokos, published in 2014 in Journal of Seismology 18, pp. 81–91.

Abstract The January 18, 2010, shallow earthquake in the Corinth Gulf, Greece (M_w 5.3) generated unusually strong long-period waves (periods 4–8 seconds) between the *P*- and *S*-wave arrival. These periods, being significantly longer than the source duration, indicated a structural effect. The waves were observed in epicentral distances 40–250 km and were significant on radial and vertical component. None of existing velocity models of the studied region provided explanation of the waves. By inverting complete waveforms we obtained an 1-D crustal model explaining the observation. The most significant feature of the best-fitting model (as well as the whole suite of models almost equally well fitting the waveforms) is a strong velocity step at depth about 4 km. In the obtained velocity model, the fast long-period wave was modeled by modal summation and identified as a superposition of several leaking modes. In this sense, the wave is qualitatively similar to *PL* or *Pnl* waves, which however are usually reported in larger epicentral distances. The main innovation of this paper is emphasis to smaller epicentral distances. We studied properties of the wave using synthetic seismograms. The wave has a normal dispersion. Azimuthal and distance dependence of the wave partially explains its presence at 46 stations of 70 examined. Depth dependence shows that the studied earthquake was very efficient in the excitation of these waves just due to its shallow centroid depth (4.5 km).

2.1 Introduction

Observations of long-period seismic waves appearing in seismograms between *P*- and *S*-wave onsets have been reported since the early 1930's by Somwille, who also introduced the name *PL* (*P*-long). This information can be found in Oliver and Major [1960] who provided an explanation in terms of leaking modes and dispersion curves. Su and Dorman [1965] related *PL* waves to a crust-mantle wave-guide. The waves were observed on various oceanic and continental paths, in epicentral distances 400–5500 km and periods ranging between 5 and 35 s and were reported as a general phenomena.

The *PL* wave was investigated theoretically since the 60's. Phinney [1961] studied analytically 3 cases: (i) the propagation of leaking modes in a halfspace, (ii) solid halfspace in contact with liquid halfspace and (iii) two halfspaces in welded contact. He showed that leaking modes correspond to complex roots of dispersion equation. Gilbert [1964] analyzed the propagation of *PL* waves in stratified elastic halfspace. Dainty [1971] calculated phase and group velocity dis-

persion curves and attenuation curves for different leaking modes in multilayered elastic halfspace.

Helmberger and Engen [1980] introduced the name *Pnl* wave for wave groups consisting of P_n and *PL* wave. Patton and Doser [1988] showed that the *Pnl* wave is usable for point source inversion from regional records. Saikia and Burdick [1991] studied the nature of the fine structure of *Pnl* waves and found that it is sensitive to the velocity gradient near the free surface.

PL and *Pnl* waves are used in seismology mostly for structural studies. Shaw and Orcutt [1984] determined the crustal thickness of the Tibetan Plateau using synthetic seismograms of *PL* waves obtained by wave number integration. Holt and Wallace [1990] examined crustal thicknesses and upper mantle velocities in the same region by *Pnl* waveform inversion. Fujita and Nishimura [1993] estimated the crustal velocity structure of Japan using waveform modeling of *PL* wave after proving its resolution in many numerical test. Savage and Helmberger [2004] used *Pnl* waves to calibrate the site response and the amplification factor. Tan et al. [2010] used *Pnl* waves for path calibration and point source inversion.

Another well-known fast long-period wave is the *W* phase [Kanamori, 1993]. This wave is usually explained as a superposition of the fundamental, first, second and third overtones of spheroidal modes or Rayleigh waves. Its periods lie in the range of 100–1000 s in distances of thousands of kilometers and group velocities are 4.5–9 km/s. Thanks to them, it is very useful for rapid determination of the source parameters and for tsunami warning [Kanamori and Rivera, 2008]. Contrary to the *PL* wave, this phase does not require any leaking-modes explanation. The high velocity is controlled by penetration depth.

Numerical modeling of *PL* waves and of similar phases is possible by means of tools for the calculation of complete wavefield, e.g. by the Discrete Wavenumber method where leaking modes are included, as shown by Bouchon and Ali [1977] and Bouchon [1981]. Helmberger and Engen [1980] simulated the *PL* waves by the ray summation in a layer over a halfspace. Haddon [1984] showed that leaking modes can be obtained by modal summation in the same way as Rayleigh wave, considering complex solution of the dispersion equation.

Nevertheless, a detailed numerical analysis of observed *PL* waves and their properties has been quite rare so far. For example, we are not aware of any study devoted to these waves at near-regional distances.

On January 18, 2010, a M_w 5.3 earthquake occurred in the Gulf of Corinth, Greece . Seismic records of this earthquake attracted our attention because of strong long-period (4–8 s) waves between *P*- and *S*-wave arrival in epicentral distances 40–250 km. Therefore, the main goal of this paper is to discuss nature of these specific phases in terms of the *PL* waves and describe their properties.

This paper starts with the description of the observation and data used. Since we were unable to successfully simulate this wave in existing crustal models of the studied region, we apply the complete waveform inversion to obtain a velocity model supporting the *PL* wave. Then we resolve contributing modes by modal summation and, based on synthetic seismograms, we describe properties of the *PL* wave.

2.2 Observation of Fast Long-Period Waves

The Efpalio 2010 earthquake sequence occurred in the western part of the Gulf of Corinth, Greece [Sokos et al., 2012]. The strongest event of the sequence was an earthquake with magnitude 5.3, exhibiting normal faulting along E–W trending planes (Table 2.1).

Table 2.1: Parameters of the Efpalio earthquake according to Sokos et al. [2012].

origin time	January 18, 2010 15:56:09.8 UTC
hypocenter	38.419° N, 21.915° E, depth 6.6 km
centroid	38.422° N, 21.941° E, depth 4.5 km
seismic moment	$0.97 \cdot 10^{17}$ Nm
moment magnitude M_w	5.3
nodal planes	102° / 55° / −83°
(strike / dip / rake)	270° / 36° / −100°

We inspected 70 broadband seismic stations in epicentral distances 12–600 km. The records were instrumentally corrected and rotated to the radial-tranverse-vertical (RTZ) system. A noticeable fast long-period wave was observed at more than half of the stations (Fig. 2.1). The wave is significant in a considerable number of the stations in epicentral distances 40–250 km, having its amplitude of the same order as the seismogram maximum in the surface-wave group. At some other stations the wave is present, but much weaker. There are a few stations where the wave is visually not apparent. As observed in Fig. 2.1, the wave occurrence has no simple dependence on azimuth and epicentral distance although the north-south direction seems to predominate. The wave has period 4–8 seconds and it is seen on radial and vertical component between the *P*- and *S*-wave arrival (Fig. 2.2). The latter suggests its relation to Rayleigh waves, while the large group velocity suggests its relation to some higher modes. Hereafter, we will refer to the wave as *PL* wave, because of qualitative similarity to *PL* or *Pnl* waves described at regional distances and longer periods.

2.3 Inversion of Crustal Structure

We started with attempts to simulate the observed *PL* wave by the forward modeling in the existing regional crustal models [Latorre et al., 2004; Novotný et al., 2001, 2008, 2012; Rigo et al., 1996]. All existing models generated a very weak *PL* wave, if any. There are also some tomografic model of the studied region (e.g. Karagianni et al. [2005] and Latorre et al. [2004]), but their resolution in the shallow depths is limited. To find another model, better explaining the *PL* wave, we inverted full waveforms into a 1-D crustal model. The crucial advantage of the full waveform inversion is its ability to use information contained in many wavegroups of the record without need to identify the individual wavegroups with a specific mode. We used a subset of 9 stations with strong *PL* wave, namely stations MAM, DRO, EVR, RLS, GUR, AMT, LTK, VLX and PYL in epicentral distances 36–170 km.

The Discrete Wavenumber method [Bouchon, 1981; Coutant, 1989] is used for forward problem solution. The Neighborhood Algorithm [Sambridge, 1999]

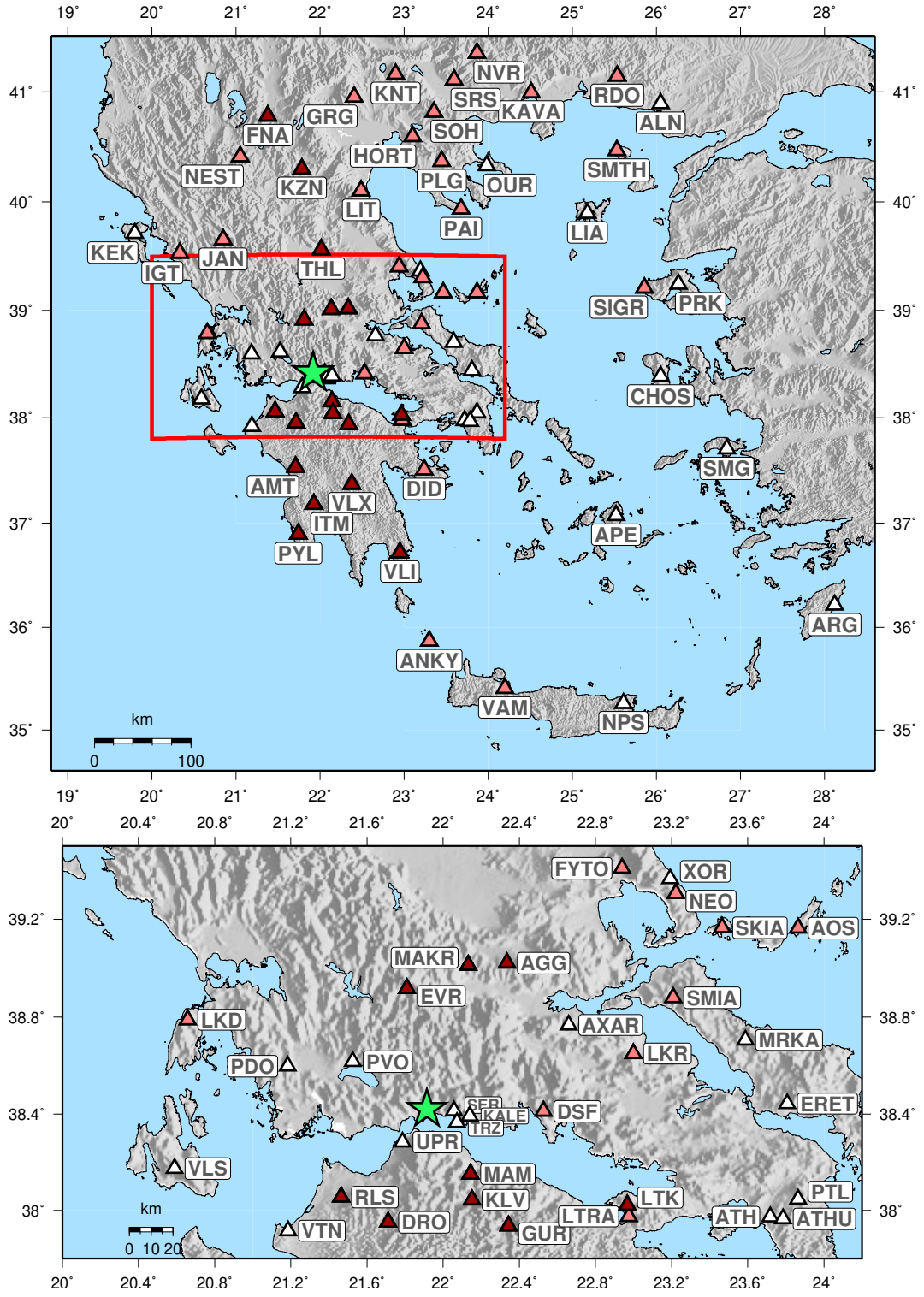

Figure 2.1: Seismic stations are marked according to the strength of the observed fast long-period wave: strong – dark red, weak – light red, absent – white. The classification is based on the ratio between the amplitudes of the *PL* wave and the strongest wave group (surface waves) in the displacement record; the strong, weak, and absent *PL* waves refer to the ratio of about 50–100 %, 20–50 % and less than 20 %, respectively. Epicenter of the Efpalio earthquake is labeled by a green asterisk.

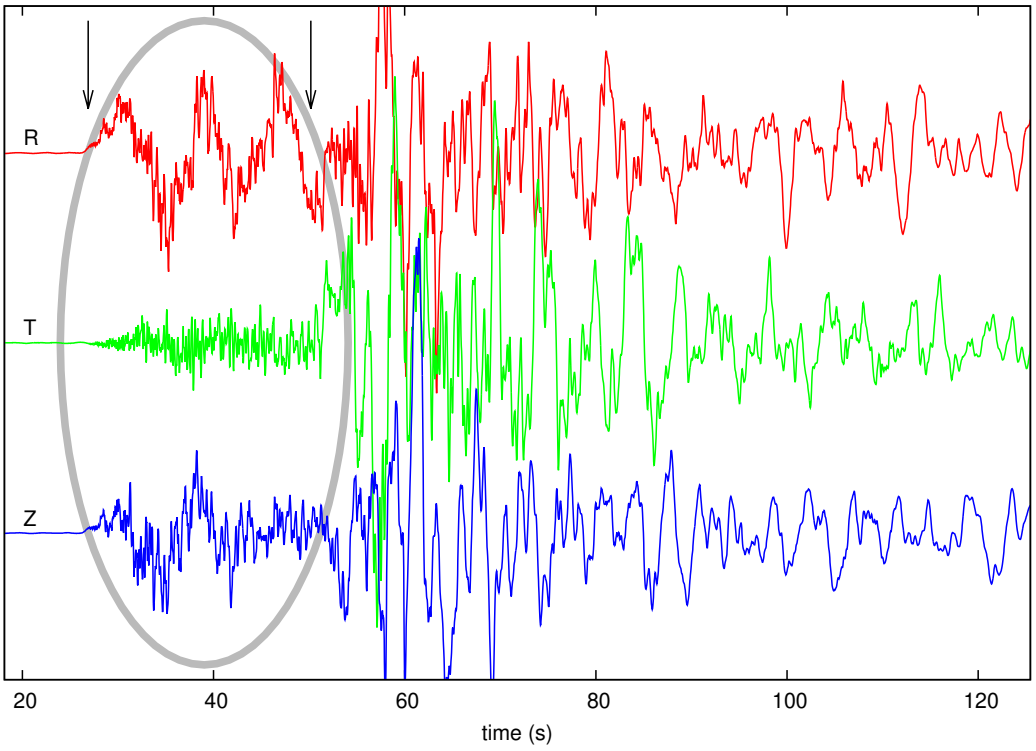

Figure 2.2: Instrumentally corrected, rotated velocity record of the Efpalio 2010 earthquake on broad-band station PYL (Pylos, epicentral distance 170 km). Highlighted by an ellipse is a strong fast long-period wave on the radial and vertical component with prevailing period of about 8 seconds, starting simultaneously with the P-wave arrival. Arrows mark the approximate arrival times of P wave and S wave.

Table 2.2: Parametrization of the inverse problem used. There are 11 parameters to be inverted.

parameter		range	constraint
thickness	layer 1	0.2–2.8 km	total thickness 10 km
	layer 2	0.2–3.0 km	
	layer 3	0.2–4.0 km	
	layer 4	arbitrary	
v_P	layer 1	2–5 km/s	no low-velocity channel for v_P
	layer 2–4	2–7.2 km/s	
v_P/v_S	layer 1–4	1.41–3.0	no low-velocity channel for v_S

is used for stochastic search, providing an ensemble of models that preferentially sample the good data-fitting regions of parameter space, rather than finding just a single best-fitting model.

Observed and synthetic seismograms were filtered by acausal four-parameter bandpass filter 0.02-0.05-0.10-0.20 Hz, which is flat between 0.05 and 0.10 Hz, and there are cosine tapers at the edges. The misfit m is defined as

$$m = \frac{\sum\limits_{stat}\sum\limits_{comp}\int W(t,stat)\left(o(t)-s(t)\right)^2 dt}{\sum\limits_{stat}\sum\limits_{comp}\int W(t,stat)o(t)^2 dt}\ , \tag{2.1}$$

where t is time, $o(t)$ and $s(t)$ is the observed and synthetic seismogram, respectively, and *comp* stands for summing over seismogram components and *stat* over stations. $W(t, stat)$ is weighting function used to emphasize typical interval of PL wave (in particular, $W = 2$ between ray-theoretical P- and S-wave arrival and $W = 1$ elsewhere). Point source synthetics were calculated for the centroid location and the focal mechanism of Table 2.1. The moment-rate time function is 1-second triangle. Its duration corresponds to magnitude of the event. However, compared to the characteristic period of the wave of interest and the filtration mentioned above, the shape of the time function is unimportant for the inversion. A small source timeshift (up to 2 s) is allowed around location-provided origin time. We inverted thicknesses of layers and P- and S-wave velocities in the uppermost 10 km of crust. Considering prevailing period of the PL wave ($\sim$ 5 s) we suppose that the deeper structure is less important. Densities have been evaluated by an empirical formula and quality factors Q_P and Q_S were fixed to values 300 and 150, respectively. Deeper layers were fixed according to an ongoing parallel study. The used parametrization is shown in Table 2.2.

Characteristic feature of the result (Fig. 2.3) is that the best models appear to be composed of 3 layers. Remarkable velocity step of both v_P and v_S velocities is at depth of 4 km, the topmost 2 km have higher v_P/v_S ratio than the rest of model. The best fitting model well reproduces the PL wave (Fig. 2.4) in contrast to the existing crustal models. These results proved to be stable in many additional tests as altering parametrization, changing the set of inverted stations, etc. Naturally, the obtained model of the uppermost 10 km may be influenced by uncertainty of the deeper layers which we represented by a fixed model. Although non-unique and possibly deviating from the real structure, the obtained model is a useful tool for *interpretation* of the PL wave nature and properties in the following sections.

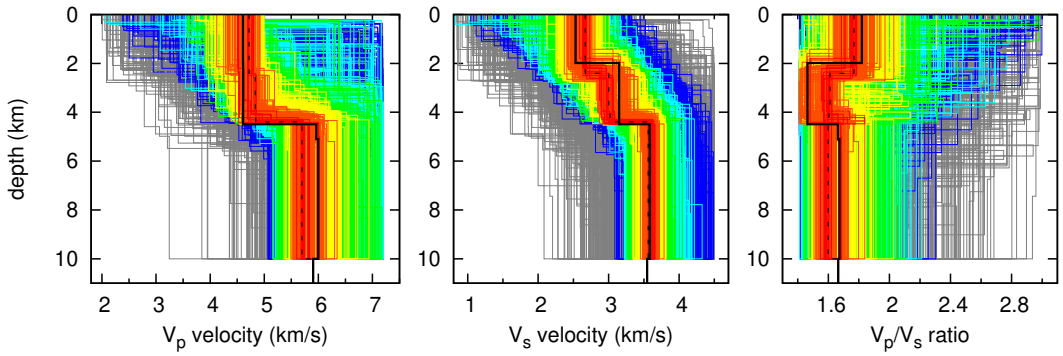

Figure 2.3: Simultaneous inversion of 9 stations. All models for which the forward problem was solved are shown. Their misfit function is presented by the rainbow spectrum from red (misfit less than 1.005 of the best value) to blue (misfit 1.16–1.32 of the best one) with exponentially increasing width of color sets. Models with misfit worse than 1.32 of the best one are in gray. Two models of the best group are displayed by black lines (the best one by the solid, an alternative one by the dashed line), these models are considered in further study.

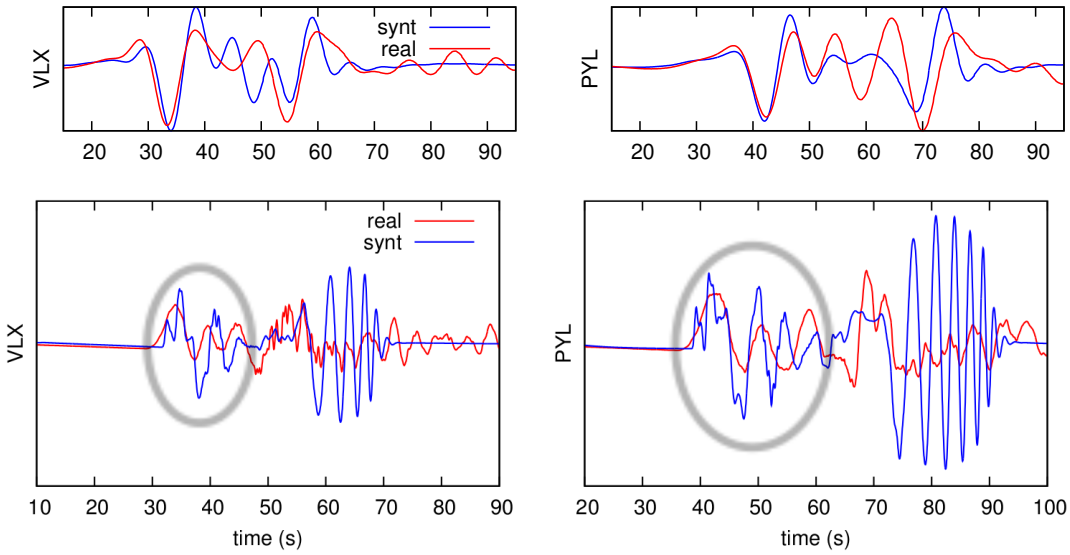

Figure 2.4: Comparison of the real records (red) and synthetic seismograms (blue) calculated in the best model (Fig. 2.3). Example of radial component at stations VLX (left) and PYL (right) are shown. Additional stations are shown in a supplement of this chaper. Upper panels show velocity records filtered up to 0.3 Hz, as used in the inversion. In the lower panels there are displacement records up to 10 Hz shown to make the *PL* wave seen in context of other waves (these high-frequency records were not used in the inversion). Intention was to simulate the *PL* wave between the *P*- and *S*-wave arrival (encircled).

2.4 Theoretical Interpretation of *PL* Wave

We used the best-fitting model obtained in the previous section to find a theoretical interpretation of the *PL* wave. To this goal, synthetic seismograms were forward simulated by three methods: (i) The Discrete Wavenumber (DWN) method gives complete wave field, but it does not explain the nature of the individual wavegroups. (ii) Standard modal summation (code from Computer Programs in Seismology by Herrmann [2004]) gives normal (fundamental and higher) modes of surface waves existing in a given velocity model, corresponding to real roots of dispersion equation. (iii) Extended modal summation make it possible to calculate almost complete synthetic seismograms (including leaking modes) by the "locked mode approximation" [ibid.]. Technically, the extended modal summation is performed by adding an artificial high velocity cap zone at great depth to the given velocity model (in this paper we use v_P 11 km/s below depth of 330 km). After this modification, the leaking modes corresponding to complex roots of the dispersion equation in the original model formally become the normal modes corresponding to real roots.

Comparison of the three methods (Fig. 2.5) enables the interpretation. Standard modal summation (for 100 modes) strongly differs from DWN, it agrees only at wavegroups of surface waves in the later part of seismogram. Extended modal summation agrees with DWN in broader temporal range, except *P* body wavegroup, but including fast long-period wave between 30–50 s.

To identify which modes contribute the *PL* wave, we calculated seismograms by summing the first n modes; the calculation was repeated for n varying from 0 to 35. It was found that *PL* wave is absent when we sum less than 8 modes. We need to sum at least 20 modes to create the *PL* wave. Subsequent build-up of the wave is illustrated in Fig. 2.6, even better demonstrated by an animation in electronic supplement of Vackář et al. [2014], available at `http://geo.mff.cuni.cz/~vackar/papers/Vackar_etal_JOSE_2014_supp2.avi`. To illustrate the role of the individual n-th mode, we subtract sum of $n-1$ modes from the sum of n modes. We found that the contribution of every mode is weak (see again Fig. 2.6), obviously the *PL* wave is a superposition of several modes. Because none of these modes is present in the standard modal summation (i.e. without the high velocity cap) we can clearly identify them (and thus also the *PL* wave) as leaking modes.

As a validation, we repeated the same comparison in another crustal model (black dashed line in Fig. 2.3) and in different epicentral distances; the results remained nearly the same. When we strongly increased the number of modes summed (up to 500), the result did not change. Another test addressed the effect of the artificial, high velocity cap zone used in extended modal summation. When we decreased v_P from 11 to 10 km/s in the added halfspace and shifted its boundary from 330 to 130 km, the numbers of modes mostly contributing the *PL* waves changed rapidly (in this case, the main contributing modes were 4–9), although the sum remained almost the same. It means that the extended summation can be understood as an approximation in which the individual modes have only formal meaning, and only the sum of modes has the physical meaning.

Partial conclusion of this section is as follows: the *PL* wave can be modeled by DWN and extended modal summation. Extended modal summation, in contrast

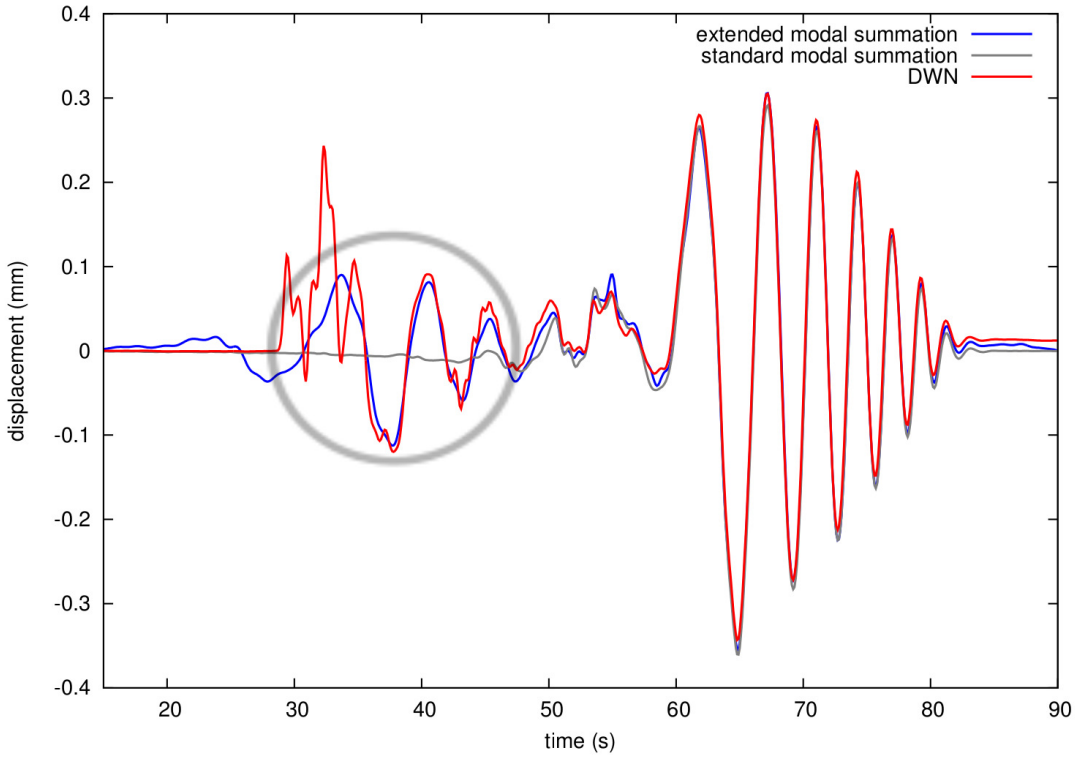

Figure 2.5: Radial component of a synthetic seismograms calculated in three different ways. Standard modal summation (gray) corresponds to DWN (red) only at slower wavegroups and does not explain the *PL* wave (encircled). Extended modal summation (blue) corresponds to DWN except *P* body wavegroup; the *PL* wave is explained very well. The velocity model obtained by complete waveform inversion was used. The seismogram is from a station in epicentral distance 170 km. The source depth is 6.6 km.

to DWN, enables clear interpretation of the *PL* wave as a superposition of leaking modes. Specific number of modes needed depends on technical realization of the locked mode approximation.

2.5 *PL* Wave Properties

We used the best-fitting model found in Section 2.3 to describe some properties of the *PL* wave using synthetic seismograms. We tested dependence of the amplitude of the wave on receiver azimuth, receiver distance and source depth (Fig. 2.7). We evaluated ratio of the amplitudes of *PL* wave and Rayleigh wave in synthetic displacement records calculated by modal summation. We found that the wave is strongest in direction perpendicular to strike and nearly independent on receiver distance in range 60–200 km. These dependencies give a possible partial explanation of the observed *PL*-wave amplitudes, namely the predominance of the *PL* wave in the north-south direction, i.e. perpendicularly with respect to the fault strike (Fig. 2.1).

The ratio of amplitudes of the *PL* wave and Rayleigh wave is strongly dependent on the source depth, reaching its maximum at the hypocentral depth about 5 km, similar to the hypocentral depth of the studied earthquake. The

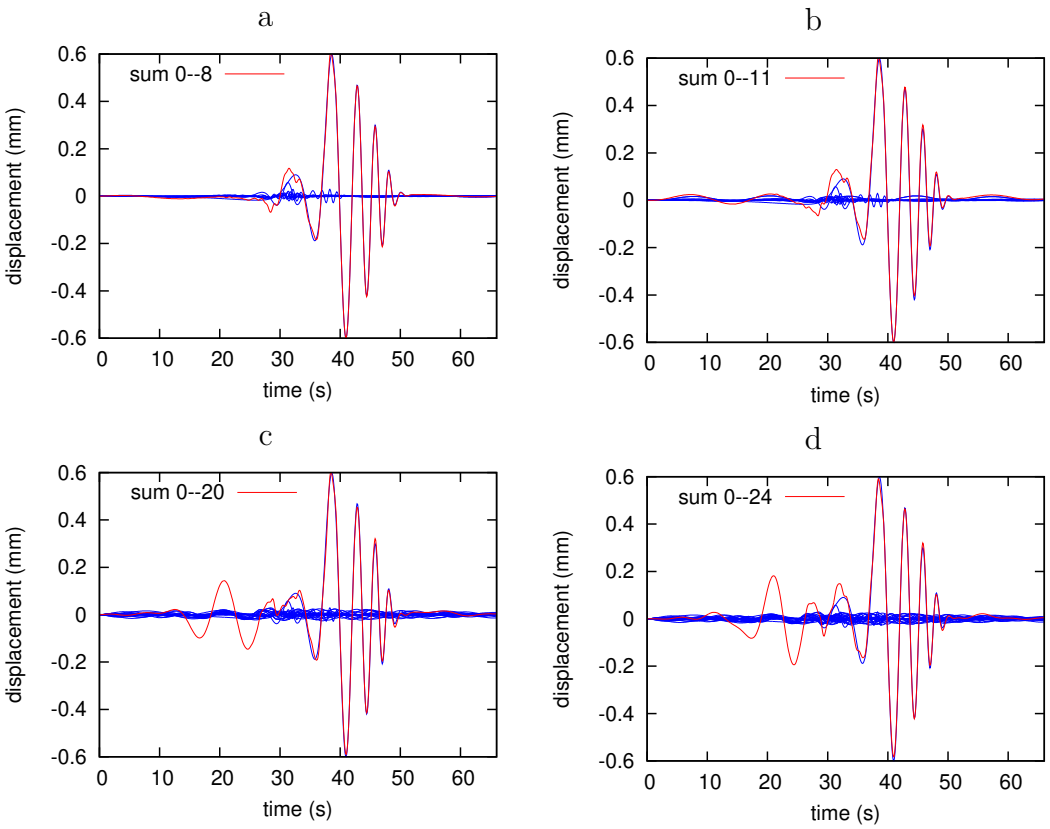

Figure 2.6: Mechanism of creating the *PL* wave using extended modal summation. Every panel shows a sum of the first n modes (red) and individual contributions of modes (see the tightly clustered family of blue curves), plotted in the same scale as the sum. The results for $n = 8$, 11, 20 and 24 are shown in panels a, b, c and d, respectively. The *PL* wave is present only in the last two cases. The mostly contributing modes are between 11th and 20th in this particular example.

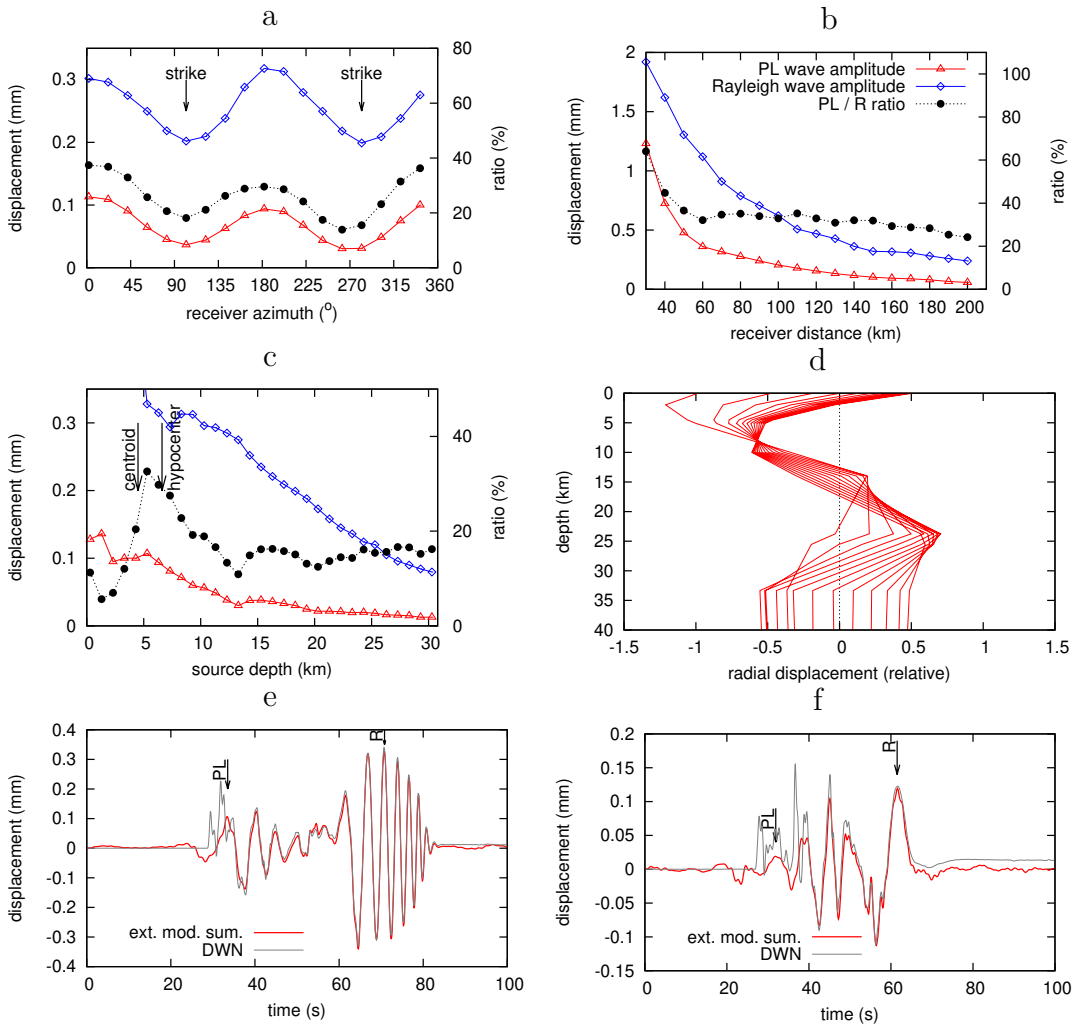

Figure 2.7: The amplitude of the *PL* wave is dependent on the epicentral distance, station azimuth and source depth. We compared amplitude of *PL* wave (the first positive maximum in the seismogram) with the largest maximum of Rayleigh wave (panels e and f, measured values shown by arrows). The best model from inversion (Fig. 2.3) and parameters of the Efpalio earthquake (Table 2.1) are used. We measured amplitudes in synthetic seismograms provided by extended modal summation. The ratio of the *PL* wave versus Rayleigh wave is 30–35 % in direction perpendicular to strike while ∼20 % in strike direction (panel a). The ratio is slightly decreasing (from 35 % to 25 % considering azimuth 192°) in distances 60–200 km; it is much higher in distances shorter than 60 km (panel b). The ratio depends on the source depth with maximum at the source depth ∼5 km (panel c). The eigenfunctions (for period 5 s) of modes contributing the *PL* wave have maxima at similar depth (panel d). The change of seismogram shape in the epicentral distance of 169 km is illustrated for depth of 5.4 and 25.4 km in panels e and f, respectively; note the different vertical scale.

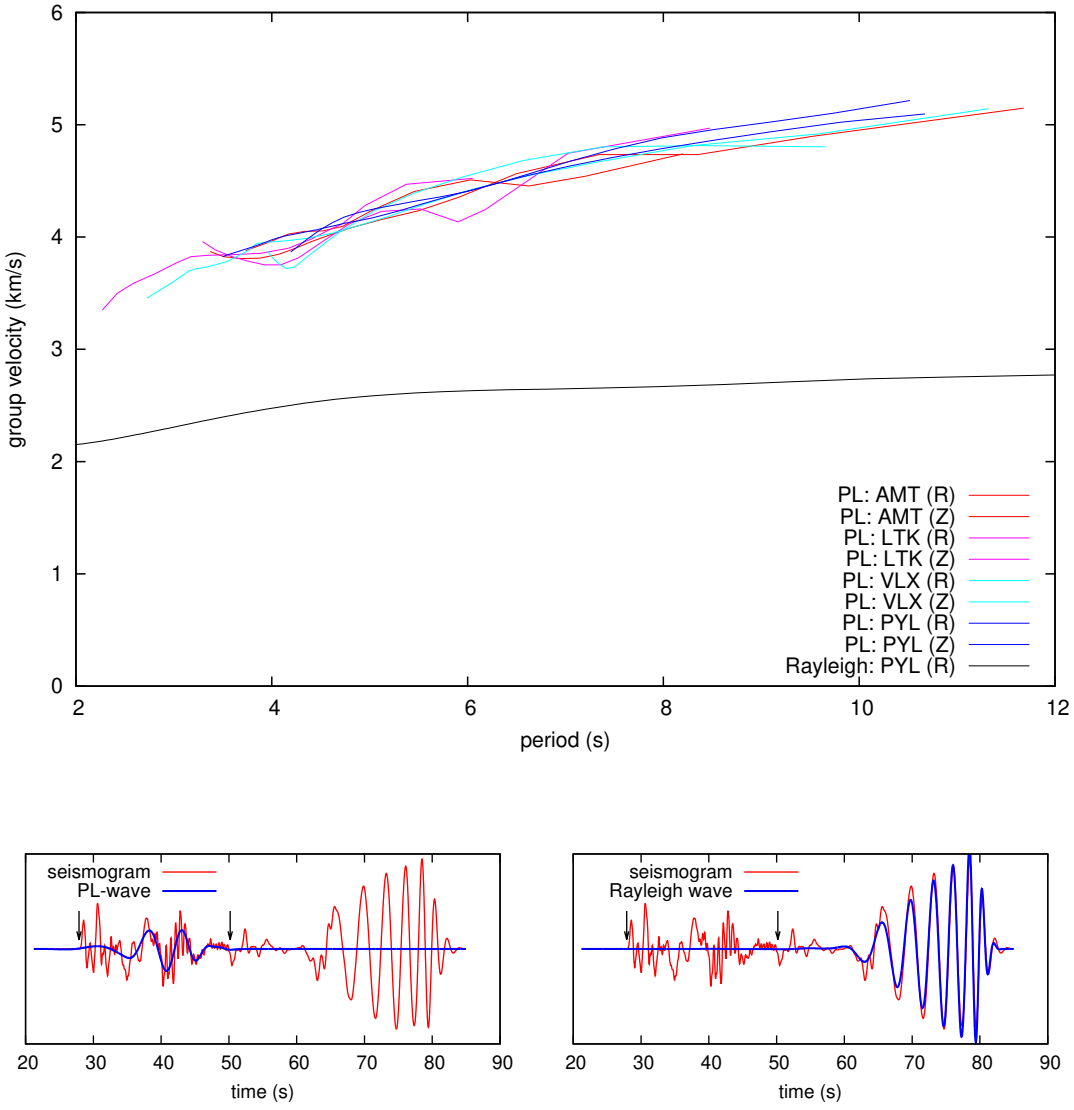

Figure 2.8: **Top:** Dispersion curves of the *PL* waves for synthetic records at different stations. The best model from inversion (Fig. 2.3) and parameters of the Efpalio earthquake (Table 2.1) are used. For comparison, the dispersion curve of the fundamental mode of the Rayleigh model at station PYL is also shown. **Bottom:** Radial component of synthetic seismogram (red) for the Efpalio earthquake at station PYL (Pylos, epicentral distance 170 km) and the wave group corresponding to dispersion curve (blue): *PL* wave (left) and Rayleigh wave (right). Black arrows mark the approximate arrival times of *P* wave and *S* wave.

dependence on source depth is related to eigenfunctions of modes contributing the wave (Fig. 2.7, panels c and d).

The frequency-time analysis of synthetic records in the best-fitting model was performed (program SVAL by Kolínský [2004], version 2011). It has shown that the *PL* wave has normal dispersion. An example is shown in Fig. 2.8 where we compare dispersion curves for radial and transverse components at four stations. Small differences between the curves in Fig. 2.8 are related to problems to identify a correct branch of the dispersion curve when the *PL* wave is overlapping in the analyzed seismogram with other waves. The synthetic dispersion curves are not compared with real ones in this paper. It is because the real dispersion curves are path dependent due to laterally varying 3D crustal structure. This variation (and derivation of a suite of 1D models along the individual path groups) will be investigated in a separate paper. In this paper, focused on the nature of the *PL* wave, the 1D model is sufficient.

2.6 Conclusion

We investigated fast long-period waves (*PL* waves) observed in most of 70 records of Efpalio 2010 earthquake in the epicentral distances of 40–250 km. The study is innovative in four aspects: (i) Physical properties of similar waves have been mostly discussed in larger epicentral distances ($>$ 400 km) in the previous papers. We extend the study to smaller distances. (ii) Successful simulation of such waves in not straightforward. None of the previous velocity models explained the observation. We found a suite of successful models by full waveform inversion performed by the Discrete Wavenumber method and by the Neighborhood Algorithm. (iii) In contrast to most of published papers dealing with analytical solution in a simple model, we performed a numerical modeling in multilayered media. (iv) Three different methods of the seismogram simulation were comprehensively combined.

By modal summation we showed that the *PL* wave is created by a superposition of several leaking modes of Rayleigh waves. The *PL* wave has normal dispersion. Azimuthal and distance dependence of the *PL* wave provides a possible partial explanation of spatial pattern of the *PL*-wave existence and strength. The Efpalio earthquake was particularly efficient in the *PL*-wave excitation due to its shallow centroid depth of 4.5 km.

Acknowledgement

The authors acknowledge the data exchange between the Patras University (including 10 joint Patras-Prague stations) and the Hellenic Unified Seismic Network (HUSN). We thank to P. Bernard, J. Burjánek, V. Plicka, F. Gallovič for many useful suggestions. The work was supported by the Czech Republic grants SVV-2013-267308, GAČR 210/11/0854 and GAUK 496213.

2.7 Supplement

Comparison of the real records (red) and synthetic seismograms (blue) calculated in the best-fitting model. Vertical components at all inverted stations are displayed. Upper pannel at each station shows velocity records low-pass filtered up to 0.3 Hz, as used in the waveform inversion. In the lower panels there are displacement records displayed up to 10 Hz to make the PL-wave better visible in context of other waves. The moment-rate function is a 1-s triangle.

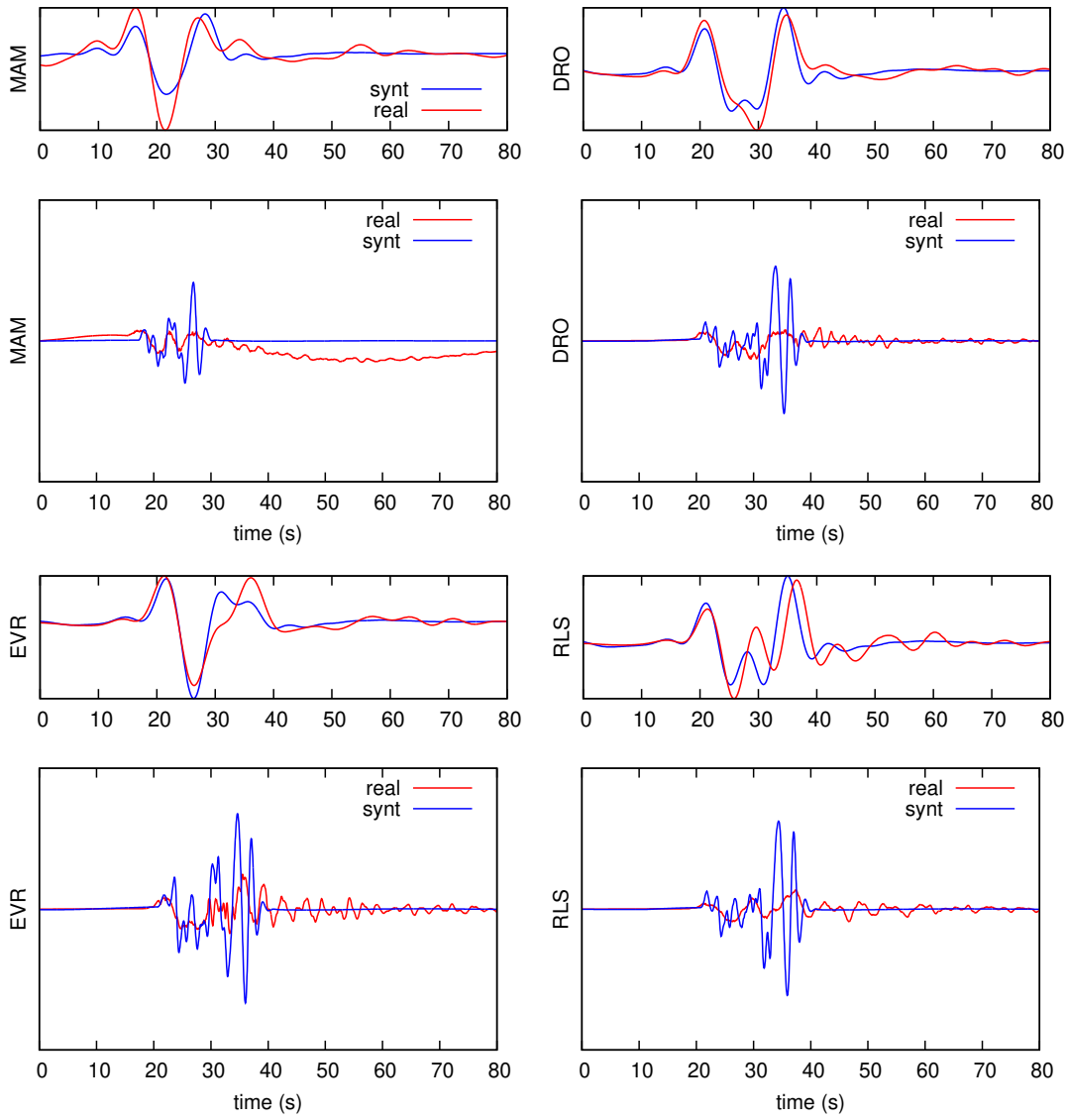

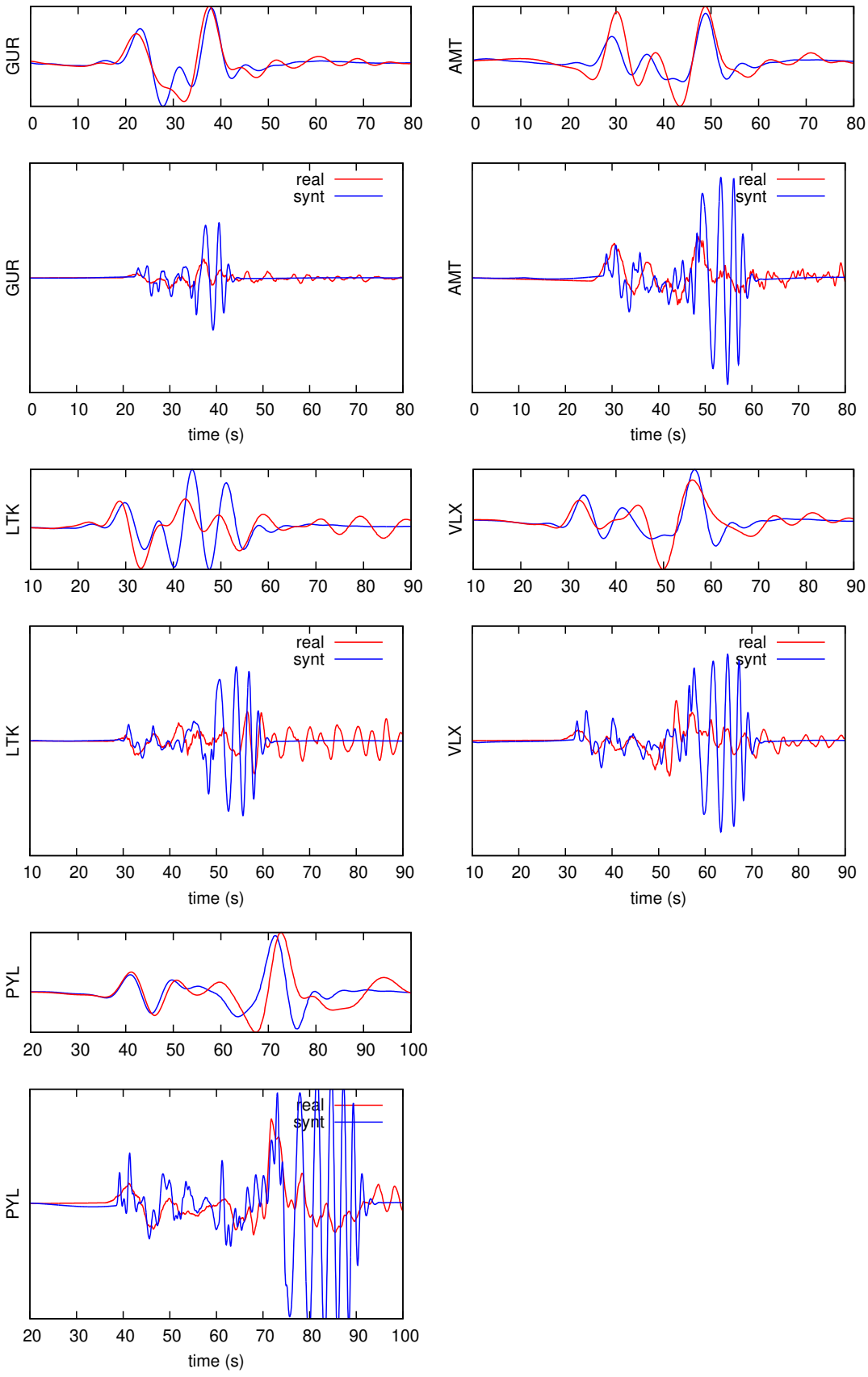
GUR
AMT
real
synt
time (s)
LTK
VLX
PYL

3. Bayesian formulation of the inverse problem of centroid moment tensor

3.1 Mathematical formulation of the problem

This section is based on Section 2 of Vackář et al. [2017]. Full derivation of the involved equations is added here.

A Bayesian approach is a probabilistic method projecting data errors and prior information into the uncertainty of model parameters. In addition to the best-fitting CMT solution, the method provides a posterior probability density function (PPDF) of the parameters. The PPDF can be obtained analytically for linear inverse problems in a L^2-norm and Gaussian distributions of data uncertainties. For non-linear problems a systematic grid search can be used, but (except for problems with very few parameters) it is computationally highly inefficient. That is why stochastic sampling algorithms have been developed to provide an approximation of the PPDF [Sambridge, 2014; Sambridge and Mosegaard, 2002].

Here we propose a hybrid approach, where the centroid position and time are evaluated on a grid of points, and the MT is solved by least squares. In each grid point the PPDF of the MT solution (which is Gaussian because the problem is linear) is obtained analytically. Then such PPDFs are combined to obtain a full (non-Gaussian) PPDF. So we obtain the same PPDF as would be obtained by a stochastic method, but using just a 4-dimensional grid search instead of sampling a 10-dimensional model space. The grid is chosen in such a way that it covers all relevant locations and its sampling density controls PPDF discretization, for details see Section 7.7. By choosing the grid, we define a prior information for centroid location and time, which is uniform within the grid and zero elsewhere. In other words, we assume that the hypocenter definitely lies within the grid, but no position within the grid is preferred.

In the linear MT problem in a given space-time grid point i (x_i, y_i, z_i, t_i) the observables $\boldsymbol{d}$ and model parameters $\boldsymbol{m}$ are related by $\boldsymbol{d} = \mathbf{G}\boldsymbol{m}$, where matrix $\mathbf{G}$ (forward problem matrix) is composed of Green's functions (more exactly, the forward problem matrix $\mathbf{G}$ in our method is composed of elementary seismograms of 6 elementary moment tensors, which are calculated from Green's functions). Let the measured data, which include measurement uncertainties, be denoted $\boldsymbol{d}_{obs}$, and assume that their uncertainties are Gaussian with the data covariance matrix denoted as $\mathbf{C}_D$ (the content of the data covariance matrix is described in the next Chapter 6). With no prior information about the MT parameters (i.e., formally, Gaussian prior with infinite variance), the least-squares solution for the model parameters is [Tarantola, 2005, eq. 3.40–3.41]

$$\widetilde{\boldsymbol{m}}_i = \left(\mathbf{G}_i^T \mathbf{C}_D^{-1} \mathbf{G}_i\right)^{-1} \mathbf{G}_i^T \mathbf{C}_D^{-1} \boldsymbol{d}_{obs} \,, \tag{3.1}$$

where $\widetilde{\boldsymbol{m}}_i$ denotes the inverted model parameters in grid point i, which gener-

ally differ from the true model parameters $\boldsymbol{m}$. The uncertainties of the model parameters are described by the model parameters covariance matrix $\widetilde{\mathbf{C}}_i^M$, given by

$$\widetilde{\mathbf{C}}_i^M = \left(\mathbf{G}_i^T \mathbf{C}_D^{-1} \mathbf{G}_i\right)^{-1} \ . \tag{3.2}$$

The misfit value is then

$$\text{misfit}_i = \left(\boldsymbol{d}_{obs} - \mathbf{G}_i \widetilde{\boldsymbol{m}}_i\right)^T \mathbf{C}_D^{-1} \left(\boldsymbol{d}_{obs} - \mathbf{G}_i \widetilde{\boldsymbol{m}}_i\right) \ . \tag{3.3}$$

The PPDF for MT components in a fixed space-time point i is given by 6-dimensional Gaussian function which is centered in the best solution for the given grid point i,

$$\text{PPDF}_i(\boldsymbol{m}) = \frac{1}{c} \exp\left(-\frac{1}{2} \left(\boldsymbol{d}_{obs} - \mathbf{G}_i \boldsymbol{m}\right)^T \mathbf{C}_D^{-1} \left(\boldsymbol{d}_{obs} - \mathbf{G}_i \boldsymbol{m}\right)\right) \ , \tag{3.4}$$

where c is a constant normalizing the total (10-dimensional) PPDF to unity (see lower). After an algebra, which is in detail shown below in Section 3.2, the PPDF can be equivalently written

$$\begin{aligned}
&\text{PPDF}_i(\boldsymbol{m}) = \\
&= \frac{1}{c} \exp\left(-\frac{1}{2} \left[\left(\boldsymbol{d}_{obs} - \mathbf{G}_i \boldsymbol{m}\right)^T \mathbf{C}_D^{-1} \left(\boldsymbol{d}_{obs} - \mathbf{G}_i \boldsymbol{m}\right)\right]\right) = \\
&= \frac{1}{c} \exp\left(-\frac{1}{2} \left[\left(\boldsymbol{m} - \widetilde{\boldsymbol{m}}_i\right)^T \widetilde{\mathbf{C}}_M^{-1} \left(\boldsymbol{m} - \widetilde{\boldsymbol{m}}_i\right) + \left(\boldsymbol{d}_{obs} - \mathbf{G}_i \widetilde{\boldsymbol{m}}_i\right)^T \mathbf{C}_D^{-1} \left(\boldsymbol{d}_{obs} - \mathbf{G}_i \widetilde{\boldsymbol{m}}_i\right)\right]\right) = \\
&= \frac{1}{c} \exp\left(-\frac{1}{2} \left[\left(\boldsymbol{m} - \widetilde{\boldsymbol{m}}_i\right)^T \widetilde{\mathbf{C}}_M^{-1} \left(\boldsymbol{m} - \widetilde{\boldsymbol{m}}_i\right) + \text{misfit}_i\right]\right) = \\
&= \frac{1}{c} \exp\left(-\frac{1}{2} \left(\boldsymbol{m} - \widetilde{\boldsymbol{m}}_i\right)^T \widetilde{\mathbf{C}}_M^{-1} \left(\boldsymbol{m} - \widetilde{\boldsymbol{m}}_i\right)\right) \exp\left(-\frac{1}{2} \text{misfit}_i\right) \ .
\end{aligned} \tag{3.5}$$

The purpose of this transformation is to rewrite PPDF of unknown shape by the misfit and 6-D Gaussian function, which can be integrated later.

The normalizing constant c is obtained by integration over all model parameters and summation over space-time grid points

$$\begin{aligned}
1 &= \sum_i \int \text{PPDF}_i(\boldsymbol{m}) \, \mathrm{d}\boldsymbol{m} \, \Delta V_i = \\
&= \sum_i \int \frac{1}{c} \exp\left(-\frac{1}{2} \left(\boldsymbol{m} - \widetilde{\boldsymbol{m}}_i\right)^T \widetilde{\mathbf{C}}_M^{-1} \left(\boldsymbol{m} - \widetilde{\boldsymbol{m}}_i\right)\right) \exp\left(-\frac{1}{2} \text{misfit}_i\right) \mathrm{d}\boldsymbol{m} \, \Delta V_i = \\
&= \sum_i \frac{1}{c} \int \exp\left(-\frac{1}{2} \left(\boldsymbol{m} - \widetilde{\boldsymbol{m}}_i\right)^T \widetilde{\mathbf{C}}_M^{-1} \left(\boldsymbol{m} - \widetilde{\boldsymbol{m}}_i\right)\right) \mathrm{d}\boldsymbol{m} \, \exp\left(-\frac{1}{2} \text{misfit}_i\right) \Delta V_i = \\
&= \sum_i \frac{1}{c} \sqrt{(2\pi)^6 \det \mathbf{C}_i^M} \exp\left(-\frac{1}{2} \text{misfit}_i\right) \Delta V_i = \\
&= \sum_i a_i \ ,
\end{aligned} \tag{3.6}$$

where we used n-dimensional Gaussian integral [Wikipedia contributors, 2018] and the ΔV_i is a volume belonging to the grid-point i. In our case (uniform sampling in both space and time), it is

$$\Delta V_i = \Delta x \, \Delta y \, \Delta z \, \Delta t \ , \tag{3.7}$$

where Δx, Δy, and Δz is grid spacing in direction of the coordinates x, y, and z, respectively, and Δt is time-grid spacing.

We denoted a_i the PPDF integrated over all MT parameters at a given space-time grid point i. It is composed of the analytically estimated uncertainties of all MT parameters (determining the model covariance matrix $\mathbf{C}_i^M$) and misfit of the best model at that grid point

$$a_i = \frac{1}{c}\sqrt{(2\pi)^6 \det \mathbf{C}_i^M} \exp\left(-\frac{1}{2}\text{misfit}_i\right) \Delta V_i \ . \tag{3.8}$$

3.2 Derivation of equation 3.5

Here we prove the transformation from the second line of 3.5 to its third line. Let's denote (symbol $\coloneqq$ stands for definition)

$$\begin{aligned} S(\boldsymbol{m}) &\coloneqq (\mathbf{G}\boldsymbol{m} - \boldsymbol{d}_{obs})^T \mathbf{C}_D^{-1} (\mathbf{G}\boldsymbol{m} - \boldsymbol{d}_{obs}) \\ S(\widetilde{\boldsymbol{m}}) &\coloneqq (\mathbf{G}\widetilde{\boldsymbol{m}} - \boldsymbol{d}_{obs})^T \mathbf{C}_D^{-1} (\mathbf{G}\widetilde{\boldsymbol{m}} - \boldsymbol{d}_{obs}) \\ S'(\boldsymbol{m}) &\coloneqq (\boldsymbol{m} - \widetilde{\boldsymbol{m}})^T \mathbf{C}_M^{-1} (\boldsymbol{m} - \widetilde{\boldsymbol{m}}) \ . \end{aligned} \tag{3.9}$$

Then we want to prove $S(\boldsymbol{m}) = S(\widetilde{\boldsymbol{m}}) + S'(\boldsymbol{m})$.

We will use the definition of $\widetilde{\mathbf{C}}_M$ and $\widetilde{\boldsymbol{m}}$

$$\widetilde{\mathbf{C}}_M = \left(\mathbf{G}^T \mathbf{C}_D^{-1} \mathbf{G}\right)^{-1} \tag{3.10}$$

$$\widetilde{\boldsymbol{m}} = \widetilde{\mathbf{C}}_M \mathbf{G}^T \mathbf{C}_D^{-1} \boldsymbol{d}_{obs} \tag{3.11}$$

and transposition of matrix product

$$(\mathbf{AB})^T = \mathbf{B}^T \mathbf{A}^T \ . \tag{3.12}$$

Matrices $\mathbf{C}_D$ and $\widetilde{\mathbf{C}}_M$ are symmetric by their definition, so their inverse is symmetric also. Then $\left(\mathbf{C}_D^{-1}\right)^T = \mathbf{C}_D^{-1}$ and $\left(\widetilde{\mathbf{C}}_M^{-1}\right)^T = \widetilde{\mathbf{C}}_M^{-1}$.

Now we replace $S'(\boldsymbol{m})$ and $S(\widetilde{\boldsymbol{m}})$ by their definitions and after some algebra we obtain definition of $S(\boldsymbol{m})$. For clarity, we strike out terms which are identity after multiplication in one direction (e.g. $\cancel{A A^{-1}}$). The terms which are at one place added and at another subtracted are stricken out in another direction (e.g.

$+\cancel{A} - \cancel{A}$).

$$
\begin{aligned}
&S'(\boldsymbol{m}) + S(\widetilde{\boldsymbol{m}}) = \\
&= (\boldsymbol{m} - \widetilde{\boldsymbol{m}})^T \, \widetilde{\mathbf{C}}_M^{-1} \, (\boldsymbol{m} - \widetilde{\boldsymbol{m}}) + (\mathbf{G}\widetilde{\boldsymbol{m}} - \boldsymbol{d}_{obs})^T \, \mathbf{C}_D^{-1} \, (\mathbf{G}\widetilde{\boldsymbol{m}} - \boldsymbol{d}_{obs}) = \\
&= \left(\boldsymbol{m} - \widetilde{\mathbf{C}}_M \mathbf{G}^T \mathbf{C}_D^{-1} \boldsymbol{d}_{obs}\right)^T \widetilde{\mathbf{C}}_M^{-1} \left(\boldsymbol{m} - \widetilde{\mathbf{C}}_M \mathbf{G}^T \mathbf{C}_D^{-1} \boldsymbol{d}_{obs}\right) + \\
&\quad + \left(\mathbf{G}\widetilde{\mathbf{C}}_M \mathbf{G}^T \mathbf{C}_D^{-1} \boldsymbol{d}_{obs} - \boldsymbol{d}_{obs}\right)^T \mathbf{C}_D^{-1} \left(\mathbf{G}\widetilde{\mathbf{C}}_M \mathbf{G}^T \mathbf{C}_D^{-1} \boldsymbol{d}_{obs} - \boldsymbol{d}_{obs}\right) = \\
&= \boldsymbol{m}^T \left(\mathbf{G}^T \mathbf{C}_D^{-1} \mathbf{G}\right) \boldsymbol{m} + \cancel{\boldsymbol{d}_{obs}^T \mathbf{C}_D^{-1} \mathbf{G} \widetilde{\mathbf{C}}_M \widetilde{\mathbf{C}}_M^{-1} \widetilde{\mathbf{C}}_M \mathbf{G}^T \mathbf{C}_D^{-1} \boldsymbol{d}_{obs}} - \\
&\quad - \cancel{\boldsymbol{d}_{obs}^T \mathbf{C}_D^{-1} \mathbf{G} \widetilde{\mathbf{C}}_M \widetilde{\mathbf{C}}_M^{-1} \boldsymbol{m}} - \cancel{\boldsymbol{m}^T \widetilde{\mathbf{C}}_M^{-1} \widetilde{\mathbf{C}}_M \mathbf{G}^T \mathbf{C}_D^{-1} \boldsymbol{d}_{obs}} + \qquad (3.13) \\
&\quad + \cancel{\boldsymbol{d}_{obs}^T \mathbf{C}_D^{-1} \mathbf{G} \widetilde{\mathbf{C}}_M \mathbf{G}^T \mathbf{C}_D^{-1} \mathbf{G} \widetilde{\mathbf{C}}_M \mathbf{G}^T \mathbf{C}_D^{-1} \boldsymbol{d}_{obs}} + \boldsymbol{d}_{obs}^T \mathbf{C}_D^{-1} \boldsymbol{d}_{obs} - \\
&\quad - \cancel{\boldsymbol{d}_{obs}^T \mathbf{C}_D^{-1} \mathbf{G} \widetilde{\mathbf{C}}_M \mathbf{G}^T \mathbf{C}_D^{-1} \boldsymbol{d}_{obs}} - \cancel{\boldsymbol{d}_{obs}^T \mathbf{C}_D^{-1} \mathbf{G} \widetilde{\mathbf{C}}_M \mathbf{G}^T \mathbf{C}_D^{-1} \boldsymbol{d}_{obs}} = \\
&= (\mathbf{G}\boldsymbol{m})^T \, \mathbf{C}_D^{-1} \, (\mathbf{G}\boldsymbol{m}) + \boldsymbol{d}_{obs}^T \mathbf{C}_D^{-1} \boldsymbol{d}_{obs} - \boldsymbol{d}_{obs}^T \mathbf{C}_D^{-1} \mathbf{G}\boldsymbol{m} - \boldsymbol{m}^T \mathbf{G}^T \mathbf{C}_D^{-1} \boldsymbol{d}_{obs} = \\
&= (\mathbf{G}\boldsymbol{m} - \boldsymbol{d}_{obs})^T \, \mathbf{C}_D^{-1} \, (\mathbf{G}\boldsymbol{m} - \boldsymbol{d}_{obs}) = \\
&= S(\boldsymbol{m})
\end{aligned}
$$

3.3 Marginal probability density

Marginal probability density of the inverted parameters as well as marginal probability densities of some parameters non-linearly related to MT (e.g. strike angle or double-couple percentage, which are not directly inverted, but can be calculated from the inverted moment tensor components) can be determined. To manage this, we generate random samples of MT from a multivariate normal (Gaussian) distribution at each grid point specified by its mean $\widetilde{\mathbf{m}}_i$ and model parameters covariance matrix $\widetilde{\mathbf{C}}_i^M$ (determined in Eqs. 3.1 and 3.2). The number of random samples at each grid point i is proportional to a_i, i.e. PPDF integrated over the MT parameters in the specific grid point (Eq. 3.8). Having an ensemble of random samples drawn from the total PPDF, we can easily plot histograms of parameters of interest (both inverted as well as their combinations) or scattering of nodal planes. Examples are given later.

4. Sources of uncertainty

Before solving any inverse problem, we should analyze possible errors and uncertainty of parameters. By "error", we mean some quantity which was measured improperly, a device which is working in a wrong way, or an incorrect assumption; e.g. we calculate with a gain value of an instrument which was changed to different type in a meantime, there is high contact resistance on a cable between sensor and digitizer, or a sensor is oriented to the east instead of north. Contrary to this, "uncertainty" is something what was measured or assumed correctly, but the "true" value cannot be obtained exactly, because of limited knowledge of the earth structure, limited accuracy of the instrumentation, and/or simplifications in the theory and calculations. Typical examples of uncertainty are 1-D velocity model, instrument and seismic noise, point-source assumption etc. In this chapter, we describe the most common sources of both error and uncertainty, which we face in moment tensor inversion. Where possible, we also give a hint, how to deal with such issues.

The uncertainty analysis is important, because each measured or determined value (including a CMT solution) should be accompanied by estimation of its uncertainty. Correctly estimated uncertainty defines a region in the model parameters space, where the true solution lies with a certain probability. If any of uncertainty source is ignored, the evaluated uncertainty may be biased.

4.1 Instrument parameters

Each instrument (seismic sensor together with digitizer) outputs some (typically three-component) time series. The record are related to the ground motion by instrument parameters, i.e. sensitivity and instrument response (typically in a form of poles and zeros describing the response polynomial). These parameters are provided by station operator and sometimes they could be outdated, e.g. in cases when the instrument was changed to a different type or its configuration was altered and the information in database was not updated. These problems can be detected by anomalous amplitudes of seismic signal and/or seismic noise and the problem should be communicated with station operator and the stations should be excluded from the processing, if no up-to-date parameters are provided by the operator. An example how the stations with such problems can be detected in a large dataset we provide in paper Málek et al. [2017].

Some other errors are related to the sensor orientation. It may be caused by inaccurate orientation of the sensor during its installation (orientation using classical compass affected by magnetic metals nearby, neglecting magnetic declination, inaccuracy of measurement) as well as by making a serious mistake like orienting an arrow on sensor to the north in case it should be to the east, or plugging cables in a incorrect way resulting in exchange of components and/or their polarity reversal. Such problems can be detected on large datasets taking angles describing sensor orientation as unknowns in the inverse problem or by plotting difference between P-wave polarization and theoretical back-azimuth [Vecsey et al., 2017].

Another possible problem is the incorrect record timing. Time synchroniza-

tion is usually provided by GPS-receiver and when the receiver loses signal, it is unplugged or there is another problem, the difference between device clocks and exact time starts to increase. A small time difference can be hardly detected in a single case, although it can cause serious problem in the inversion. It can be sometimes detected from digitizer log files, but we usually do not have access to them if the station is operated by anyone else.

The last possible source of error is a difference between real and assumed location of the instrument. It may be caused, e.g., by a wrong transformation of geodetic coordinates. Neglecting of sensor altitude can also have a similar effect.

We cannot detect most of these disturbances from single-event data, but most of them is detectable on large datasets. Very promising study was done by Vecsey et al. [2017]. We should keep in mind, that in cases where a station cannot be fitted in the inversion, the problem could be both in the inversion as well as in the station.

4.2 Instrument disturbances

The seismographs are quite complex instruments with a wide scale of possible technical problems. Some of them are easily detectable just by a visual inspection of an earthquake records, e.g. some of components contain just a flat line or an instrument noise instead of earthquake waveform. Such problems are not really dangerous for a CMT inversion; the problematic component(s) has zero fit, so it decreases total variance reduction, but it should not affect the result value significantly.

We must also understand correctly which physical quantity does the instrument measure. The broad-band seismometers, which we use mostly in this work, have velocity on the output (if using frequencies on the flat part of the response). They work on the principle of force balance of inertial mass. It is obvious from the physical principle itself, that the instrument reacts not only to ground translation, but also to rotation, because ground tilt results in a projection of gravitational acceleration to the horizontal components [Pillet and Virieux, 2007]. The rotations are present in the wave field of S-waves and surface waves of all types and they can be measured by special instruments [Brokešová and Málek, 2010]. The effect on the record of standard seismometer may be much stronger in case of ground tilt, which is the effect of near-field deformation of the seismic source or earthquake-triggered inelastic movement of instrument installation. In such cases, the disturbance caused by the tilt is present in the seismogram in the same time as the earthquake signal. This makes the disturbance more dangerous for two reasons: first it may be easily overlooked in band-pass record due to its long-period character, second it may affect significantly the result of a CMT inversion, as well as other calculations made from the waveform.

In seismological practise, we face several types of earthquake-triggered instrumental disturbances. Some of them may be modeled as a step in the input acceleration, velocity, or displacement (first two types described in Zahradník and Plešinger [2010], the third according to Zahradník [pers. comm.]). Internally, we call them "mouse" of the first, second, and third type, respectively. The first type might be caused by a ground tilt, the others are probably of purely instrumental origin. Similar effect may be caused also by seismograf overloading (record clip-

ping) and subsequent integration. We studied the first type, which seems to be the most common, in detail in paper Vackář et al. [2015], which is included in this thesis as Chapter 5. The first type is automatically detected in our software and such records are skipped from the inversion in the developed method (see Section 7.4). We want to include the other types to the automated detection in the future, as well as detection of record clipping.

4.3 Noise

We use the term "seismic noise" as all signals in the waveforms generated by all other sources than the earthquake of interest. So the noise includes, e.g., microseism caused by ground-ocean and ground-wind interaction on large scales, local wind effects on vegetation, antropogenic noise (traffic, heavy industry etc.), as well as other earthquakes. Although some of these sources are random (e.g. two earthquakes from different locations may be observed in the same time at the station), most of them is more or less stationary in short-time window. Assuming this stationarity, we can estimate the noise level and its properties in the inverted record from a before-event noise. We use this approximation for construction of the data covariance matrix in Chapter 6. In the developed method, we estimate the noise properties for each component of each station separately, as well as the correlation between components of any single station.

Usually, the inversion should be restricted on the frequencies where the seismic waves generated by the earthquake (called signal) are stronger than the noise. This is not necessary in our developed method, because the noisy frequencies are automatically filtered out using the data covariance matrix.

4.4 Green's function modeling

The Earth structure is complex on all scales from molecular to tectonic plates. Although there is a significant progress in the knowledge of Earth interior, we could never know it in all details. This is a limitation for seismic source studies, because we need to model seismic waves. The quality of the (seismic wave velocity) model makes a high frequency limit for the frequency band in the inversion, for more detail see Subsection 7.6.1.

Beside a case study in Chapter 2, we do not deal with this issue in this thesis. Some promising results were reached by Hallo and Gallovič [2016]. They used used a branch[1] of code `ISOLA-ObsPy`, where they include their developed estimation of Green's functions uncertainty. The merging of this branch with the mainline of the code is one of our future plans, so the code should take into account both noise as well as modelling error in the inversion and uncertainty evaluation.

[1] Branching (in programming and software management) is the duplication of a code so that modifications can happen in parallel along both branches.

4.5 Other sources of uncertainty

There are a few other issues which are connected with the result uncertainty. First of them is the limited number of seismic recordings and their spatial distribution. In the developed code, the source-station configuration is taken into account and it affect both condition number and the CMT uncertainty (see synthetic test in section 8.1.1). Another sources of uncertainty are simplifications in the mathematical description of the earthquake source (point source approximation, fixed source time function etc.). We deal with some of them, e.g. we omit stations too close to the epicenter, where the point source approximation is invalid. The other simplifications cannot be handled in a simple way. The code is mainly developed to application to small to moderate earthquakes recorded in regional distances, where the used approximations are more or less valid. For other applications, it is up to user to decide whether the approximations in the code are still appropriate.

5. Automated detection of long-period disturbances in seismic records; MouseTrap code

Paper by J. Vackář, J. Burjánek, and J. Zahradník, published in 2015 *Seismol. Res. Lett.*, **86**, pp. 442–450.

5.1 Introduction

Sudden disturbances in strong-motion acceleration records, referred to as baseline offsets, are well known [Boore et al., 2002; Javelaud et al., 2011]. The physical nature of this phenomenon remains unclear, although some cases are well explained by a permanent ground tilt [Graizer, 2010; Javelaud et al., 2012]. The ground tilt may be caused by near-field source effects, or a local tilt at a station produced by seismic vibrations in highly heterogeneous substrata (i.e., strong gradients of material properties at small scales). Tilts are frequently observed in volcanic areas [Wielandt and Forbriger, 1999; Wiens et al., 2005]. Delorey et al. [2008] performed an experiment showing that tilting of the instrument produces a long-period disturbance of the characteristic shape.

In these cases, the disturbances predominate on horizontal components. The disturbances can also have a purely instrumental origin [Boore, 2003; Iwan et al., 1985; Shakal and Petersen, 2001]. The latter is a more suitable explanation in cases where the disturbances are also strong on the vertical component.

Similar artifacts have also been reported on different types of broad-band seismometers worldwide [Delorey et al., 2008; Pillet and Virieux, 2007; Zahradník and Plešinger, 2005]. A strong disturbance is frequently characterized by a one-sided pulse in raw output velocity. A weaker disturbance is often masked by high-frequency content of the velocity record. However, it can be easily visible in the integrated output of a broad-band instrument (raw displacement) where it looks like a baseline step, whose duration equals to the seismometer corner period (Fig. 5.1A).

The disturbances may easily be overlooked in band-pass filtered records. Using such disturbed records can lead to wrong results in many seismic applications, e.g. the moment-tensor inversion [Zahradník and Plešinger, 2005; Zahradník et al., 2008]. Similar problems might arise in the spectral estimation of the moment magnitude; the disturbed records may erroneously pass through a routine data quality control, e.g. the signal-to-noise (S/N) control [Sokos and Zahradník, 2013], because the disturbances yield apparently very large values of the S/N ratio. As seen in Fig. 5.1B, the disturbances cause significant spurious increase of the spectrum at low frequencies. The signal spectrum is contaminated up to frequencies much higher than the low-frequency corner of the instrument.

The main objective of this study was to develop a code for an automated detection of such disturbances aimed at removing them from the routine seismic data processing. Such a tool would also allow for systematic studies of the disturbances in order to identify and explain their origins. As an application we

analyzed the disturbances in 18 years of recordings in the Swiss Digital Seismic Network.

The developed code is available as an ObsPy module (under GNU/GPL license).

5.2 Modeling the disturbances: forward problem

Many of the observed disturbances can be modeled as a seismometer response to an acceleration step on the input [Zahradník and Plešinger, 2005] (Fig. 5.1A). Thus, a characteristic one-sided pulse appears in the raw velocity output, which results in a baseline offset in the raw displacement (Fig. 5.2). Note that the step visible in the raw displacement is not a permanent displacement, but a permanent acceleration (see the acceleration scale at the right-hand side of Fig. 5.2D). It is because the integrated broad-band output is proportional to displacement only at frequencies above the low-frequency corner of the instrument, while it is proportional to acceleration at the low-frequency limit. Consequently, a simple integration of the instrumentally uncorrected record in its full frequency band will reveal the characteristic shape of the disturbance (smoothed ramp, see Fig. 5.1A).

Because of its shape, we name the disturbance an "artificial fling step" (for brevity also "fling step" in the following text). Such disturbances are well known to users of moment-tensor inversion software ISOLA [Sokos and Zahradník, 2008, 2013], because removal of disturbed records is necessary. Informally, in the community of ISOLA users, such disturbances are referred to as "mouse". We use this informal name in the developed code.

The time series $m_d(t)$ of the raw displacement disturbance caused by a unit acceleration step with zero onset time is described by

$$m_d(t) = \int_{-\infty}^{t} \int_{-\infty}^{+\infty} s(\tau)\tau h(t-\tau)\mathrm{d}\tau\mathrm{d}t \ , \tag{5.1}$$

where $h(t)$ is an impulse response of the instrument to input velocity and $s(t)$ is the input unit acceleration step, i.e. the Heaviside function ($s(t) = 1$ for $t \geq 1$ and $s(t) = 0$ for $t < 0$). The inner integral is a time convolution of the input velocity ramp $s(\tau)\tau$ and instrument response $h(\tau)$. The outer integral transforms the velocity to displacement.

The disturbances often occur simultaneously on three component recordings; in another words, the causative acceleration step has three components as well. Thus we use 4 parameters for the description of a real fling step: time t_0 of the onset of the input acceleration step, amplitude A of the acceleration step and two spatial angles—horizontal azimuth ϕ and its inclination θ from the horizontal plane. The east, north and vertical components of the raw displacement disturbance recording are therefore

$$m_E(t) = m_d(t - t_0)A \sin\phi \cos\theta \tag{5.2}$$

$$m_N(t) = m_d(t - t_0)A \cos\phi \cos\theta \tag{5.3}$$

$$m_Z(t) = m_d(t - t_0)A \sin\theta \tag{5.4}$$

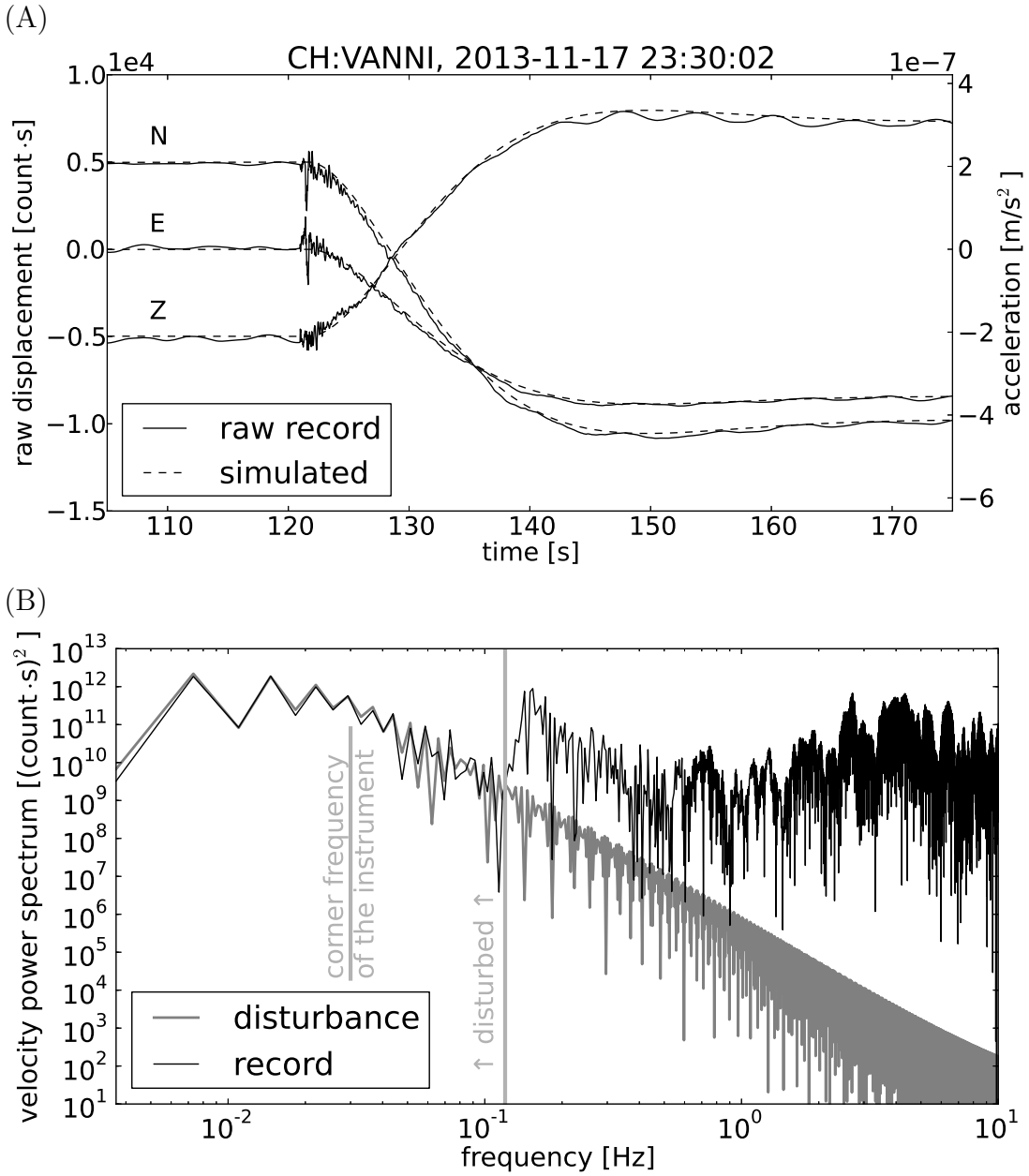

Figure 5.1: **A)** Example of a fling step disturbance in the integrated output (raw displacement) of the Nanometrics Trillium T40 seismometer. The disturbance is well fitted by the simulated instrument response to an acceleration step of amplitude $A = 8.7 \cdot 10^{-7}\,\mathrm{m \cdot s^{-2}}$, azimuth $\phi = 209.7°$, and inclination $\theta = 35.9°$. The recorded earthquake has magnitude $M_{Lh} = 1.7$ (Swiss Seismological Service), its epicentral distance is 1.9 km. **B)** Power spectrum of raw velocity (Z component) and of the disturbance. The disturbance dominates in the spectrum up to frequency ∼0.12 Hz.

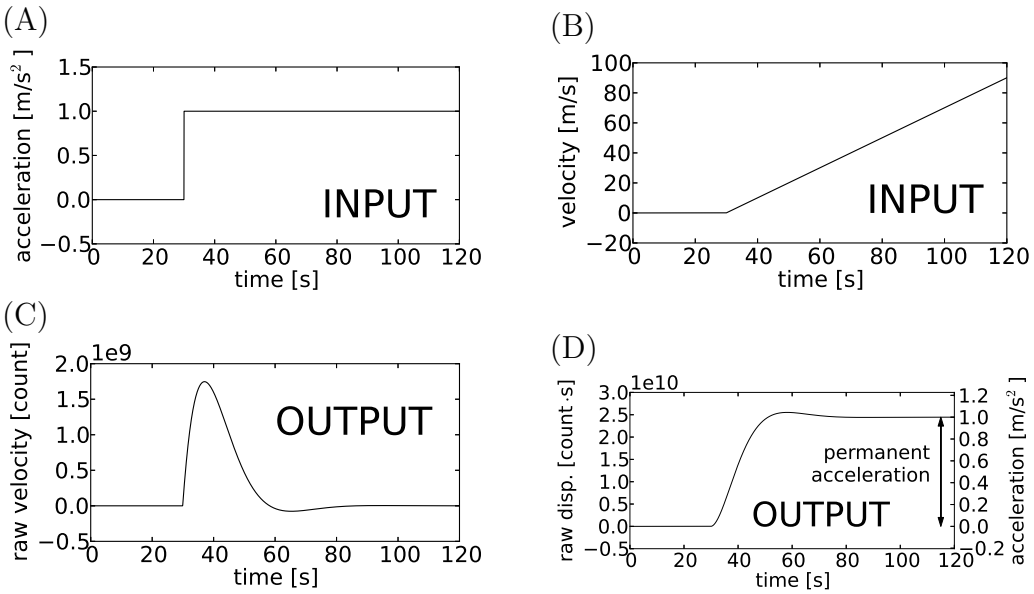

Figure 5.2: Modeling fling step disturbance. The input acceleration step (A) is equivalent to the velocity ramp (B). After applying the instrumental response (here for Nanometrics Trillium T40) we get a characteristic one-sided pulse in the output raw velocity (C), and a fling step disturbance in the raw displacement (D). The right-hand scale of panel D corresponds to the low-frequency limit of integrated broad-band output which is proportional to acceleration.

5.3 Fitting the disturbances: inverse problem

Explaining a recorded disturbance by the synthetic fling step formally means solving an inverse problem with 4 parameters: t_0, A, ϕ, and θ. In order to have a unique solution, A must be positive and the angles ϕ and θ are in intervals 0–360° and −90 to +90°, respectively. The inverse problem is solved by the least-squares method (LSQ) to minimize the L^2-norm difference between the observed record and synthetic fling step. The agreement is quantified by variance reduction (VR). Analytical expressions of the partial derivatives with respect to A, ϕ, and θ are used in the LSQ fitting (see Appendix A for details). The values of t_0 are selected from a grid of values and the inverse problem is solved for the other three parameters in each grid point; then the corresponding parameters for t_0 with the highest VR are selected.

Besides VR we also need to define a criterion—whether the fling step is present or absent. To this goal we evaluate an existence criterion

$$mp = VR - \frac{|t_0 - t_S|}{const} \,, \tag{5.5}$$

where t_S is the S-wave arrival. The term $|t_0 - t_S|/const$ serves to penalize fling step disturbances not related to the earthquake in order to exclude false detection due to noise. The penalty term was motivated by the observation that most fling steps occur shortly after the S-wave arrival ($t_0 \geq t_S$). The term *const* is a numerical constant chosen to be much larger than $t_0 - t_S$ in case of earthquake-induced fling step ($const = 50$ s in application of this paper, chosen ad hoc after few preliminary tests). If the *const* is too low, the earthquake-induced fling steps

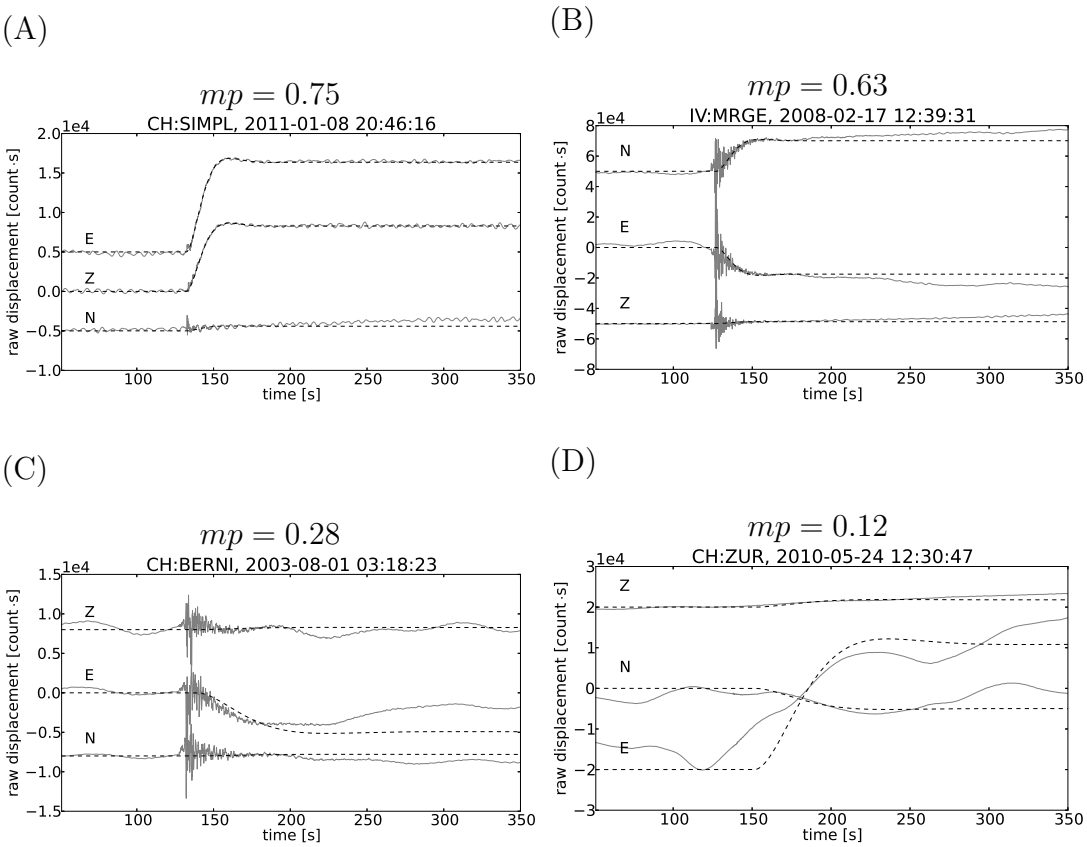

Figure 5.3: Agreement between observed records (solid line) and fitted synthetic disturbances (dashed line) for different values of the existence criterion mp.

might be excluded; if it is too high, many cases where the long-period noise is fitted by synthetic fling step, such as in Fig. 5.3D, are taken into account. After visually inspecting dozens of disturbances with various mp values, we set up an empirical criterion that the cases with $mp > 0.7$ are fling steps, $mp < 0.2$ are not fling steps, and cases $0.2 < mp < 0.7$ require visual inspection to distinguish whether the fling step is present or not. There are examples of records and fitted synthetic disturbances in Fig. 5.3: Record of station SIMPL (Fig. 5.3A, $mp = 0.75$) is a typical example of a strong disturbance. Record of MRGE (Fig. 5.3B, $mp = 0.63$) is unclear: when we look at record in detail, the baseline trend starts seconds before the earthquake and its shape differs from the synthetic disturbance. At station BERNI (Fig. 5.3C, $mp = 0.28$) the disturbance might be present, although it is weak and the shape is not fitted perfectly. In record of ZUR (Fig. 5.3D, $mp = 0.12$) there is a relatively well fitted long-period noise, but with relation neither to an earthquake nor to the studied disturbance.

5.4 MouseTrap code

We implemented the described approach into an ObsPy module called `MouseTrap`. The module consists of the following functions:

mouse.create Calculates the instrument output for a given transfer function and a unit acceleration step on the input.

PrepareRecord Removes the before-event mean value, integrates record into displacement, and analyzes the signal-to-noise ratio of the record (ratio of before-event maximum to record maximum). Testing signal-to-noise ratio is necessary to prevent explaining strong long-period noise as a disturbance.

mouse.fit_3D Fits a given three-component record with a synthetic fling step.

mouse.exist Distinguishes whether the fling step is present according the fit value, synthetic fling step amplitude and its ratio to record amplitude. The output can be optionally the binary value (0, 1), or the *mp* value.

mouse.params Returns the parameters t_0, A, ϕ, and θ of the detected fling step.

mouse.plot Plots the comparison between observed record and synthetic fling step.

The module is published under GNU/GPL license, and available at `http://geo.mff.cuni.cz/~vackar/mouse`. The detailed documentation and a few examples are also on the website. Running the code requires Python interpreter (version 2.7.x) with ObsPy [Beyreuther et al., 2010] and Matplotlib [Hunter, 2007] libraries installed. The module can be used for two tasks—the fling step detection in a single record, or the detection of fling steps in a set of records of a seismic network. The latter requires earthquake catalog in machine-readable or database form.

5.5 Automated detection of disturbances in a seismic network

Here we demonstrate the code capabilities through a systematic detection of fling steps using a database of seismic records. The source code of this procedure (`SwissMouse`) can be found at the website mentioned above and the results of its application to Swiss Digital Seismic Network are described in the following section. The algorithm flowchart is shown in Fig. 5.4.

The procedure starts with event selection from the database. For each earthquake, a set of stations is selected in the distance range according to magnitude and the Swiss ground motion prediction equation (GMPE) [Cauzzi et al., 2014; Edwards and Fäh, 2013]. We take into account the stations where the exceedance of a fixed acceleration value is expected. As a posteriori verification we checked that only few detected disturbances lie next to the cut-off line of the criterion. Waveform data and poles and zeros (PAZ) are downloaded from the ArcLink server. The signal-to-noise ratio (ratio of before-event maximum to record maximum) is tested, and the unfavorable records are skipped. Simple parameters of the records, such as epicentral distance and azimuth, as well as the PGA, PGV, and PGD values are evaluated. In addition to standard PGA and PGV values, these values were also calculated in different frequency bands, i.e. the record was band-pass filtered and then maximal values determined. Next, the fling step modeling is applied using the `MouseTrap` code and the inverted parameters of the fling step are stored in an SQL database. The entire process is fully automated,

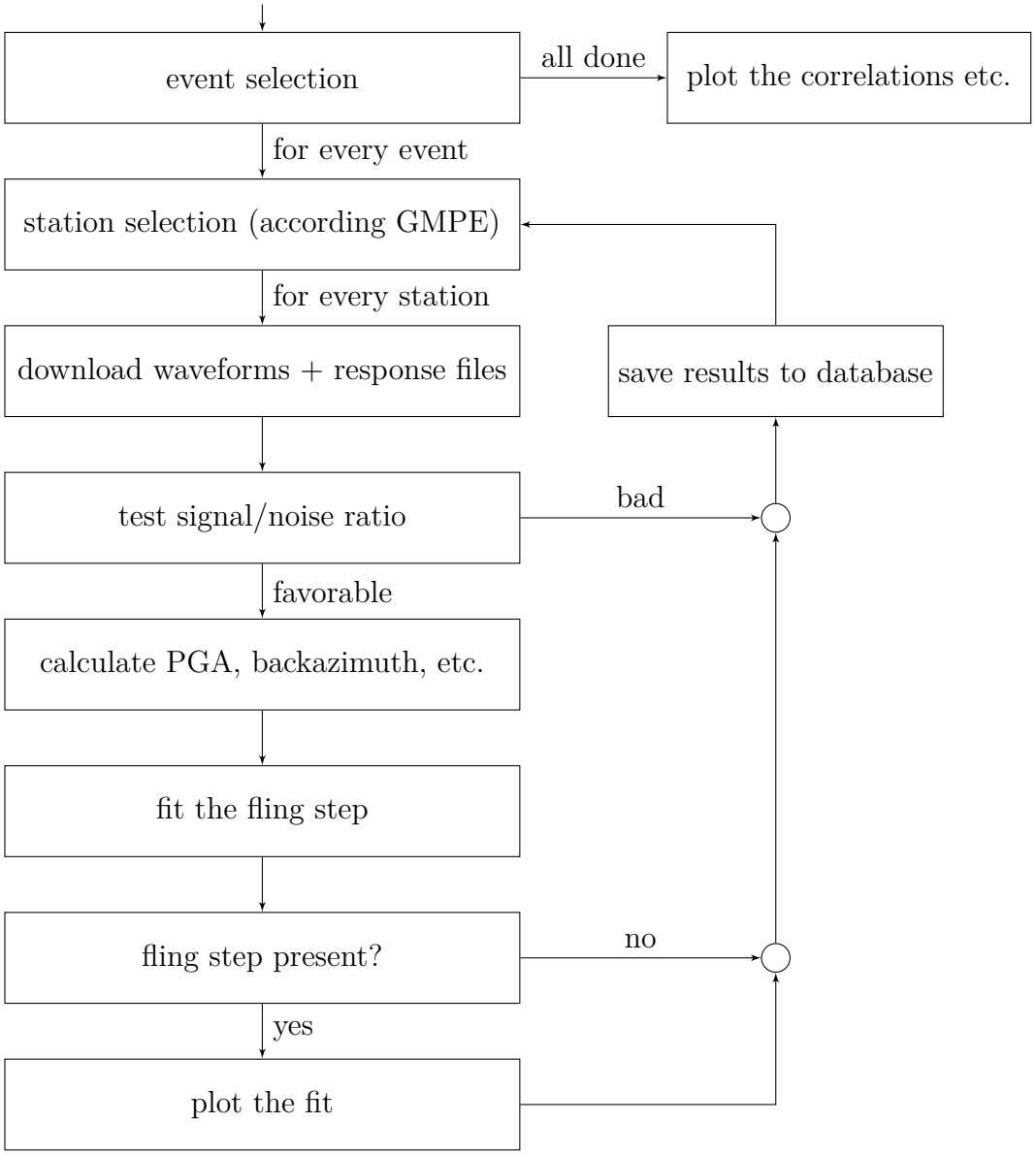

Figure 5.4: Flowchart of the systematic detection of fling steps with database of records using `SwissMouse` code.

but the comparison between observed and synthetic waveform is also plotted for possible visual inspection. Last but not least, correlation plots and histograms, which are discussed in the following chapter, are automatically plotted using pre-defined SQL queries.

5.6 Case study: disturbance detection in 18 years of record of Swiss Digital Seismic Network

We examined 18 years of records of Swiss Digital Seismic Network using the developed `MouseTrap` and `SwissMouse` codes. The purpose was to test the detection algorithm and obtain a set of fling steps for a rough evaluation of their properties.

The magnitude-distance criterion was met by 6,240 broad-band records, but

Table 5.1: Statistics of the analyzed records. The records were analyzed by code `SwissMouse` while it was applied on 18-years set of Swiss data.

Records total	**6,240**
Skipped records	5,114
problems with download	1,087
unfavorable signal-to-noise ratio	3,965
gap in data	42
no poles-and-zeros file	20
Analyzed records	**1,126**
no fling step detected	914
fling step is unclear (visual inspection necessary)	129
fling step detected with no doubt	**83**

only 1,126 records were passed to further analysis (see Tab. 5.1 for details). From the analyzed records, in 83 cases a fling step was detected with no doubt ($mp > 0.7$). Most of the detected disturbances are in records where the seismic signal is significantly below the saturation level. Another 129 cases were unclear ($0.7 > mp > 0.2$), and a visual inspection was necessary for decision about the fling step existence.

The main properties of fling steps in our dataset can be briefly summarized as follows: Some directions of the fling step are more frequent. Namely, many of fling steps were observed in azimuth ϕ equal to 30°, 270°, and 150°, or the opposite directions (Fig. 5.5A). These azimuths coincide with directions of the three inclined pendulums in Galperin's design seismographs (like Streinecken STS-2 and Nanometrics Trillium T40, which are the most frequent broad-band instruments in the Swiss Digital Seismic Network). Most of the disturbances are horizontal ($\theta = 0$), but a significant number have the inclination θ close to ±35° (Fig. 5.5B). The inclination of the pendulums in the Galperin's seismographs is 35.3°. Therefore, these observations might indicate the instrumental origin of the disturbances. Looking at individual stations, there are stations where most of the fling steps are horizontal, but correlated neither with the azimuth of the pendulum, nor with the back-azimuth of the event, and there are some other stations where most of the fling steps are in the azimuth and inclination of one preferred pendulum (Fig. 5.5C and Fig. 5.5D).

Fling steps are more common near the epicenter and at higher magnitudes (Fig. 5.6A). This is probably related to stronger ground shaking, but does not correlate well with PGA, PGV, or PGD. Beside these parameters the ratio fling-step / no-fling-step is also dependent on epicentral distance (Fig. 5.6B).

We also evaluated the fling-step / no-fling-step ratio at different seismograph types (Fig. 5.7A). The ratio is similar for all three types of the broad-band instruments used in Swiss Digital Seismic Network. There are minor differences between broad-band instruments, but this result is partly influenced by the presence or absence of events near to the investigated stations.

When we looked at fling step count at the individual investigated stations (Fig. 5.7B), a large variability was found, ranging from stations very rich in fling steps to stations with no fling step at all. Some of the stations where fling steps are common are situated very close to some earthquakes, so fling steps are mostly

caused by near events (e.g. stations VANNI, FUORN). But there are also stations (e.g. SIMPL, AIGLE), where the fling step occurrence is high independently of the epicentral distance of the event (Fig. 5.7C and Fig. 5.7D).

Finally, the disturbance occurrences in Swiss network have no simple rules and can be hardly predicted. There are stations, where the disturbance occurrence is much more probable; which might indicate some instrumental problem. Nevertheless we demonstrated their systematic existence especially at stations within short epicentral distances. Such stations are crucial in moment tensor inversions of weak events. The tool developed here is capable to detect and characterize such disturbances, so the disturbed records could be easily removed from processing without considering their origin.

5.7 Conclusion and discussion

We developed a code `MouseTrap` for automated detection of fling step disturbances in seismic records. The program is available under free license at website `http://geo.mff.cuni.cz/~vackar/mouse`. The spurious input acceleration step and the instrument response explain many of the observed disturbances very well. Fitting the synthetic disturbance into real records provides four parameters of the input acceleration step, namely its onset time t_0, amplitude A, azimuth ϕ, and inclination θ. The code can be applied either to an individual record or to a set of records with metadata in a database.

We expect the code to be useful in many applications for automatic data processing, e.g. waveform inversion and S/N ratio evaluation, where detection and removal of contaminated records is a must.

We also developed the code `SwissMouse` for automated analysis of fling step existence in broad-band records of Swiss Digital Seismic Network over the last 18 years, at stations close to located events. Fling steps are present at all types of studied broad-band instruments, at many different stations. We observed a higher percentage of fling steps at some stations. Azimuths of fling steps remain the same at some (but not all) stations. In particular there is a higher occurrence of fling steps with azimuths 30°, 90°, and 150°. Most of the fling steps are horizontal, but a significant number have inclination $\sim 35°$. These preferred directions are very likely related to pendulums in Galperin's design seismometers, so these cases are probably of instrumental origin. There is a good reason (supported by limited authors' experience) to expect, that in instruments operating with pendulums in N, E, Z setup, such as e.g. Guralp CMG 3-T, the disturbances might sometimes be preferentially related to a single component. The fling steps are more common at records with higher PGA and PGV, near the source, and at higher magnitudes (M 1–4 mostly examined). Besides this paper we have also observed such disturbances at short-period instruments, where they are naturally characterized by much shorter durations than at broad-band seismometers.

There are also similar disturbances which can be described as instrument response to a spurious step in the input velocity [Zahradník and Plešinger, 2010], which can be explained as caused by saturation in the force-balance system. These might be implemented in future updates of the `MouseTrap` code, including diagnostics of a joint occurrence of both kinds of disturbances. Another challenging issue is to develop the fling step detection in continuous records.

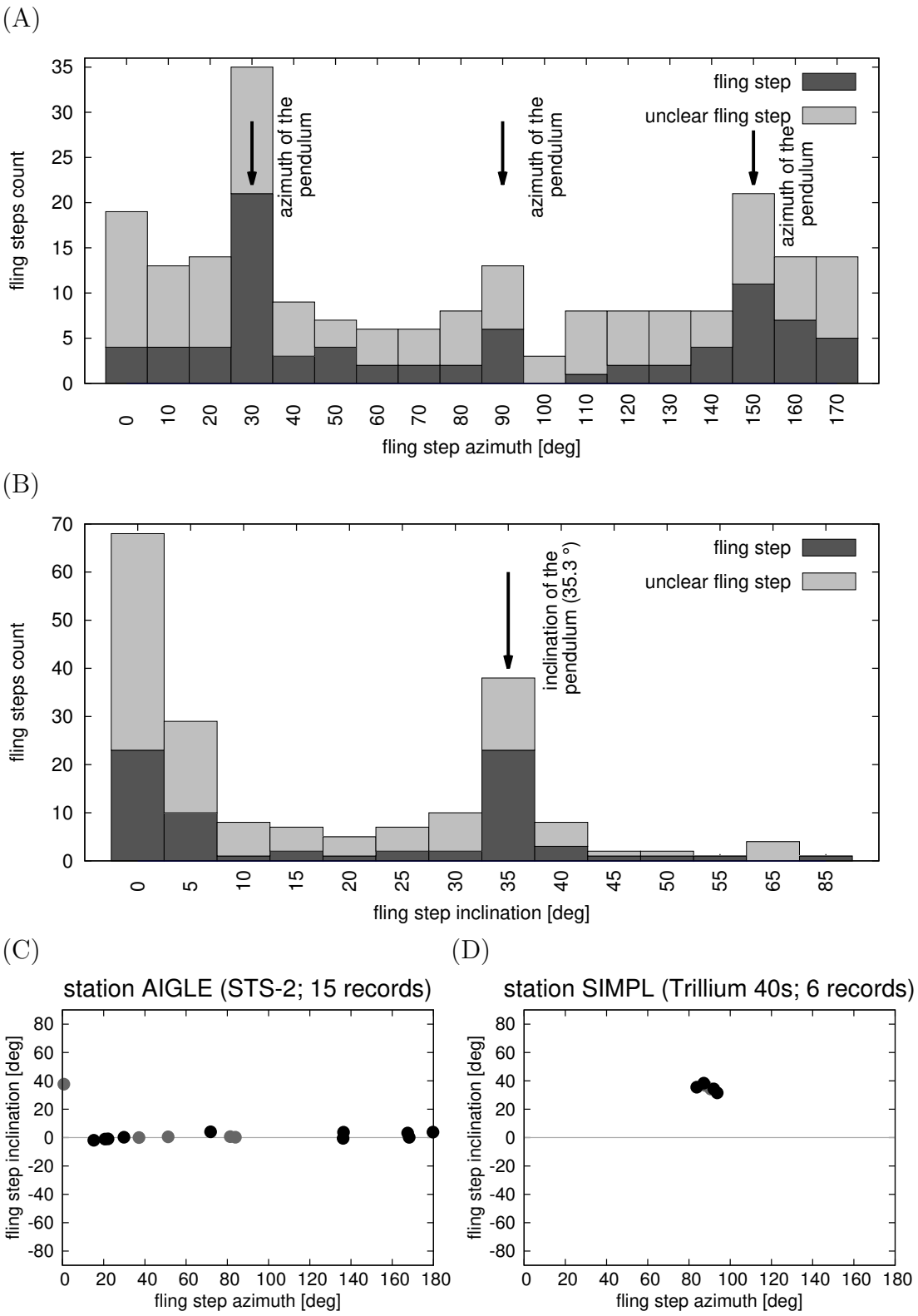

Figure 5.5: Azimuths (A) and inclinations (B) of the fling step disturbances in the 18-years dataset of disturbances detected in the Swiss Seismic Network. For better visibility, the azimuth is restricted to the interval 0–180° and inclination to 0–90° because some of disturbances are in direction of the pendulum and some in the opposite direction. There are some stations where the fling steps are nearly horizontal and in different azimuths (C), and some other stations where all the fling steps have azimuth and inclination of one preferred pendulum (D).

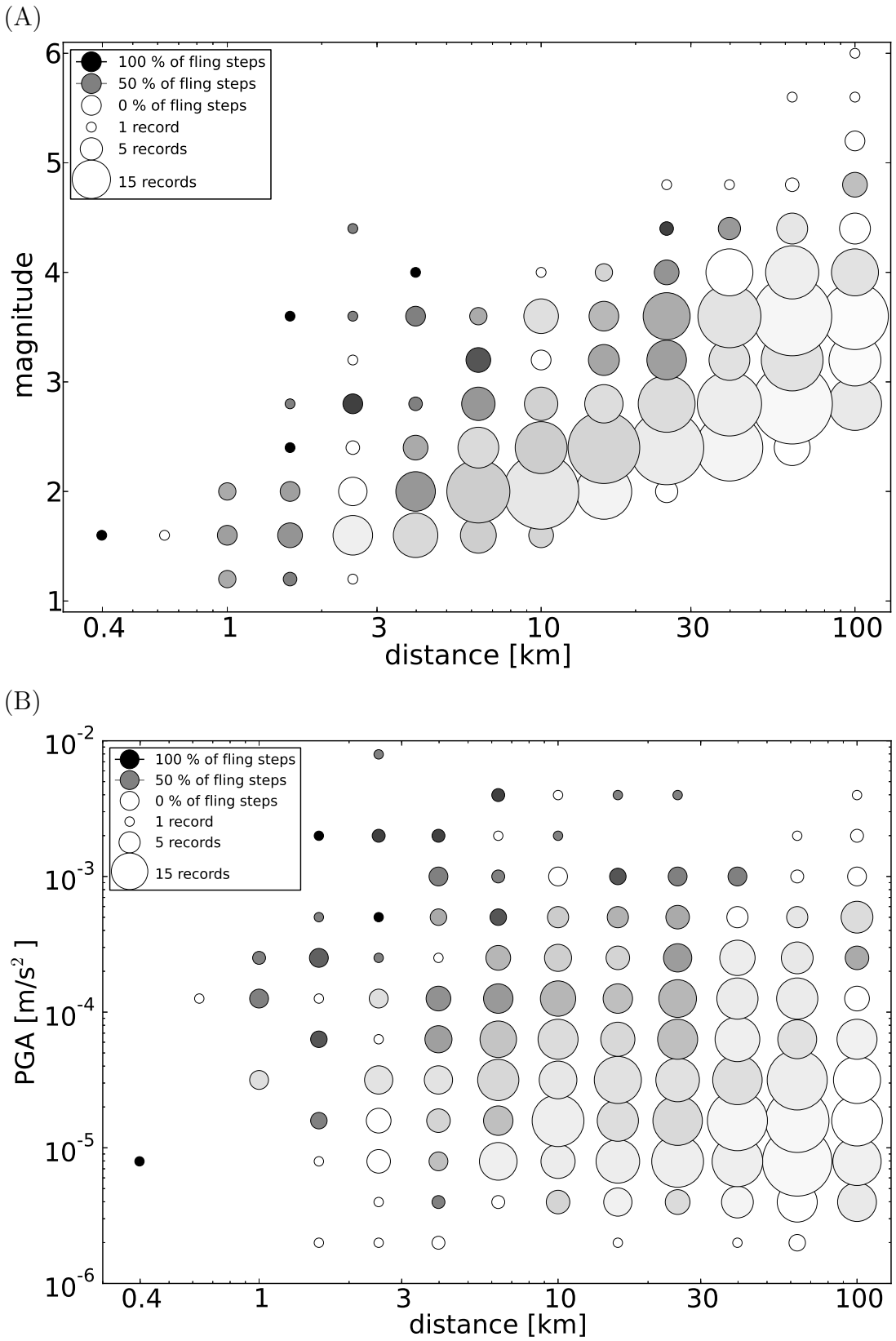

Figure 5.6: Fling steps are more common near the epicenter and at higher magnitudes (A). Fling steps are more common at higher PGA (B). The magnitude (A) comes from Swiss Seismological Service earthquake catalogue, moment magnitude M_w and local magnitudes M_L and M_{Lh} are used for different events.

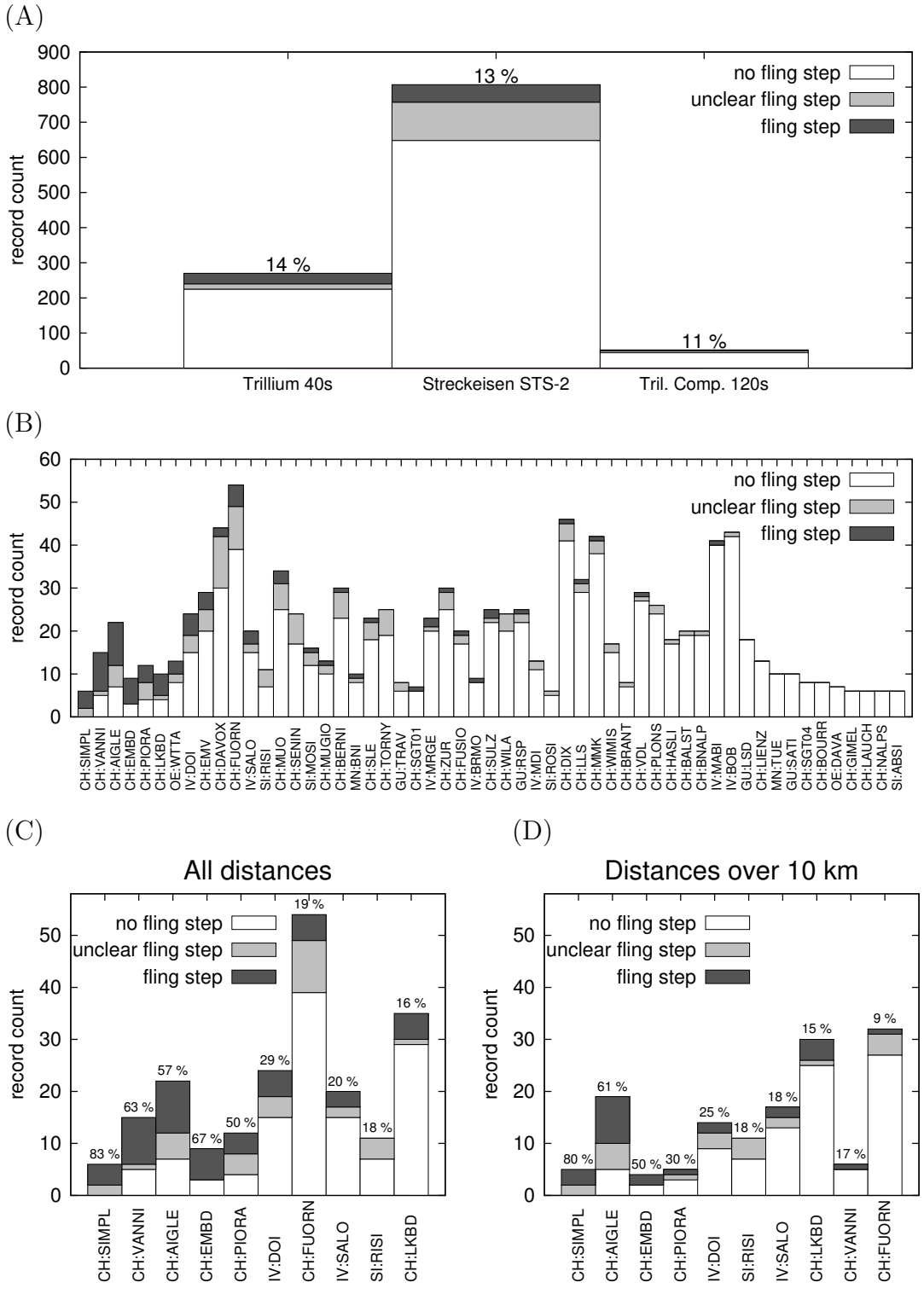

Figure 5.7: Fling steps count at studied broad-band sensors (A). Fling steps counts at the studied stations with more than 5 records (B). Fling step count at selected stations for events in all epicentral distances and for epicentral distances over 10 km (C and D).

Acknowledgement

We are grateful to Philipp Kästli for his help with using SeisComP database. We would like also to thank Yannik Behr and Carlo Cauzzi for useful advice and Benjamin Edwards for language correction. The work was supported by the Czech Republic grants SVV 2014-260096, GAČR 14-04372S, and GAUK 496213. The used dataset comes from Swiss Seismic Network operated by Swiss Seismological Service, with data from neighboring countries operated by INGV, ZAMG, and University of Genoa included.

5.8 Appendix

Analytical expressions of partial derivatives are used during least-squares fitting of observed record by synthetic fling step.

Let us have a three component record with north-south, east-west, and vertical components s_i^N, s_i^E, and s_i^Z, respectively, where i indexes time samples. We want to minimize the difference between the record and a synthetic disturbance m_i by finding proper amplitude A, azimuth ϕ, and inclination θ of the disturbance. The difference in the L^2-norm

$$\sum_i \left(s_i^N - Am_i \cos\phi\cos\theta\right)^2 + \sum_i \left(s_i^E - Am_i \sin\phi\cos\theta\right)^2 + \sum_i \left(s_i^Z - Am_i \sin\theta\right)^2 \tag{5.6}$$

should be minimal, so its partial derivatives should be zero.

From $\frac{\partial}{\partial\phi} = 0$ we get

$$\frac{\sum_i m_i s_i^E}{\sum_i m_i s_i^N} = \frac{\sin\phi}{\cos\phi} = \tan\phi\ . \tag{5.7}$$

From $\frac{\partial}{\partial\theta} = 0$ we get

$$\frac{\sum_i m_i s_i^Z}{\sum_i m_i \left(s_i^N\cos\phi + s_i^E\cos\phi\right)} = \frac{\sin\theta}{\cos\theta} = \tan\theta\ . \tag{5.8}$$

From $\frac{\partial}{\partial A} = 0$ we get

$$\frac{\sum_i m_i \left(s_i^N\cos\phi\cos\theta + s_i^E\sin\phi\cos\theta + s_i^Z\sin\theta\right)}{\sum_i m_i^2} = A\ . \tag{5.9}$$

6. Covariance matrix of the noise

This chapter is based on Section 3 of Vackář et al. [2017].

In this section we describe the construction of the data covariance matrix $\mathbf{C}_D$. In our definition, it reflects the properties of the seismic noise. We assume that seismic noise time series can be considered as a stationary Gaussian random process with zero mean. Then the data covariance matrix can be written for a discrete series $x(t_i)$, which represents a single component of seismic noise at a single station, as [Tarantola, 2005, Example 5.1]

$$\mathbf{C}_D = \begin{pmatrix} C(\tau_0) & C(\tau_1) & \cdots & C(\tau_{N-1}) \\ C(\tau_1) & C(\tau_0) & \cdots & C(\tau_{N-2}) \\ \vdots & \vdots & \ddots & \vdots \\ C(\tau_{N-1}) & C(\tau_{N-2}) & \cdots & C(\tau_0) \end{pmatrix} . \tag{6.1}$$

where $C(\tau_k)$ is a value of covariance function for a time lag τ_k and N is a number of samples in the discrete series $x(t_i)$. For estimation of the covariance function, we assume ergodicity, so that the averaging over realizations can be replaced by averaging over time. Then the covariance for discrete time series may be estimated as the auto-correlation defined by

$$C(\tau_k) \overset{\text{ergodicity}}{=} (x \star x)[\tau_k] \overset{\text{def}}{=} \frac{1}{2N+1} \sum_{m=-N}^{N} x[\tau_m]\, x[\tau_{m+k}] . \tag{6.2}$$

So far, we have assumed only a single scalar time history of the noise (i.e., a single component of the motion at a single station). Nevertheless, the data covariance matrix could be generalized for the three component noise recordings acquired at L stations. In general, one should assume all potential correlations in the recorded noise wave field, so that the full covariance matrix would consist of 3 times L matrices defined in equation (6.1). On one hand, since the noise wave field still consists of propagating seismic waves (e.g., surface waves), one cannot neglect the correlation between the components of recorded ground motion at a single station. On the other hand, we assume zero correlations between the noise recordings at different stations. This is valid assumption for stations which are far away from each other and for high frequency seismic noise, so that different noise sources dominate the recording at different stations. For stations close to each other, seismic arrays, collocated sensors, and for low frequency noise, it might be useful to take into account cross-covariance between stations. The data covariance matrix for two stations, each of them with three components (with ordering station first and then components) would be then [ibid., eq. 5.10–5.11]

$$\mathbf{C}_D = \begin{pmatrix} \mathbf{C}_{st1}^{ZZ} & \mathbf{C}_{st1}^{ZN} & \mathbf{C}_{st1}^{ZE} & 0 & 0 & 0 \\ \mathbf{C}_{st1}^{NZ} & \mathbf{C}_{st1}^{NN} & \mathbf{C}_{st1}^{NE} & 0 & 0 & 0 \\ \mathbf{C}_{st1}^{EZ} & \mathbf{C}_{st1}^{EN} & \mathbf{C}_{st1}^{EE} & 0 & 0 & 0 \\ 0 & 0 & 0 & \mathbf{C}_{st2}^{ZZ} & \mathbf{C}_{st2}^{ZN} & \mathbf{C}_{st2}^{ZE} \\ 0 & 0 & 0 & \mathbf{C}_{st2}^{NZ} & \mathbf{C}_{st2}^{NN} & \mathbf{C}_{st2}^{NE} \\ 0 & 0 & 0 & \mathbf{C}_{st2}^{EZ} & \mathbf{C}_{st2}^{EN} & \mathbf{C}_{st2}^{EE} \end{pmatrix} , \tag{6.3}$$

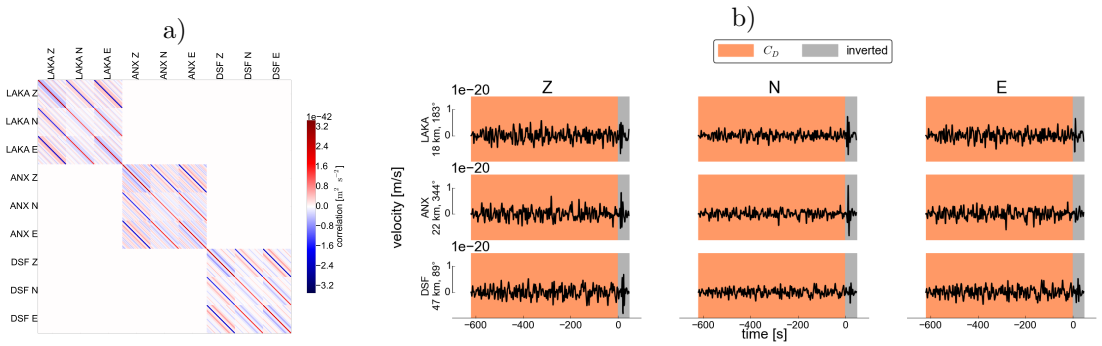

Figure 6.1: Example of data covariance matrix (panel a) and related seismograms (panel b). We generated synthetic data for three 3-component stations for a given seismic source and added planar wave white noise coming from azimuth 54° and inclination −21°, so all components are affected (panel b). The data covariance matrix $\mathbf{C}_D$ (panel a) is calculated from the before event noise (orange time window in panel b). The data covariance matrix consists of three large non-empty blocks corresponding to three stations, their 3×3 sub-blocks correspond to auto- and cross-covariance of the 3 components. We can see that some components are correlated (red color at the diagonal) and the others anticorrelated (blue color). The correlation between stations is assumed to be zero.

where blocks on the diagonal (e.g., C^{ZZ}_{st1}, C^{NN}_{st1}, etc.) are given by Eqs. (6.1 and 6.2), while at non-diagonal blocks (e.g., C^{EN}_{st1}, C^{EZ}_{st1}, etc.) are given by Eq. (6.1), except $C(\tau_k)$ is discrete cross-covariance, estimated by discrete cross-correlation, so that, for example,

$$C^{EZ}(\tau_k) \overset{\text{ergodicity}}{=} (x^E \star x^Z)[\tau_k] \overset{\text{def}}{=} \frac{1}{2N+1} \sum_{m=-N}^{N} x^E[\tau_m]\; x^Z[\tau_{m+k}] \;, \tag{6.4}$$

would be an estimate of cross covariance for East-West ($x^E(t_i)$) and vertical component ($x^Z(t_i)$) noise time series at a single station. The empty blocks are from the assumption that the seismic noise is not correlated between the seismic stations.

We illustrate a data covariance matrix on a simple example in Fig. 6.1.

6.1 Standardized data calculated using the covariance matrix

The real vs. synthetic waveform match is commonly plotted as it provides visual control of the difference between the reality and a model. For the most simple case of the inverse problem with diagonal data covariance matrix with constant data variance σ^2 ($\mathbf{C}_D = \sigma^2\mathbf{I}$), the solution of the inverse problem (eq. 3.1) is

$$\widetilde{\mathbf{m}} = \left(\mathbf{G}^T \left(\sigma^2\mathbf{I}\right)^{-1} \mathbf{G}\right)^{-1} \mathbf{G}^T \left(\sigma^2\mathbf{I}\right)^{-1} \boldsymbol{d}_{obs} = \left(\mathbf{G}^T\mathbf{G}\right)^{-1} \mathbf{G}^T \boldsymbol{d}_{obs} \;. \tag{6.5}$$

Then the real/synthetic waveform difference, which is plotted, is also minimized in the L^2-norm. For general $\mathbf{C}_D$ described in this chapter, interpreting such a

waveform match as a criterion of the fit quality is problematic, because the misfit value and the difference between the real and synthetic waveform is weighted by the data covariance matrix (Eq. 3.3). Consequently, a large difference between the observed and simulated waveforms may be caused by frequencies which are actually suppressed in the inversion by the effect of $\mathbf{C}_D$ and the stations with the largest amplitudes might not be the ones with the largest impact. In this section, we present a way how to visualize the waveform difference, which is directly related to the minimized misfit.

Since $\mathbf{C}_D$ is positive-definite matrix by its definition (we use biased estimate of the covariance function in Eqs. 6.1 and 6.3), we can use Cholesky decomposition [Cholesky, 1910; Hazewinkel, 2001].

$$\mathbf{C}_D^{-1} = \mathbf{L}\mathbf{L}^T \ . \tag{6.6}$$

Then we can rewrite the misfit definition (Eq. 3.3) in the following way:

$$\begin{aligned} \text{misfit}_i &= (\boldsymbol{d}_{obs} - \mathbf{G}\widetilde{\boldsymbol{m}}_i)^T \mathbf{L}\mathbf{L}^T (\boldsymbol{d}_{obs} - \mathbf{G}\widetilde{\boldsymbol{m}}_i) = \\ &= \left(\mathbf{L}^T\boldsymbol{d}_{obs} - \mathbf{L}^T\mathbf{G}\widetilde{\boldsymbol{m}}_i\right)^T \left(\mathbf{L}^T\boldsymbol{d}_{obs} - \mathbf{L}^T\mathbf{G}\widetilde{\boldsymbol{m}}_i\right) = \\ &= (\boldsymbol{d}'_{obs} - \boldsymbol{d}'_i)^T (\boldsymbol{d}'_{obs} - \boldsymbol{d}'_i) \ , \end{aligned} \tag{6.7}$$

where

$$\begin{aligned} \boldsymbol{d}'_{obs} &= \mathbf{L}^T\boldsymbol{d}_{obs} \\ \boldsymbol{d}' &= \mathbf{L}^T\mathbf{G}\widetilde{\boldsymbol{m}}_i \ . \end{aligned} \tag{6.8}$$

The difference between $\boldsymbol{d}'_{obs}$ and $\boldsymbol{d}'$ (called standardized residuals, according to Dettmer et al. [2014]) is minimized in the L^2-norm, so it can be plotted to visualize waveform agreement as used in inversion. The effect of the automated station weighting and frequency filtering, that are also included in the approach, (shown in Section 8.1) can be seen in $\boldsymbol{d}'_{obs}$ (standardized observed data) and $\boldsymbol{d}'$ (standardized synthetic data) also. As a drawback, the information at components of $\boldsymbol{d}'_{obs}$ (standardized data) may be mixed compared to components of $\boldsymbol{d}_{obs}$ (original data). This may happen if, e.g., the noise on horizontal components E and N is strongly correlated. Then the information about its correlation, contained in $\mathbf{C}_D$, helps in the inverse problem, but the $\mathbf{C}_D$ also causes tradeoff between components E and N of standardized waveforms. This tradeoff is intrinsically connected with removing the effect of the noise correlated between components.

6.2 Formulation of the inverse problem in the spectral domain

Initially, we intended to solve the inverse problem (described in Chapter 3) in spectral domain, because the records can be time-shifted with lower computational expenses there. Later, we decided to solve the problem in the time domain by a pre-calculated set of time-shifted data vectors $\boldsymbol{d}$, which are the same for all points of the space-time grid, where we search the hypocenter. We decided to

keep the formulation in spectral domain in the thesis, although it was not used finally, for the case it would be useful for someone.

The general equation of the inverse problem (eq. 3.1) is valid also in the spectral domain, but we have to define what is contained in our new data vector $\hat{\mathbf{d}}$ and forward problem matrix $\hat{\mathbf{G}}$, and find out what is contained in covariance matrix in spectral domain $\hat{\mathbf{C}}_D$.

The data vector and the forward-problem matrix are composed of spectra of the single components ordered in the following way (here an example for two stations with components Z, N, E)

$$\hat{\mathbf{d}} = \begin{pmatrix} \hat{D}^Z_{st\,1} \\ \hat{D}^N_{st\,1} \\ \hat{D}^E_{st\,1} \\ \hat{D}^Z_{st\,2} \\ \hat{D}^N_{st\,2} \\ \hat{D}^E_{st\,2} \end{pmatrix} \quad ; \qquad \hat{\mathbf{G}} = \begin{pmatrix} \widehat{E1}^Z_{st\,1} & \widehat{E2}^Z_{st\,1} & \dots & \widehat{E6}^Z_{st\,1} \\ \widehat{E1}^N_{st\,1} & \widehat{E2}^N_{st\,1} & \dots & \widehat{E6}^N_{st\,1} \\ \widehat{E1}^E_{st\,1} & \widehat{E2}^E_{st\,1} & \dots & \widehat{E6}^E_{st\,1} \\ \widehat{E1}^Z_{st\,2} & \widehat{E2}^Z_{st\,2} & \dots & \widehat{E6}^Z_{st\,2} \\ \widehat{E1}^N_{st\,2} & \widehat{E2}^N_{st\,2} & \dots & \widehat{E6}^N_{st\,2} \\ \widehat{E1}^E_{st\,2} & \widehat{E2}^E_{st\,2} & \dots & \widehat{E6}^E_{st\,2} \end{pmatrix} , \tag{6.9}$$

where $\hat{D}^X_{st\,m}$ is the spectrum of component X of station m, obtained from observed seismogram $D^X_{st\,m}$ by Discrete Fourier Transform (DFT), and $\widehat{Ei}^X_{st\,m}$ is the spectrum of elementary seismogram of elementary moment tensor i and the specified station m and component X, obtained as DFT of $Ei^X_{st\,m}$. The ordering is exactly the same as ordering used finally in formulation in the time domain, for more details see further eq. 7.21.

We introduce a matrix of Discrete Fourier Transform (DFT matrix) [Brokešová, 2008]

$$\begin{aligned} \mathbf{F}_1 &= \left(\frac{\omega^{jk}}{\sqrt{N}} \right)_{j,k=0\dots N-1} = \\ &= \frac{1}{\sqrt{N}} \begin{pmatrix} 1 & 1 & 1 & 1 & \cdots & 1 \\ 1 & \omega & \omega^2 & \omega^3 & \cdots & \omega^{N-1} \\ 1 & \omega^2 & \omega^4 & \omega^6 & \cdots & \omega^{2(N-1)} \\ 1 & \omega^3 & \omega^6 & \omega^9 & \cdots & \omega^{3(N-1)} \\ \vdots & \vdots & \vdots & \vdots & \ddots & \vdots \\ 1 & \omega^{N-1} & \omega^{2(N-1)} & \omega^{3(N-1)} & \cdots & \omega^{(N-1)(N-1)} \end{pmatrix} , \end{aligned} \tag{6.10}$$

where $\omega = e^{-\frac{2\pi i}{N}}$ and N is the length of the data vector $\hat{D}$.

The DFT matrix transforms one time series to frequency domain. If we have data vector or forward problem matrix composed of more time series, which should be transformed independently, the DFT matrix will be composed of blocks, which are given by eq. 6.10

$$\mathbf{F} = \begin{pmatrix} \mathbf{F}_1 & 0 & \cdots & 0 \\ 0 & \mathbf{F}_1 & \cdots & 0 \\ \vdots & \vdots & \ddots & \vdots \\ 0 & 0 & \cdots & \mathbf{F}_1 \end{pmatrix} \tag{6.11}$$

.

Then we can write Fourier transform of the data vector and the forward problem matrix as

$$\hat{\mathbf{d}} = \mathbf{F}\boldsymbol{d}\,; \qquad \hat{\mathbf{G}} = \mathbf{F}\mathbf{G}\,. \tag{6.12}$$

Now we rewrite general equation of the inverse problem (eq. 3.1) using inverse Fourier transform $\mathbf{G} = \mathbf{F}^{-1}\hat{\mathbf{G}}$ and $\boldsymbol{d} = \mathbf{F}^{-1}\hat{\mathbf{d}}$

$$\widetilde{\mathbf{m}} = \left(\left(\mathbf{F}^{-1}\hat{\mathbf{G}}\right)^T \mathbf{C}_D^{-1}\mathbf{F}^{-1}\hat{\mathbf{G}}\right)^{-1} \left(\mathbf{F}^{-1}\hat{\mathbf{G}}\right)^T \mathbf{C}_D^{-1}\mathbf{F}^{-1}\hat{\mathbf{d}}_{obs}\,. \tag{6.13}$$

Using $(\mathbf{AB})^T = \mathbf{B}^T\mathbf{A}^T$ we get

$$\widetilde{\mathbf{m}} = \left(\hat{\mathbf{G}}^T \underbrace{\left(\mathbf{F}^{-1}\right)^T \mathbf{C}_D^{-1}\mathbf{F}^{-1}}\, \hat{\mathbf{G}}\right)^{-1} \hat{\mathbf{G}}^T \underbrace{\left(\mathbf{F}^{-1}\right)^T \mathbf{C}_D^{-1}\mathbf{F}^{-1}}\, \hat{\mathbf{d}}_{obs}\,. \tag{6.14}$$

Now we do some algebra with parts of the last equation highlighted by brace

$$\left(\mathbf{F}^{-1}\right)^T \mathbf{C}_D^{-1}\mathbf{F}^{-1} = \left(\mathbf{F}^T\right)^{-1} \left(\mathbf{F}\mathbf{C}_D\right)^{-1} = \left(\mathbf{F}\mathbf{C}_D\mathbf{F}^T\right)^{-1}\,, \tag{6.15}$$

where we have used $(\mathbf{AB})^{-1} = \mathbf{B}^{-1}\mathbf{A}^{-1}$ and $\left(\mathbf{A}^T\right)^{-1} = \left(\mathbf{A}^{-1}\right)^T$.

If we denote two-dimensional (2-D) Fourier transform of $\mathbf{C}_D$ as $\hat{\mathbf{C}}_D = \mathbf{F}\mathbf{C}_D\mathbf{F}^T$, we can write formula for the inverse problem in the exactly same form as in the time domain

$$\widetilde{\mathbf{m}} = \left(\hat{\mathbf{G}}^T\hat{\mathbf{C}}_D^{-1}\hat{\mathbf{G}}\right)^{-1} \hat{\mathbf{G}}^T\hat{\mathbf{C}}_D^{-1}\hat{\mathbf{d}}_{obs}\,. \tag{6.16}$$

We can easily show, that $\hat{\mathbf{C}}_D$ is a 2-D Fourier transform of matrix $\mathbf{C}_D$. Using $(\mathbf{AB})_{jk} = \sum_{n=0}^{N} \mathbf{A}_{jn}\mathbf{B}_{nk}$ and by substitution for DFT matrix components (here for one component or time series) from eq. 6.10 we get

$$\begin{aligned}
(\mathbf{F}_1\mathbf{C})_{jk} &= \sum_{n=0}^{N-1} \frac{\omega^{jn}}{\sqrt{N}}\mathbf{C}_{nk} \\
(\mathbf{F}_1\mathbf{C}\mathbf{F}_1^T)_{jk} &= \sum_{n=0}^{N-1}\left(\sum_{m=0}^{N-1}\frac{\omega^{jm}}{\sqrt{N}}\mathbf{C}_{mn}\right)\frac{\omega^{nk}}{\sqrt{N}} = \\
&= \sum_{n=0}^{N-1}\sum_{m=0}^{N-1}\mathbf{C}_{mn}\frac{\omega^{jm}}{\sqrt{N}}\frac{\omega^{nk}}{\sqrt{N}} \\
&= \frac{1}{N}\sum_{n=0}^{N-1}\sum_{m=0}^{N-1}\mathbf{C}_{mn}e^{-2\pi i\frac{(jm+nk)}{N}}
\end{aligned} \tag{6.17}$$

The previous formula is derived for a single component. Now we show how it can be generalized for more components and more stations with high computational efficiency. To obtain the covariance matrix for more components, the 2-D Fourier transform is done block-by-block. Here we show an example for two

stations $st1$ and $st2$, each of them with two components N and E. The matrix for more stations / components can be obtained in analogous way.

$$\begin{pmatrix} \mathbf{F} & 0 & 0 & 0 \\ 0 & \mathbf{F} & 0 & 0 \\ 0 & 0 & \mathbf{F} & 0 \\ 0 & 0 & 0 & \mathbf{F} \end{pmatrix} \begin{pmatrix} \mathbf{C}_{st1}^{NN} & \mathbf{C}_{st1}^{NE} & 0 & 0 \\ \mathbf{C}_{st1}^{EN} & \mathbf{C}_{st1}^{EE} & 0 & 0 \\ 0 & 0 & \mathbf{C}_{st2}^{NN} & \mathbf{C}_{st2}^{NE} \\ 0 & 0 & \mathbf{C}_{st2}^{EN} & \mathbf{C}_{st2}^{EE} \end{pmatrix} \begin{pmatrix} \mathbf{F} & 0 & 0 & 0 \\ 0 & \mathbf{F} & 0 & 0 \\ 0 & 0 & \mathbf{F} & 0 \\ 0 & 0 & 0 & \mathbf{F} \end{pmatrix} =$$

$$= \begin{pmatrix} \mathbf{F}\mathbf{C}_{st1}^{NN} & \mathbf{F}\mathbf{C}_{st1}^{NE} & 0 & 0 \\ \mathbf{F}\mathbf{C}_{st1}^{EN} & \mathbf{F}\mathbf{C}_{st1}^{EE} & 0 & 0 \\ 0 & 0 & \mathbf{F}\mathbf{C}_{st2}^{NN} & \mathbf{F}\mathbf{C}_{st2}^{NE} \\ 0 & 0 & \mathbf{F}\mathbf{C}_{st2}^{EN} & \mathbf{F}\mathbf{C}_{st2}^{EE} \end{pmatrix} \begin{pmatrix} \mathbf{F} & 0 & 0 & 0 \\ 0 & \mathbf{F} & 0 & 0 \\ 0 & 0 & \mathbf{F} & 0 \\ 0 & 0 & 0 & \mathbf{F} \end{pmatrix} = \tag{6.18}$$

$$= \begin{pmatrix} \mathbf{F}\mathbf{C}_{st1}^{NN}\mathbf{F} & \mathbf{F}\mathbf{C}_{st1}^{NE}\mathbf{F} & 0 & 0 \\ \mathbf{F}\mathbf{C}_{st1}^{EN}\mathbf{F} & \mathbf{F}\mathbf{C}_{st1}^{EE}\mathbf{F} & 0 & 0 \\ 0 & 0 & \mathbf{F}\mathbf{C}_{st2}^{NN}\mathbf{F} & \mathbf{F}\mathbf{C}_{st2}^{NE}\mathbf{F} \\ 0 & 0 & \mathbf{F}\mathbf{C}_{st2}^{EN}\mathbf{F} & \mathbf{F}\mathbf{C}_{st2}^{EE}\mathbf{F} \end{pmatrix},$$

The previous formulas show, how a linear inverse problem in the Bayesian formulation can be solved in the frequency domain and how the vectors and matrices can be transformed. The inversion itself could have very similar computational expenses both in time and frequency domain, but the frequency domain can be slightly more effective if we have to do time-shifts of the data vector. Finally, this formulation was not used in the developed method, but it is valid generally for various inverse problems, so we decided to keep it in the thesis.

7. Developed method and its technical aspects

Lead-in text of this chapter is based on Section 6 of Vackář et al. [2017].

The method described in the previous Chapters 3 and 4, together with a few other procedures for optimal data selection and some plotting routines, is programmed as a software package ISOLA-ObsPy, which can be used for fully automated moment tensor inversion, including near-real-time data flows, as well as large data sets of previously recorded events.

The package includes automated data retrieval (saved in any file format supported by ObsPy [Krischer et al., 2015] or accessible via ArcLink [*SeisComP3 documentation*]), removal of components with various instrumental disturbances, setting frequency ranges for each station individually according to its distance and event magnitude, and full-waveform inversion in space-time grid around hypocenter. The size of the space-time grid is automatically chosen according to the location uncertainty and magnitude. Time sampling is 100-times higher then the high limit of the inverted frequency band. Spatial sampling can be adjusted by user by entering horizontal and vertical step directly and/or by entering maximal number of grid points.

Grid search over time and space is effectively combined with analytical (least-squares) MT inversion in a Bayesian framework. This way not only the best solution is found, but also the full posterior probability density function of the CMT is inferred. The marginal probability density function for any CMT parameter can be plotted. Data covariance matrix calculated from the before-event noise yields an automated weighting of the stations according to their noise levels and also serves as an automated frequency filter suppressing noisy frequencies. To speed up the inversion, the time demanding tasks such as the Green's function calculations and the spatial grid search are parallelized. The software package is programmed as versatile as possible in order to be applicable in various networks ranging from local to regional.

The code shares some similarities with the broadly used ISOLA software [Sokos and Zahradník, 2013] in terms of the inversion methods and input/output file structures, but most codes have been re-written from the scratch for maximum computational efficiency (combing Fortran and Python, using ObsPy, NumPy, and MatPlotLib). In contrast to ISOLA, whose advantage is in a friendly manual processing of individual events using Matlab GUI, the new codes are intended rather for a massive automated application on large sets of earthquakes from a database, and/or for near real-time applications.

Although the process is fully automated, the inversion can be visually inspected later. For this reason, many figures are automatically plotted.

The ISOLA-ObsPy software package is available under GNU/GPL licence[1] and can be downloaded from `http://geo.mff.cuni.cz/~vackar/isola-obspy/`,

[1]The GNU General Public License (GNU GPL) is a widely used free software license, which guarantees end users the freedom to run, study, share and modify the software. Available at `https://gnu.org/licenses/gpl.html`

where there is also full documentation.

In the following sections we describe all the process from an earthquake alert to visualized result including all technical details.

7.1 Technical solution

In this section, we add some technical details related to the developed method extending the description in the lead-in of this chapter.

For programming the automated CMT inversion, we have chosen Python because it is powerful and high-level programming language, with a wide range of standard libraries, and it is available for many operating systems. During the development, we appreciated high code readability and syntax which enable to express concepts in a brief way. We wrote the package using object-oriented programming[2]. The core of the package is a class[3] `ISOLA`. This class contains input data (like seismograms and initial location), calculated intermediate products (like the data covariance matrix), and results (e.g. most probable CMT and its uncertainty), as well as methods performing all steps of the calculation. This concept enables an easy implementation of the method to a larger product, like a program for real time data processing or analysis of a large dataset of historical earthquakes. In such application (one is described in Section 8.2), each analyzed earthquake is a separate instance[4] of class `ISOLA`, having its own data and results.

In the development, we benefit from many standard libraries of Python and seismological toolbox `ObsPy`. We list the used libraries in Table 7.1.

Table 7.1: Libraries used in class `ISOLA`.

library	**used for**
`math`	basic mathematical operations
`numpy`	linear algebra matrices and operations with them
`subprocess`	executing code for Green's function calculation
`shutil`	file manipulation (copying etc.)
`multiprocessing`	running computationally expensive calculation in parallel
`re`	regular expressions (parsing ASCII data files)
`fractions`	calculating least common multiple
`warnings`	control of warning messages
`pyproj.Geod`	transformation of geodetic coordinates
`scipy`	interpolation, reading Fortran binary files
`os.path`	operations with file path
`psycopg2`	reading network info from SeisComp (PostgreSQL) database
`matplotlib`	MATLAB-like plotting
`obspy`	seismological toolbox

The calculation of Green's functions is out of scope of this thesis. They are computed by code `axitra` [Bouchon, 1981; Coutant, 1989], which is called from our code.

[2]concept of programming, which uses "objects", which may contain several data fields (often called 'attributes') and code in the form of procedures (called 'methods')

[3]program-code-template for creating objects, providing initial values for member variables and implementations of the methods

[4]a concrete realization of the class

The most computationally demanding parts of the calculation are calculation of the Green's function and searching the solution of the inverse problem on space-time grid. These two parts are parallelized using Python module `multiprocessing`. This module runs separate tasks as subprocesses and allows the programmer to fully leverage multiple processors on a given machine.

7.2 Input data

The location is one of the main input data for our code. Namely we need the following: epicenter coordinates, origin time, hypocenter depth (all including its uncertainty), and magnitude. The location can be just approximate, because the centroid position and time is then grid-searched around the given position. The location uncertainty, which is used later to calculate the space-time grid extend, must be set also. It is upon the user to consider whether the location uncertainty in a catalog or calculated by a location code is realistic; especially the depth uncertainty is often underestimated. The magnitude can be also an estimate, e. g. M_L; it serves for estimation of maximal possible hypocenter-to-centroid distance. All previously mentioned values can be read from file in ISOLA-compatible format (by function `read_event_info`) or can be set directly (by function `set_event_info`).

Beside location, some other parameters must be set, which control technical aspects of the calculation and add some information about location uncertainty. These parameters are listed in Table 7.2. They can be set when initializing class `ISOLA`.

A 1-D crustal velocity model is needed for calculation of the Green's functions. It should be in format of the code `axitra`, which is used for calculation of elementary seismograms. It is read by function `read_crust`.

Technically, the waveforms and metadata related to the stations are also input data. They can be provided directly by user as files, but do not have to be, the code can download the waveforms directly from ArcLink server. We describe the ways of obtaining the waveforms in the following chapter.

7.3 Waveforms and metadata downloading

We need three things related to the waveforms: positions of seismic stations, instrument parameters, and waveforms themselves. There are two ways of obtaining configuration of seismic network, i.e. coordinates of the seismic stations. The stations, together with their coordinates, may be listed in a text file (format compatible with ISOLA, read by function `read_network_coordinates`) or all required information may be obtained from SeisComP3 database (by function `read_network_info_DB`). Technically, it means that the code connects directly to PostgreSQL database and queries stations, which have been in operation during the event and lies within a circle around epicenter. The radius of the circle r_{max} is the following empirical function of magnitude

$$r_{max} = 1000 \cdot 2^{2M_W} \text{ [m]} , \tag{7.1}$$

Table 7.2: Parameters of class `ISOLA`.

parameter	**default value**	**description**
`location_unc`	0	Horizontal uncertainty of the location in meters
`depth_unc`	0	Vertical (depth) uncertainty of the location in meters
`time_unc`	0	Uncertainty of the origin time in seconds
`deviatoric`	False	If False: invert full moment tensor (6 components); if True invert deviatoric part of the moment tensor (5 components)
`step_x`	500	Preferred horizontal grid spacing in meter (in m)
`step_z`	500	Preferred vertical grid spacing in meter (in m)
`max_points`	100	Maximal (approximate) number of the grid points
`threads`	2	Number of threads for parallelization
`circle_shape`	True	If True, the shape of the grid is cylinder, otherwise it is rectangular box
`use_precalculated_Green`	False	Use Green's functions calculated in the previous run
`rupture_velocity`	1000	rupture propagation velocity in m/s, used for estimating the difference between the origin time and the centroid time
`decompose`	True	Performs decomposition of the found moment tensor in each grid point
`s_velocity`	3000	Characteristic S-wave velocity used for calculating number of wave lengths between the source and stations (in m/s)
`logfile`	'output/log.txt'	Path to the logfile

which we obtain by trialing different functions during testing the code within Swiss Seismic Network. In addition, we exclude stations too close to the epicenter. From our experience, such stations make the inversion unstable and it is hardly possible to fit their waveforms. It is probably because the point source approximation is inappropriate in case of them, and their waveforms are dominated by effects of finite source. The minimal distance r_{min} is set up to the estimated rupture length d_{rup} multiplied by factor 2.

$$r_{min} = 2 \cdot d_{rup} = 2 \cdot \sqrt{111 \cdot 10^M} \text{ [m]} , \tag{7.2}$$

where M is the estimated magnitude of the event, and the formula for estimated rupture length is derived from Somerville et al. [1999, formula $M = \log A + 3.95$, area A in square km]. Now we have a set of stations in an annulus around epicenter.

We are mostly interested in broad-band stations, so during automated station selection (from the SeisComP3 database) we skipped all stations whose channel codes are not labeled "HH*" or "BH*" [Halbert, 2012]. The maximal number of inverted stations is set by default to 21; if there are more of them loaded, we take just the closest ones.

Once we have defined stations of interest, their waveform must be obtained. The first option is reading data from files. We can add data from each station sep-

arately (functions `add_NEZ` and `add_SAC`), or all together (function `load_files`), if the files are in the same directory and the filenames keep a standard. Together with data, we usually load response files, which describe instrument response of the measuring device. For waveforms, the supported formats are 4-column (time and north, east, and vertical components) text file in ISOLA format and all formats supported by ObsPy. For metadata, supported are ISOLA poles&zeros files and station-XML response files.

The second option is reading data via ArcLink (function `load_streams_ArcLink`). The ArcLink protocol is a part of SeisComP3 package and enables obtaining seismic data from specified stations and defined time window by querying ArcLink data server. It allows easy processing of large datasets and near real-time applications. Together with reading network setting from SeisComP3 database, it makes possible to analyze a set of earthquakes just with a list of events, with no need to care about data preparation. During downloading from ArcLink server, the stations where data are not available or some component is missing are removed from further processing. In the current version of the code, entire station is removed in case of missing component. For technical reasons, removed are also sensors with components with unknown orientation (typically sensors in boreholes). Obtaining network configuration from SeisComP3 database as well as downloading data from ArcLink server was tested (and successfully used) against ETH Zurich SeisComP3 and ArcLink server.

7.4 Detection of disturbances

From a variety of possible disturbances, which may occur in seismic records, we believe that so called fling step (also mouse or ping) is the most dangerous one. Technically, it corresponds to step in acceleration on seismograph input, which results in the characteristic shape on the instrument output. Due to its long-period character, it can be easily overlooked in band-pass filtered records. If the disturbed record is kept in inversion, it often results in misleading result. And last but not least, such disturbances are quite common. Inspired by Zahradník and Plešinger [2005, 2010], we have studied these disturbances in paper Vackář et al. [2015] (included in this thesis as Chapter 5).

In the proposed method, we use own code for detection of disturbances. The code was originally described in Vackář et al. [ibid.], the current version is available at `http://geo.mff.cuni.cz/~vackar/mouse/`. The code detect disturbances which correspond to a step in input acceleration of the instrument, another type of disturbance which correspond to a step in input velocity is not detected. In the `ISOLA-ObsPy` code, it is called from function `detect_mouse`, which also evaluates the result. Components, where the disturbance is detected, are skipped from the inversion, but they are still kept in memory and are plotted in the waveform fit figure. In the detection, a disturbance is modeled for given instrument and fitted into observed record, so an amplitude of the best-fitting disturbance is calculated as well as the fit value (variance reduction) between the modeled disturbance and the record. The record is considered as disturbed if the amplitude and fit value exceed one of the empirically established threshold of values (obtained by testing on dozens of disturbed records and minimizing number

of false detections) listed below:

$$\begin{aligned} amp > 500e-9 \wedge fit > 0.6 \\ amp > 100e-9 \wedge fit > 0.8 \\ amp > 70e-9 \wedge fit > 0.9 \\ amp > 5e-9 \wedge fit > 0.94 \\ fit > 0.985 \end{aligned} \tag{7.3}$$

7.5 Instrument response deconvolution

Instrument characteristics, namely poles, zeros, and gain, are typically obtained together with data, when they are read from files or ArcLink server. Observed data are then corrected using ObsPy function `Trace.simulate`. Before correction, the mean value is subtracted and highpass filter with frequency 0.01 Hz is applied on observed data. It is assumed, that the inversion in the next steps will not be carried out at frequencies lower than 0.01 Hz. All this is done within function `correct_data`.

7.6 Choosing optimal sampling and other parameters

In this chapter, we have to set up some variables, e.g. limits of inverted frequency band, various time window lengths, etc. For some of them, we have an objective criterion, the others have to be chosen more or less ad hoc. Their default values have been selected after testing different values as the best working option, but in some other applications, it might be useful to change them. Most of such variables can be changed by user simply as parameters of particular functions. The rest of them can be changed simply in the source code, which is open source.

7.6.1 Frequency ranges

Frequency band for the inversion is set by user (by setting parameters of function `set_frequencies`). The low frequency limit f_{min} should correspond to the lowest frequency which can be measured by used instrument, the high frequency limit f_{max} should reflect the highest frequencies which can be satisfactorily modeled in the used velocity model; for details, see below. This frequency range should also reflect spectrum of the source. Contrary to some other codes, e.g. ISOLA, the selected range does not need to take care of the noise spectrum (e.g. microseisms), because the noisy frequencies are automatically downweighted by the data covariance matrix.

The high frequency limit from this manually selected range is then automatically decreased at distant stations, where we assume that the high frequencies cannot be satisfactorily modeled. The number of wavelengths n at characteristic S-velocity v_S is used as an objective criterion for setting maximal frequency f_{max}^{sta} for a given station.

$$f_{max}^{sta} = \min(f_{max}, \frac{n\, v_S}{r}) \ , \tag{7.4}$$

where r_{sta} is the distance between the source and station. Parameters v_S and n are by default 3000 m/s and 5, respectively, or can be set by user.

7.6.2 Working sampling

The target working sampling is determined from the high-frequency limit (the same for all stations) as an 8-times higher frequency than maximal inverted frequency f_{max} to keep distance between bandpass high frequency limit and the Nyquist frequency of sub-sampling. Then we determine common sampling rate S_{comm} as the greatest common divisor (GCD) from sampling rates of single components s_1, $s_2 \ldots$ The decimation factor d, which is the quotient of these two numbers, is then rounded by the floor function to enables integer decimation factor. The used working sampling S_{used} is finally determined as a quotient of S_{comm} and d.

$$\begin{aligned} S_{comm} &= \mathrm{GCD}\,(s_1, s_2 \ldots) \\ d &= \lfloor \frac{S_{comm}}{8 f_{max}} \rfloor \\ S_{used} &= S_{comm}/d \end{aligned} \tag{7.5}$$

7.6.3 Time window for the inversion

For the waveform modeling, we need a time window, which includes all waveforms of the seismic event, but it should not be too long, because the computational expenses groves with its length. For simplicity, we use the same time window for all stations. The start time is fixed to 20 second before the origin time in the current version of the code

$$t_{min} = t_{orig} - 20\,s\ . \tag{7.6}$$

The end time is given by formula

$$t_{max} = t_{orig} + l_{max}/v_{surf}\ , \tag{7.7}$$

where l_{max} is the distance from the hypocenter (the deepest tested depth below epicenter) to the most distant station and v_{surf} is a reference velocity of the slowest surface wave group (1000 m/s by default). The time window, as well as the number of samples, is calculated by function `set_time_window`.

7.6.4 Number of samples

The number of samples both for the inversion as well as for the calculation of the Green's functions has to be chosen. The number of samples for the inversion (npts_slice) is calculated by the following formula

$$\mathrm{npts\_slice} = \|t_{max} \cdot S_{used}\|\ , \tag{7.8}$$

where the symbols $\|\ \|$ stands for rounding to integer value. The number of samples for the calculation of the Green's function (npts_elemse) is calculated by the following formula

$$\mathrm{npts\_elemse} = \mathrm{next\_power\_of\_2}\left\{\|\,(t_{max} - t_{min}) \cdot S_{used}\|\right\}\ , \tag{7.9}$$

where we round up to the next power of 2 because the code used for calculation of Green's function, `axitra`, require such lengths of records due to implementation of Fast Fourier Transformation.

The number of samples, as well as the time window, is calculated by function `set_time_window`.

7.7 Space-time grid

The moment tensor inverse problem is linear in moment tensor components, but non-linear in centroid position and time. We perform grid search over these 4 parameters (3 space coordinates and time) and we calculate analytically the other parameters in each grid point. In this section, we describe how is the space-time grid chosen.

The space grid is arranged by function `set_grid`. The shape of the grid is a cylinder or rectangular box around the given hypocenter. The cylinder is the default option, it can be changed by parameter `circle_shape` of class `ISOLA` (see Table 7.2). The radius r_{grid} is the sum of location uncertainty σ_{loc} (parameter of class `ISOLA`) and estimated rupture length d_{rup}

$$r_{grid} = \sigma_{loc} + d_{rup} \ . \tag{7.10}$$

The vertical extent of the grid is a function of the given location depth z_{hyp}, depth uncertainty σ_{depth}, user-given minimal depth z_{limit} (parameter of function `set_grid`, default value 1000 m), and estimated rupture length d_{rup}

$$\begin{aligned} z_{min} &= \max(z_{limit}, z_{hyp} - \sigma_{depth} - d_{rup}) \\ z_{max} &= z_{hyp} + \sigma_{depth} + d_{rup} \ , \end{aligned} \tag{7.11}$$

where we estimate the rupture length d_{rup} according to

$$d_{rup} = \sqrt{111 \cdot 10^M} \quad [\mathrm{m}] \ , \tag{7.12}$$

where M is the estimated magnitude of the event; and the result is in meters. The grid sampling is controlled by parameters `step_x`, `step_z`, and `max_points` of class `ISOLA`. First, number of grid points in case of using parameters `step_x` for horizontal spacing and `step_z` for vertical spacing is calculated. If it exceeds `max_points`, both horizontal and vertical spacing is increased by such factor, that the number of grid points correspond to `max_points`.

The time grid is set up by function `set_time_grid`. The first and the last tested time, t_{min} and t_{max}, respectively, are given by

$$\begin{aligned} t_{min} &= t_{hyp} - \sigma_t - d_{rup}/v_{rup} \ [\mathrm{s}] \\ t_{max} &= t_{hyp} + \sigma_t + d_{rup}/v_{rup} \ [\mathrm{s}] \ , \end{aligned} \tag{7.13}$$

where v_{rup} stands for approximate rupture velocity (parameter of class `ISOLA`). The grid step in time Δ_t is fixed to one percent of minimal inverted period

$$\Delta_t = 0.01/f_{max} \ . \tag{7.14}$$

Finally, the minimal and maximal tested time and the time step are rounded to the greatest common divisor of station sampling S_{comm}, thus the shifting of records do not require any interpolation.

Table 7.3: Parameters of code `AXITRA`. Symbol r_{max} denotes epicentral distance to the most distant station, its formula means 20-times the distance, rounded to kilometers, and at least 2000 km.

parameter	default value	description
`nc`	99	number of crust model layers (ignored)
`nfreq`	$\|\text{npts\_elemse}/2\| + 1$	number of evaluated frequencies
`tl`	$\text{npts\_elemse}/S_{used}$	time-window length in seconds
`aw`	0.5	artificial attenuation in DWN method
`nr`	$n_{stations}$	number of receivers
`ns`	1	number of sources
`xl`	$\max(\lceil r_{max} \rceil, 100e3) \cdot 20$	space periodicity in meters
`ikmax`	100000	max. number of the summed terms in DWN
`uconv`	0.1E-06	convergence criterion for DWN method
`fref`	1.	

7.8 Green's function and elementary seismograms

Calculation of the Green's function is one of the key parts of the moment tensor inverse problem and in a typical calculation it is the most computationally demanding part.

The Green's functions are computed by code `axitra` [Bouchon, 1981; Coutant, 1989]. This code is internally called from function `calculate_Green` with configuration parameters listed in Table 7.3. Time variation of the moment rate is delta function.

The output of the code is in a form of 6 elementary seismograms in a basis, which is defined further in Section 7.10.

7.9 Data filtering and resampling

For the inverse problem calculation, the observed seismograms must be comparable to the synthetic elementary seismograms. Specifically, they have to have the same sampling rate, length, and if the firsts are filtered, the seconds must be filtered in the exactly same way and vice versa. For the inversion described in Chapter 3, we need not only a time window containing the earthquake, but also another time window for the noise analysis.

Technically, all this is provided by function `trim_filter_data` and function `decimate_shift`, using also functions `prefilter_data` and `my_filter`, which are called internally from the previous two.

First, parts of seismograms for the noise analysis are copied from the original ones. If their length and start time is not chosen manually, they are 4-times longer than the inverted time window and their end time is the same as start time of the inverted time window. If a component of seismogram is not long enough (e.g. because of a gap in the data), the noise time window is shorter for the component, but if the length is shorter than 110 %, the noise is not analyzed at all and just "standard" inversion without noise covariance matrix is allowed. Than the noise record is sampled down to sampling two-times higher than inverted sampling rate and filtered by the same filter as the data (described in the following paragraph), but with two-times wider both low- and high-frequency limits of the filter. This

factor two is to avoid considering limits of the filter as low-noise part of spectrum in the noise covariance matrix.

Second, we focus on the part of record, which contains the earthquake. It is necessary to make it comparable to elementary seismograms, which are computed just up to a frequency specified in Section 7.8. To reach that, we transform the record to the spectral domain by Fast Fourier Transformation (FFT), drop the frequencies above that limit, and transform it back to the time domain using inverse FFT. We did a synthetic test proving that this operation is necessary for 100% fit in cases when the elementary and synthetic 'observed' seismograms are calculated with different high-frequency limits.

The trial time shifts are set before (see Section 7.7). For every time shift, the inverted time window is copied from the record prepared as described in the previous paragraph. Then, the record is sampled down to the sampling frequency of the Green's functions. No anti-alias filter is applied, because everything above Nyquist frequency is removed before in the spectral domain. The downsampling after trimming record is necessary because the time shifts are (much) smaller then the sampling rate. Now, we have a set of data vectors for the inversion procedure, where each element of the set corresponds to one of the trial time shifts.

7.10 Inverse problem

The mathematical formulation of the inverse problem is described in Chapters 3 and 6. Here we add just a few details. First we define the used basis of elementary moment tensors and seismograms, then we set up the ordering of the matrices and vectors, and last we describe a few algebraic 'tricks' to increase the computational efficiency.

7.10.1 Elementary moment tensors

Moment tensor (MT) inverse problem is linear in MT components. It has 9 components, but only 6 of them is independent (assuming conservation of angular momentum).

We can choose a basis of 6 elementary MTs $\mathbf{M}^i$ and solve the inverse problem as looking for 6 unknown coefficients a_i. The MT is then

$$\mathbf{M}_{pq} = \sum_{i=1}^{6} a_i \mathbf{M}^i_{pq} \ . \tag{7.15}$$

We use the following basis, defined in coordinate system NEZ (axes to North, East, and down)

$$\begin{aligned} \mathbf{M}^1 &= \begin{pmatrix} 0 & 1 & 0 \\ 1 & 0 & 0 \\ 0 & 0 & 0 \end{pmatrix} \qquad \mathbf{M}^2 = \begin{pmatrix} 0 & 0 & 1 \\ 0 & 0 & 0 \\ 1 & 0 & 0 \end{pmatrix} \qquad \mathbf{M}^3 = \begin{pmatrix} 0 & 0 & 0 \\ 0 & 0 & -1 \\ 0 & -1 & 0 \end{pmatrix} \\ \mathbf{M}^4 &= \begin{pmatrix} -1 & 0 & 0 \\ 0 & 0 & 0 \\ 0 & 0 & 1 \end{pmatrix} \qquad \mathbf{M}^5 = \begin{pmatrix} 0 & 0 & 0 \\ 0 & -1 & 0 \\ 0 & 0 & 1 \end{pmatrix} \qquad \mathbf{M}^6 = \begin{pmatrix} 1 & 0 & 0 \\ 0 & 1 & 0 \\ 0 & 0 & 1 \end{pmatrix} \ . \end{aligned} \tag{7.16}$$

The elementary MTs $\mathbf{M}^1$–$\mathbf{M}^5$ represent five double-couple (DC) focal mechanisms, whereas $\mathbf{M}^6$ is a purely isotropic (ISO) source. The coefficients a in Equation 7.15 are related to $\mathbf{M}$ as

$$\mathbf{M} = \begin{pmatrix} -a_4 + a_6 & a_1 & a_2 \\ a_1 & -a_5 + a_6 & -a_3 \\ a_2 & -a_3 & a_4 + a_5 + a_6 \end{pmatrix} . \tag{7.17}$$

The elementary seismograms calculated using code `axitra` [Bouchon, 1981; Coutant, 1989] are computed in the same basis. The same basis is also used in the code ISOLA [Křížová et al., 2013].

The synthetic seismogram for a given MT is then

$$u_X = \sum_{i=1}^{6} a_i E_X^i \ , \tag{7.18}$$

where u_X is a component of synthetic seismogram in direction X and E^i is an elementary seismogram for an elementary moment tensor M^i.

The scalar seismic moment used in this thesis is defined by Silver and Jordan [1982] as

$$M_0 = \sqrt{\frac{\sum_{p=1}^{3} \sum_{q=1}^{3} \left(\mathbf{M}_{pq}\right)^2}{2}} \ . \tag{7.19}$$

7.10.2 Matrix ordering

Before we start solving the inverse problem using formulas presented above, we have to define the ordering of elements of data vectors and forward problem matrices. The ordering is not only formal thing, but it also makes the data covariance matrix block-diagonal, and allow us to decrease computational expenses of the inversion using the inversion of block-diagonal matrix.

First we define a data block of a component of a station, from which will be the following vectors and matrices built. The block of data and elementary seismogram, respectively, is

$$D_{st\,m}^X = \begin{pmatrix} d_1 \\ d_2 \\ \vdots \\ d_n \end{pmatrix} \ ; \qquad Ei_{st\,m}^X = \begin{pmatrix} ei_1 \\ ei_2 \\ \vdots \\ ei_n \end{pmatrix} \ , \tag{7.20}$$

where d and e are samples of observed and elementary seismograms, respectively, and X stands for component (Z, N, E), m indexes stations (ordered by increasing epicentral distance), n is number of time samples, and Ei stands for one of six elementary seismogram, which will be denoted $E1$, $E2$ ... $E6$. So the block is a vector whose length is the number of samples of the observed or elementary seismogram.

The data vector d and the forward-problem matrix G then have following

form (for case of two stations)

$$\boldsymbol{d} = \begin{pmatrix} D^Z_{st\,1} \\ D^N_{st\,1} \\ D^E_{st\,1} \\ D^Z_{st\,2} \\ D^N_{st\,2} \\ D^E_{st\,2} \end{pmatrix} \quad ; \qquad \mathbf{G} = \begin{pmatrix} E1^Z_{st\,1} & E2^Z_{st\,1} & \dots & E6^Z_{st\,1} \\ E1^N_{st\,1} & E2^N_{st\,1} & \dots & E6^N_{st\,1} \\ E1^E_{st\,1} & E2^E_{st\,1} & \dots & E6^E_{st\,1} \\ E1^Z_{st\,2} & E2^Z_{st\,2} & \dots & E6^Z_{st\,2} \\ E1^N_{st\,2} & E2^N_{st\,2} & \dots & E6^N_{st\,2} \\ E1^E_{st\,2} & E2^E_{st\,2} & \dots & E6^E_{st\,2} \end{pmatrix} \tag{7.21}$$

7.10.3 Computationally efficient solution of the problem

The core of the inversion is the eq. 3.1, which is evaluated in each point of space-time grid. Here we show, how the computational costs for solution of this equation can be decreased.

First, we invert matrix $\mathbf{C}_D$, which is the same for all grid points. It is a block diagonal matrix, with one block for one station. Such matrix can be inverted block-by-block. It can be easily proven

$$\begin{gathered} \mathbf{A}\mathbf{A}^{-1} = \mathbf{I} \\ \mathbf{B}\mathbf{B}^{-1} = \mathbf{I} \\ \begin{pmatrix} \mathbf{A} & 0 \\ 0 & \mathbf{B} \end{pmatrix} \begin{pmatrix} \mathbf{A}^{-1} & 0 \\ 0 & \mathbf{B}^{-1} \end{pmatrix} = \begin{pmatrix} \mathbf{I} & 0 \\ 0 & \mathbf{I} \end{pmatrix}. \end{gathered} \tag{7.22}$$

Than we have to evaluate eq. 3.1 in each grid point. Using pre-calculated $\mathbf{C}_D$, the only matrix inversion operation is performed on multiplication of matrices $\mathbf{G}^T\mathbf{C}_D^{-1}\mathbf{G}$, whose dimension is only 6×6

$$\overset{6\times1}{\left(\widetilde{\mathbf{m}}\right)} = \underbrace{\left(\overset{6\times n}{\left(\ \mathbf{G}^T\ \right)} \left(\overset{n\times n}{\left(\ \mathbf{C}_D^{-1}\ \right)} \right) \left(\overset{n\times 6}{\left(\mathbf{G}\right)} \right) \right)^{-1}}_{6\times6} \left(\overset{6\times n}{\left(\ \mathbf{G}^T\ \right)} \left(\overset{n\times n}{\left(\ \mathbf{C}_D^{-1}\ \right)} \right) \left(\overset{n\times 1}{\left(\boldsymbol{d}_{obs}\right)} \right) \right). \tag{7.23}$$

Moreover, the multiplication $\mathbf{G}^T\mathbf{C}_D^{-1}$ (which is twice in the formula) can be done block-by-block also

$$\begin{pmatrix} \mathbf{G}^T_{st1} & \mathbf{G}^T_{st2} & \mathbf{G}^T_{st3} \end{pmatrix} \begin{pmatrix} \mathbf{C}_{st1} & 0 & 0 \\ 0 & \mathbf{C}_{st2} & 0 \\ 0 & 0 & \mathbf{C}_{st3} \end{pmatrix} = \begin{pmatrix} \mathbf{G}^T_{st1}\mathbf{C}_{st1} & \mathbf{G}^T_{st2}\mathbf{C}_{st2} & \mathbf{G}^T_{st3}\mathbf{C}_{st3} \end{pmatrix} \tag{7.24}$$

So the computational expenses of the inversion grows linearly with number of stations. Compared to the non-optimized inversions of full matrices, this saves a few seconds or tens of seconds when inverting less than 10 station (the saved time is dependent on length of inverted record, their sampling, and other parameters). But this optimization start to be important when inverting more station, not only because the computation is faster, but also the memory requirements are lower.

7.11 Results plotting

The method is optimized for automated data processing, but a possibility for later visual inspection of algorithm is highly desirable in many applications. For that reason, the code has procedures for plotting various figures visualizing input data, result stability, uncertainty, waveform fit, as well as some intermediate products, like the figure of the covariance matrix.

Beside graphical output, the code provide also a plain text output by functions `print_solution`, which print out moment tensor itself and its position, and `print_fault_planes`, which provide moment tensor decomposition. Here we show an example output for $M_L = 4.2$ earthquake at Sargans, Switzerland on 2013-12-12 00:59:18.

```
Centroid location:
  Centroid time: 2013-12-12 00:59:18
  Lat    47.063    Lon     9.470    Depth    6.1 km
  (   617 m to the north and -1234 m to the east
                  with respect to epicenter)
  time:   0.60 s before origin time

  VR:     82 %
  CN:      3
  MT [  Mrr      Mtt      Mpp      Mrt      Mrp      Mtp  ]:
     [  0.86     0.12     0.49     0.34    -0.45    -2.33] * 1e+14

Scalar Moment: M0 = 3.01e+14 Nm (Mw = 3.6)
  DC component:   70 %,    CLVD component: -14 %,
                        ISOtropic component:  16 %
  Fault plane 1: strike =  91, dip =  78, slip-rake = 169
  Fault plane 2: strike = 183, dip =  79, slip-rake =  12
```

The moment tensor decomposition to DC, CLVD, and ISO part is calculated according to Vavryčuk [2015]. The condition number (CN) is square root of ratio of maximal and minimal eigenvalue of $\left(\mathbf{G}_i^T \mathbf{C}_D^{-1} \mathbf{G}_i\right)$ in eq. 3.1, which characterise stability of the inverse problem, i.e., how the output is sensitive to a small change of input values. Please note, that CN is related only to stability of the analytically solved part of the inverse problem, i.e., MT in the best grid point. Stability of the solution between the grid points can be inspected in Figs 7.7 and 7.8. The variance reduction (VR) is ratio of misfit and norm of data vector $\|\boldsymbol{d}_{obs}\|$

$$\begin{aligned} \mathrm{VR} &= \left(1 - \frac{\mathrm{misfit}_i}{\|\boldsymbol{d}_{obs}\|}\right) \cdot 100\,\% = \\ &= \left(1 - \frac{\left(\boldsymbol{d}_{obs} - \mathbf{G}_i \widetilde{\boldsymbol{m}}_i\right)^T \mathbf{C}_D^{-1} \left(\boldsymbol{d}_{obs} - \mathbf{G}_i \widetilde{\boldsymbol{m}}_i\right)}{\boldsymbol{d}_{obs}^T \mathbf{C}_D^{-1} \boldsymbol{d}_{obs}}\right) \cdot 100\,\% \,. \end{aligned} \tag{7.25}$$

Here we show some examples of figures produced by the code. If it is not specified in the figure caption, the figures are related to the same earthquake as the text output above.

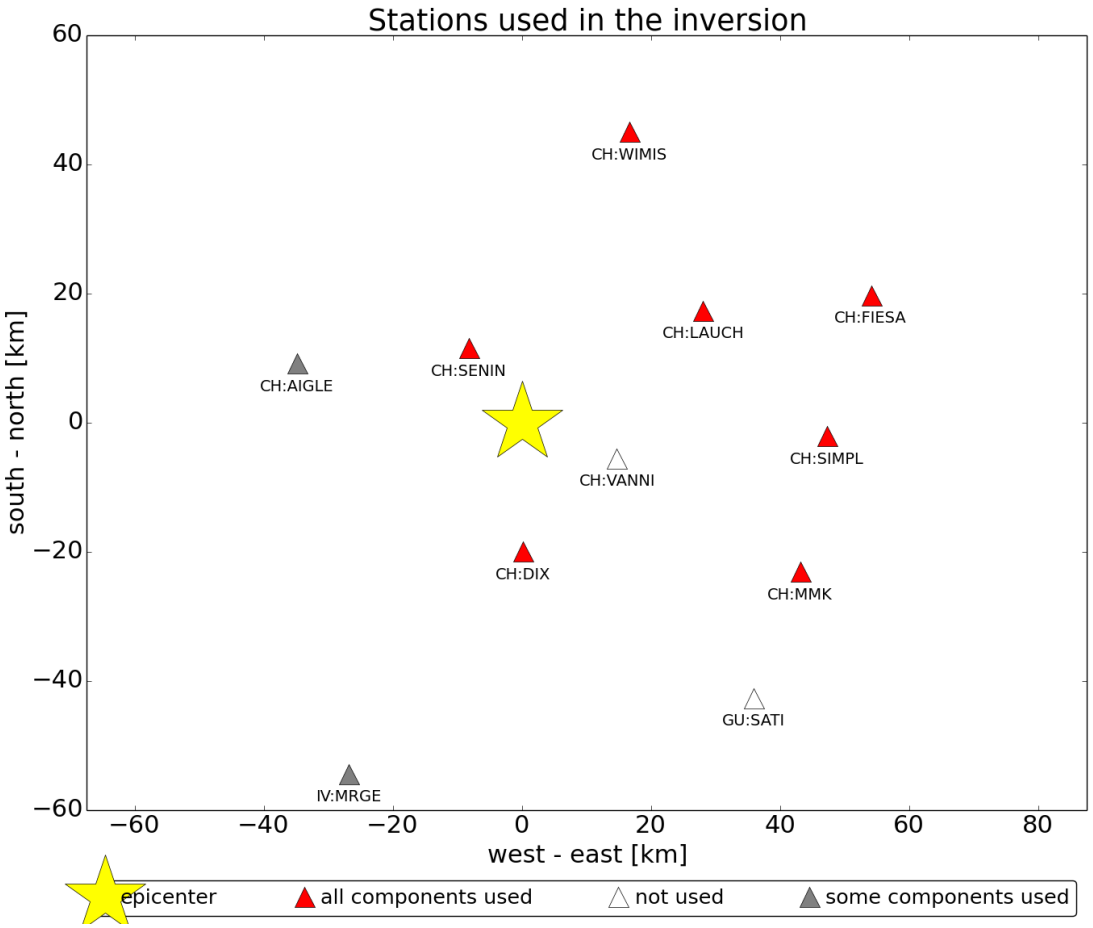

Figure 7.1: Map of stations used in the inversion. The epicenter is shown by a star, the station by triangles, their colors shows whether all components were used, just some of them, or none. Plotted for an $M_W = 2.9$ earthquake at Sion, Switzerland on 2015-06-20 10:30:22.

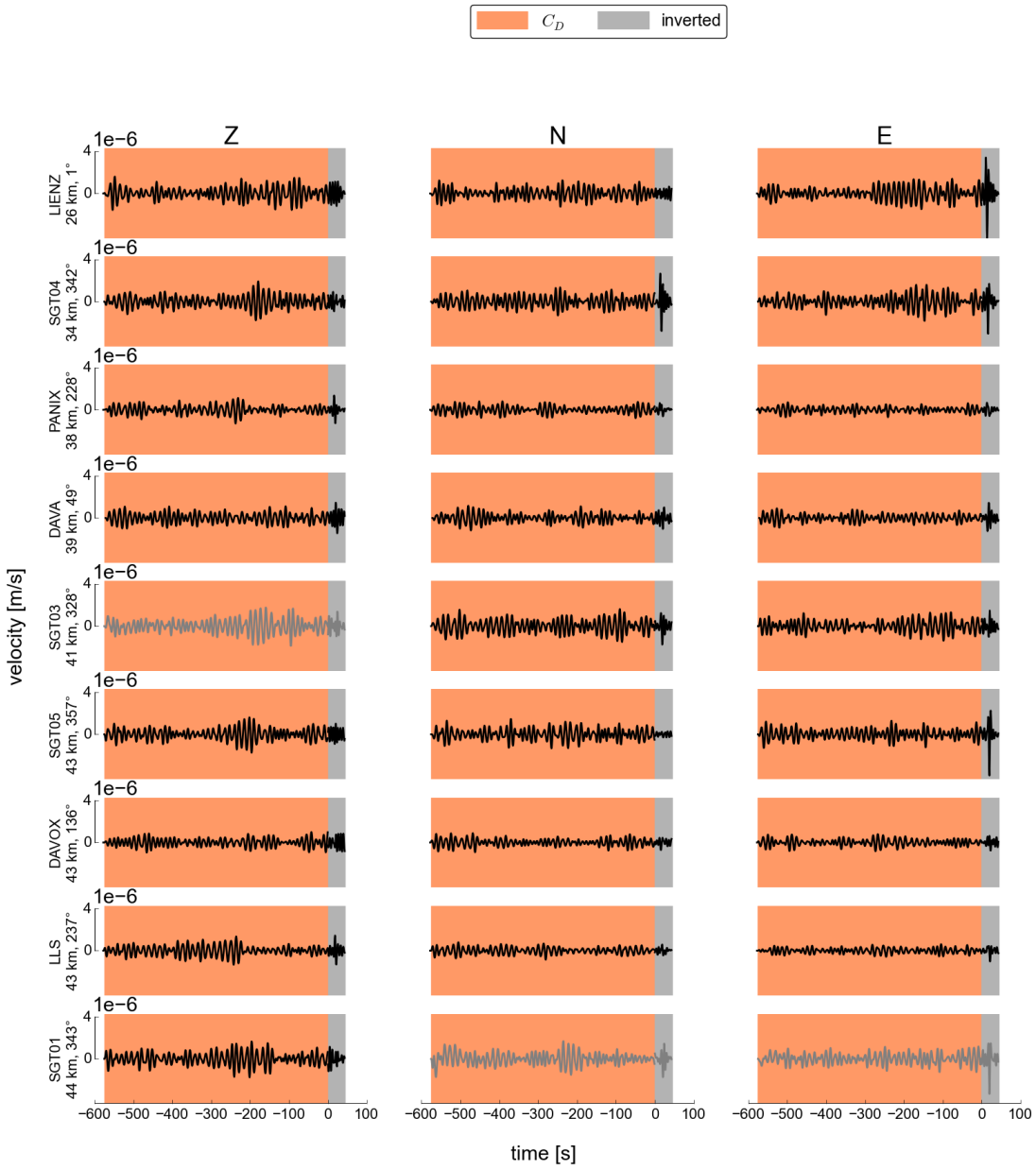

Figure 7.2: Input seismograms with highlighted time windows used and for building the noise covariance matrix $\mathbf{C}_D$ (orange) and for the inversion (gray background). Seismograms which were used in the inversion are shown in black color, the others which were skipped because of some disturbances are shown in gray. The figure enables compare the signal-to-noise level on different stations visually. Note that the records are unfiltered.

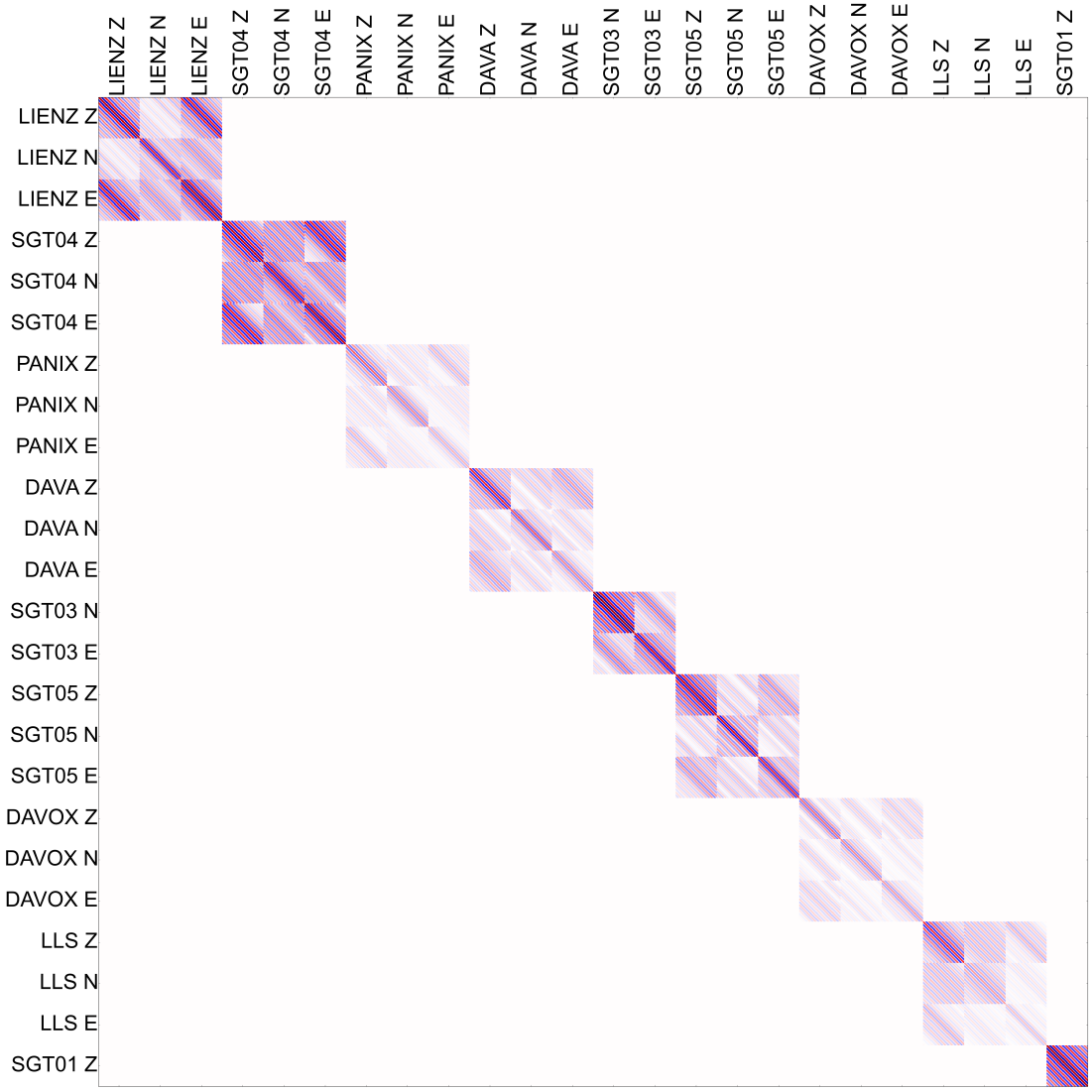

Figure 7.3: Visualization of the data covariance matrix $\mathbf{C}_D$. Positive values are shown in red, negative in blue, zero values are in white. The $\mathbf{C}_D$ is calculated from the before event noise (orange time window in Fig. 7.2). It consists of large non-empty blocks corresponding to stations, their sub-blocks correspond to auto- and cross-covariance of the 3 components. Station names and components are shown at left and top edge. There are 3×3 sub-blocks for stations where all components are present; if any of components is not used in the inversion because of a disturbance or data gap (e.g. stations SGT03 and SGT01), there are fewer sub-blocks. The correlation between stations is assumed to be zero.

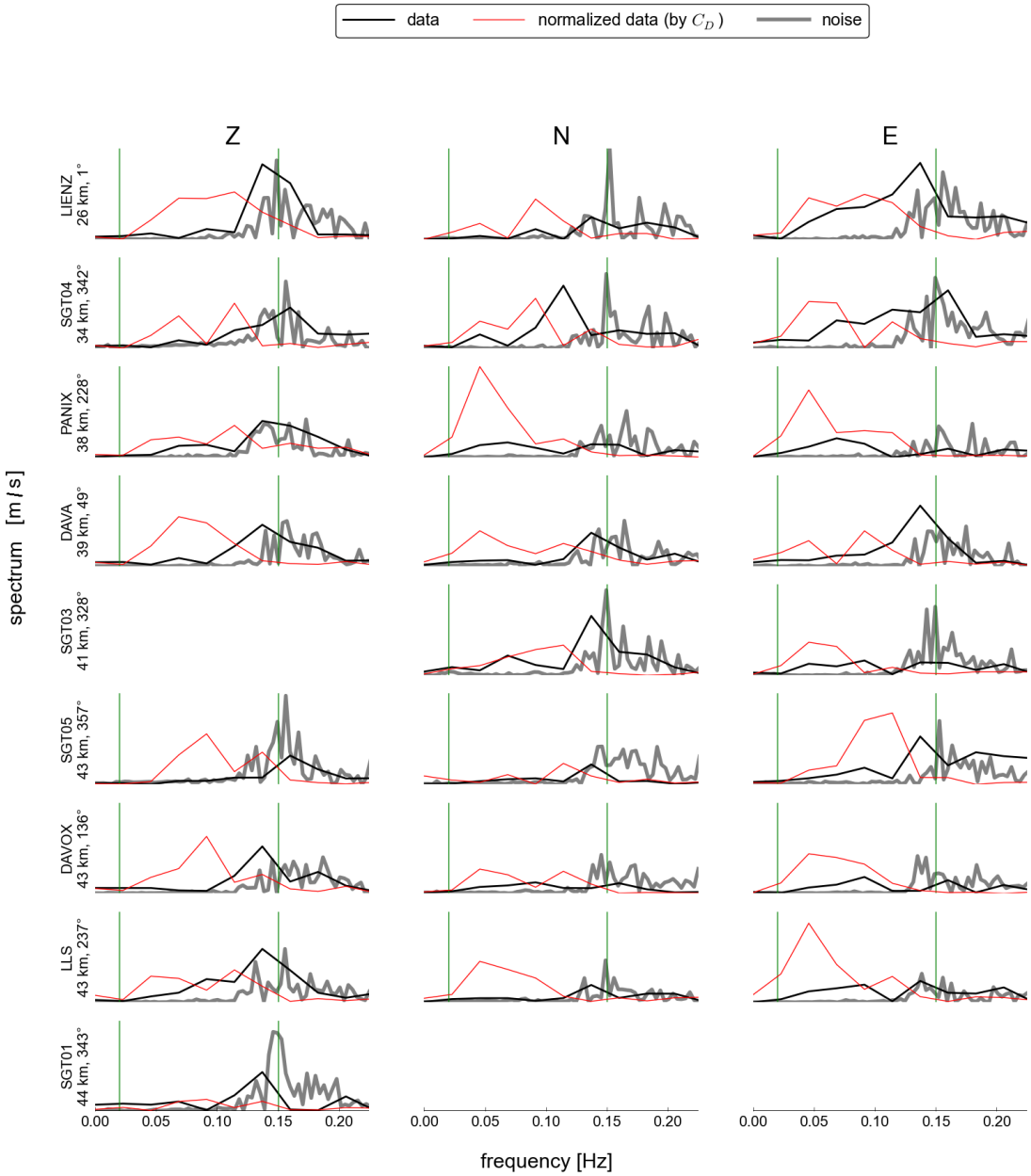

Figure 7.4: Spectral content (real part of Fourier transform) of the before-event noise (gray), inverted time window (black), and standardized data (red; obtained from the inverted time window using covariance matrix $\mathbf{C}_D$). Comparing these three lines, it is obvious that the $\mathbf{C}_D$ amplifies the frequencies less affected by noise and suppress the most noisy frequencies. The inverted frequency band is labeled by green lines. Station codes, epicentral distances and azimuths are shown on the left side.

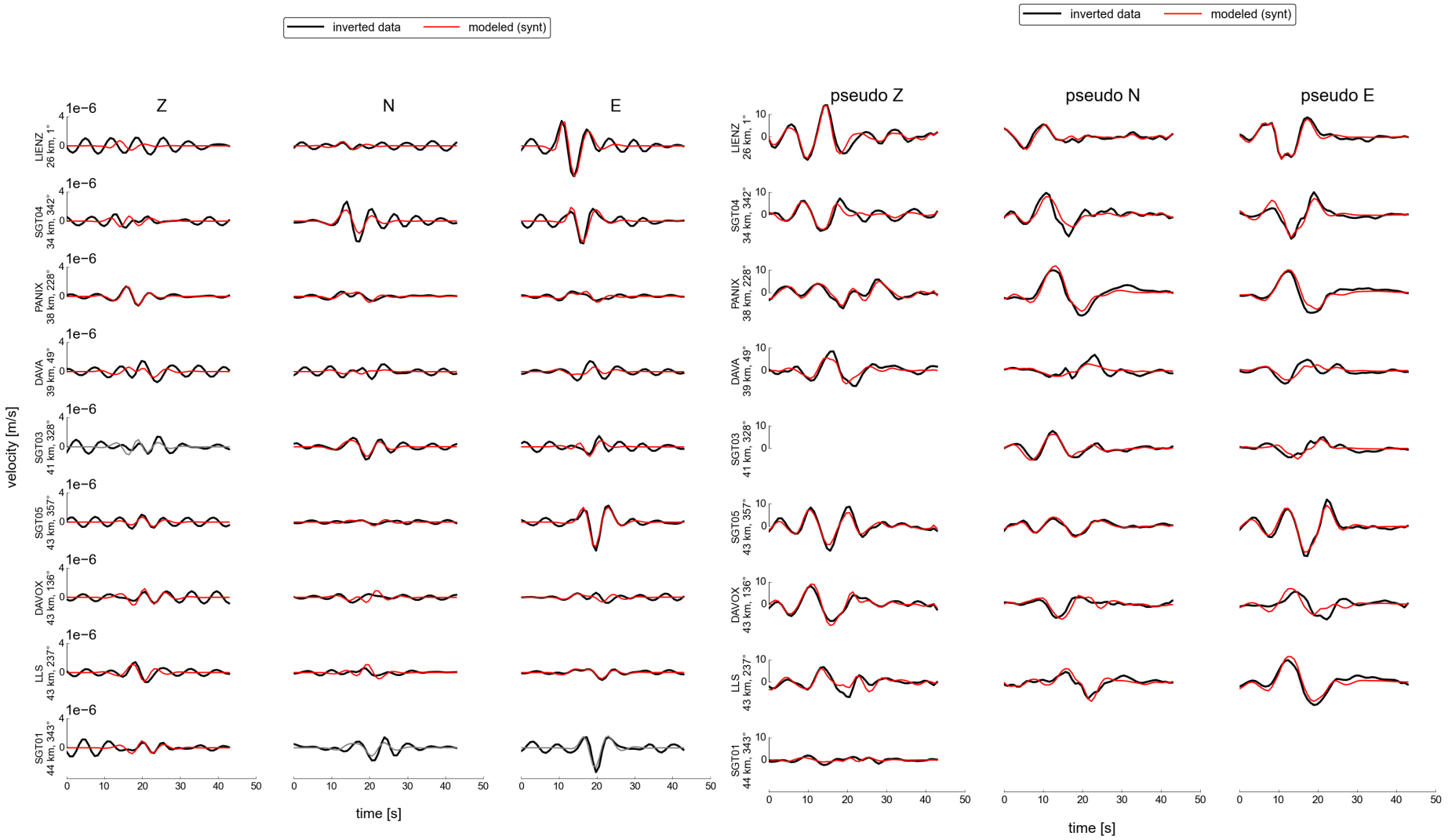

Figure 7.5: Observed (black) and modeled (red) waveforms for best-fit MT in two variants: just filtered to inverted frequency range (left) and standardized using the data covariance matrix $\mathbf{C}_D$ (right). The components of standardized data are denoted "pseudo Z" etc. because normalization using $\mathbf{C}_D$ can transfer a part of information between components (see section 6.1).

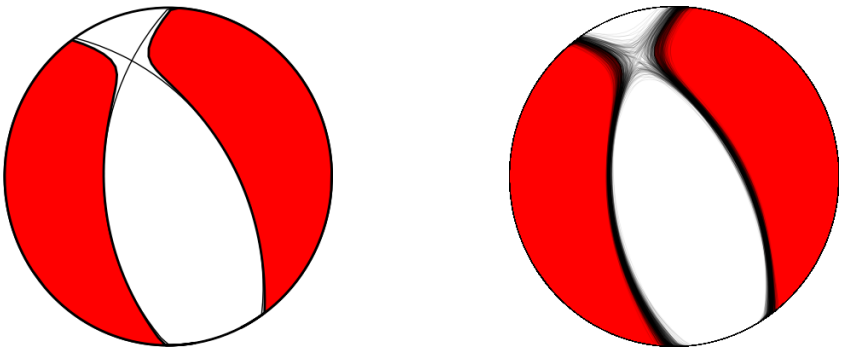

Figure 7.6: A beachball visualization of the full moment tensor of the best solution (lower hemisphere). It is possible to plot it alone (left) or together with a set of nodal lines which sample posterior probability density of the inverted parameters (right).

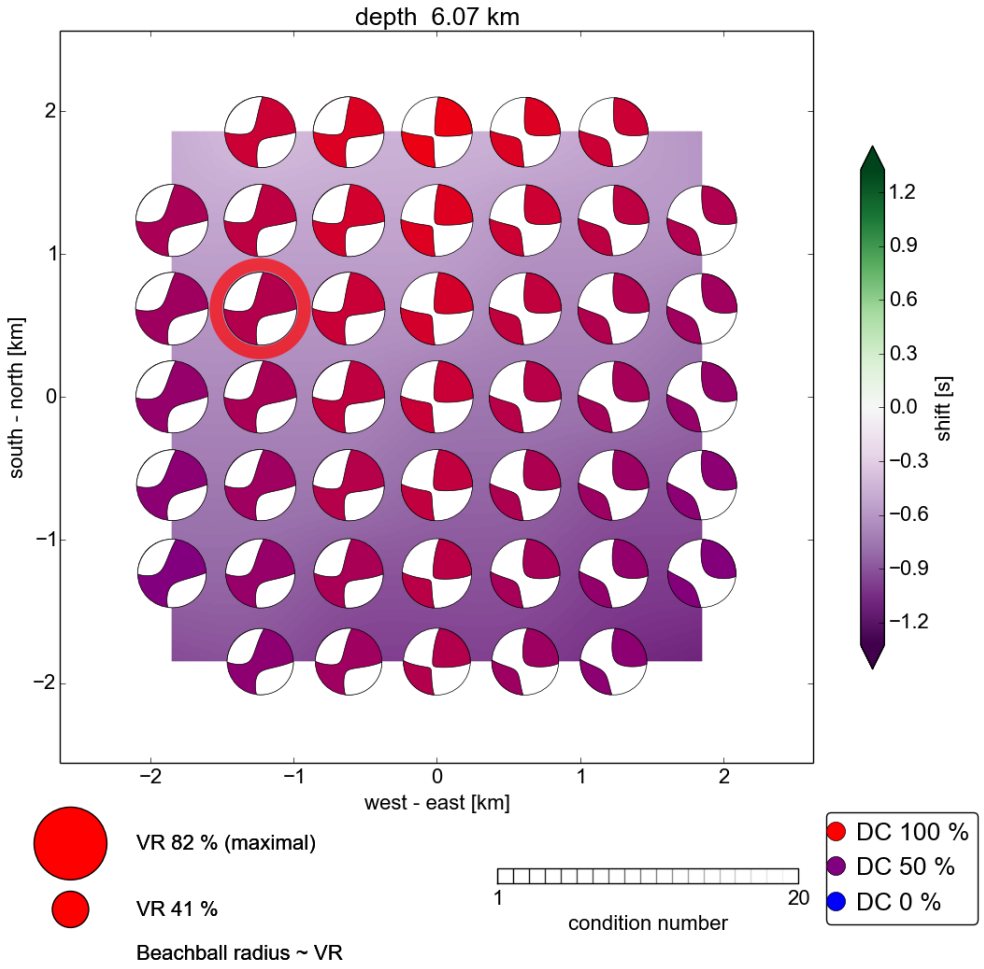

Figure 7.7: Spatial variability of the solution. It is sectional view in the horizontal plane for the selected depth of 6.07 km. The color of the beachball corresponds to the DC percentage for the best solution at a given grid point. The beachball size corresponds to the variance reduction (VR) and the color in the background corresponds to the inverted centroid time at a given grid point. The best solution is encircled.

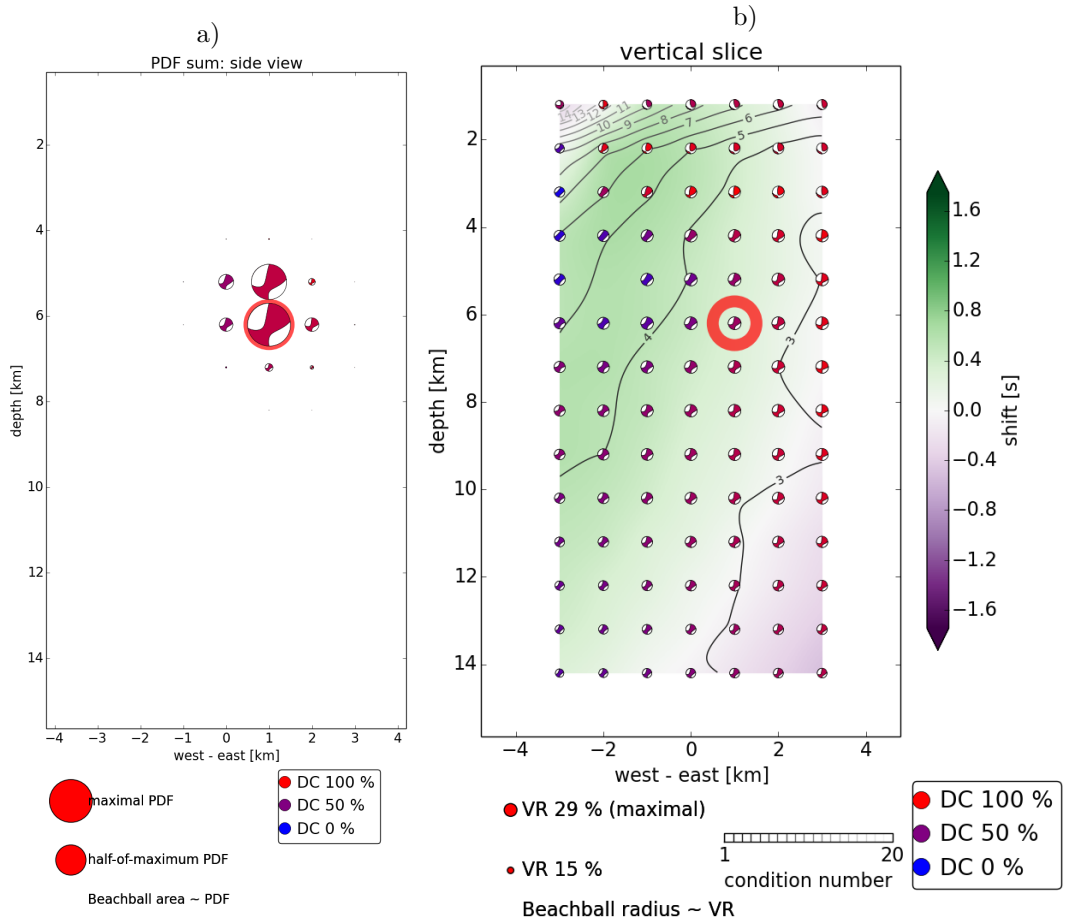

Figure 7.8: Solution varying with depth and west-east coordinate (view from the south). The color of the beachball corresponds to the DC percentage for the best solution at a given grid point. In panel (a), the size of the beachballs corresponds to the posterior probability density function (PPDF) and the PPDF is summed over third dimension (N-S coordinate) and time. In panel (b), the beachball size corresponds to the variance reduction (VR), the solutions are shown in the plane in which the best solution (circled) lies, the color in the background corresponds to the inverted centroid time at a given grid point, and the contour lines show the condition number. Plotted for an $M_W = 3.7$ earthquake at Sargans, Switzerland on 2013-12-27 07:08:28.

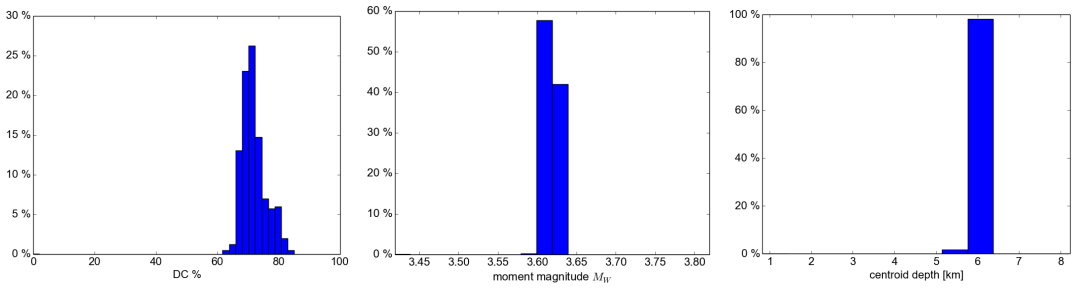

Figure 7.9: Histograms showing marginal probability density for selected parameters: double-couple percentage (left), moment magnitude (middle) and centroid depth (right). The marginal probability density are calculated from an ensemble of random points, which sample posterior probability density function, for details see Section 3.3.

7.12 Result presentation

Usually, there is a need to publish the results of automated processing on the Internet or to share them with somebody. We have chosen the HTML format as the best option for such applications, because an HTML page can be formatted in a flexible way which adapt to the size of reader's device and it enables to present sets of images as a gallery of thumbnails which can be enlarged.

The ISOLA-ObsPy package contains a function `html_log`. It creates an HTML page containing a description of the result illustrated by figures created by functions described in Section 7.11. We can decide which plots should be included in HTML report and/or add a reference solution for comparison by setting parameters of the function. An example of the HTML output is attached as an Attachment A.1 at page 114.

8. Tests and applications of the developed method

8.1 Synthetic tests

This section includes tests published in Section 4 in Vackář et al. [2017].

There are two representative synthetic tests presented in this section. They show that the proposed method can not only assess the uncertainty of the CMT solutions with respect to seismic noise, but it can also improve the CMT results. The improvement is possible because when analyzing the noise, the inversion can automatically be focused onto the least noisy part of the data.

8.1.1 Dependence of the uncertainty on the noise level and number of stations

To illustrate the performance of the proposed method, we conduct a synthetic test showing behavior of the Bayesian inversion for different noise levels and station configurations (Fig. 8.1). We generated synthetic waveforms (in the same velocity model as used in the inversion), then we added white noise of specified level, and used it as "data" in the inversion. Narrowing the marginal probability of each parameter can be observed for higher number of stations, lower noise level, and better azimuthal coverage. The marginal probability densities are plotted by method described in Section 3.3. The dependence on the noise level is driven by the data covariance matrix $\mathbf{C}_D$ (described in Chapter 6), which reflects the properties of before-event noise.

The marginal probability distribution is not always centered at the true solution (for which synthetic seismograms were generated; red line in the figure), but usually close to the best fitting model, which can be biased. The bias changes for every realization of random white noise. The 'DC %' parameter never has a maximum at 100 % because every perturbation around a pure-DC mechanism results in a non-DC part, so obtaining pure-DC moment tensor is highly improbable when generating realizations within a given probability density function. But maximum probability of 'DC %' gets closer to original 100 % when the uncertainty is decreasing.

number of station	3	8	3	3	8
noise	strong	strong	weak	weak	weak
max. azimuthal gap	138° (good)	105° (good)	329° (poor)	138° (good)	105° (good)
condition number	5	6	10	5	6
variance reduction	14 %	8 %	71 %	71 %	62 %

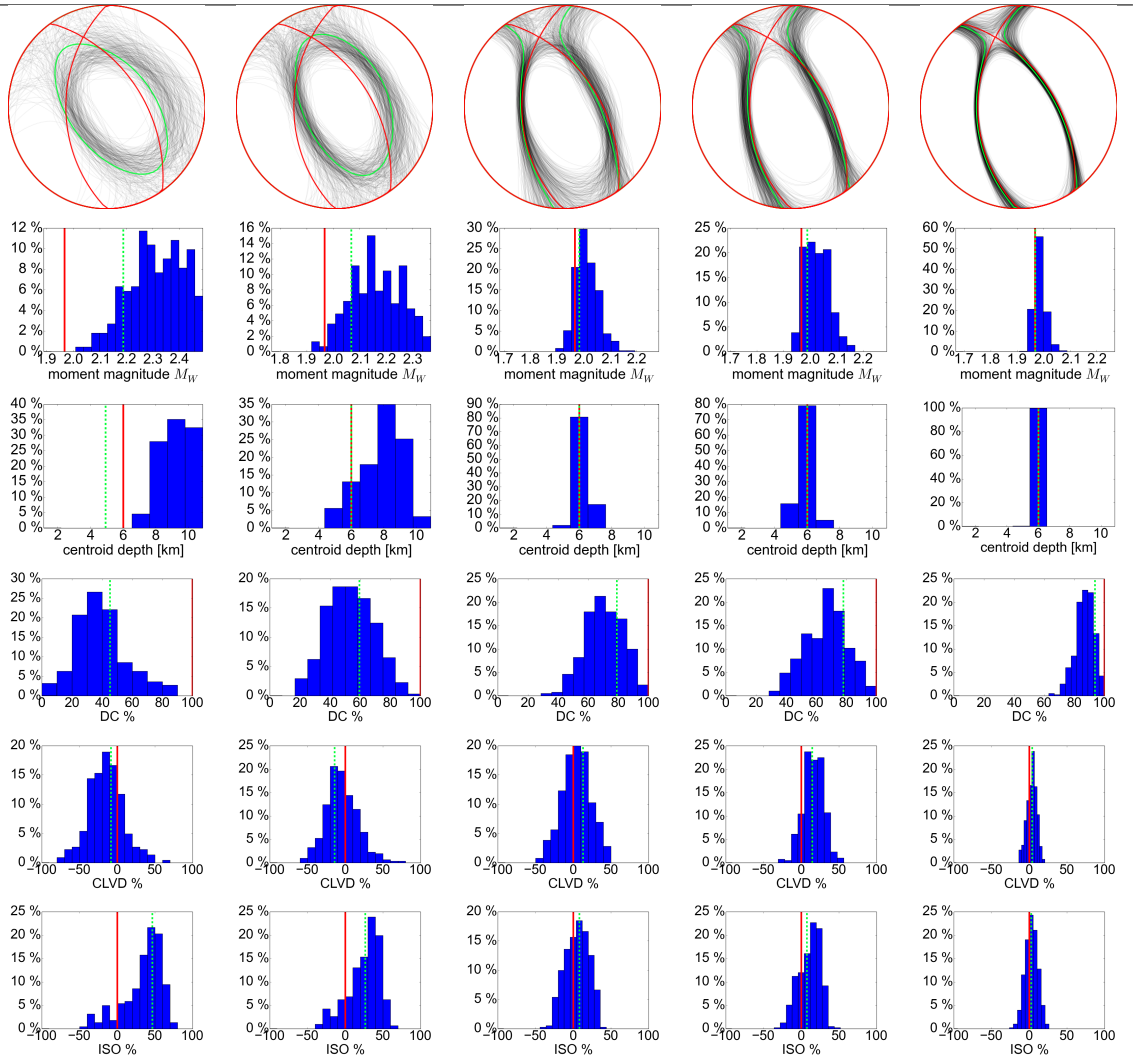

Figure 8.1: Case example (synthetic test), how the Bayesian uncertainty of the resulting CMT varies in five different configurations. 400 focal mechanisms were generated randomly based on the calculated PPDF (see Section 3.3). The configurations differ by the number of the stations, their azimuthal distribution, and by the noise level. True parameters are shown in red and the best solution by the green dotted line. Marginal probability densities are shown for nodal lines, moment magnitude Mw, centroid depth and for the MT decomposed into its double-couple, CLVD and isotropic component [Vavryčuk, 2015]. The marginal probability function gets narrower (more focused) as the number of the stations increases, their azimuthal coverage improves, and as the noise decreases. Noise denoted 'strong' has 4 times higher standard deviation than 'weak' one.

8.1.2 White noise test, station dependent

In practice, the seismic noise level often varies from station to station. An automatic algorithm or manual operator needs to choose the stations according their signal-to-noise ratio. In this test we examine ability of the data covariance matrix to automate such a procedure, i.e. to prefer the stations at which the noise level is low. Because in practice we often use the same frequency range at many stations, and this range is relatively narrow (1–2 octaves wide), for simplicity here we assume a white noise.

We simulated waveforms of an event with a given focal mechanism, adding a strong white noise to 3 stations of 5, and weak noise to the others. The level of the "strong noise" was chosen to be such that in manual processing such stations would be eliminated. The reason was to test the capability of the procedure to manage extreme conditions. Then we sampled down the waveforms to the rate 1.2 Hz, dropping frequencies above the Nyquist frequency, and then we filtered them by Butterworth filter to frequency range 0.02–0.15 Hz.

The results are presented in Figs 8.2–8.6. As a reference, we show best-fitting solution with a diagonal $\mathbf{C}_D$ (the same standard deviation for all stations). It is given just as an example of a common approach for the purpose of comparison with our new method. The covariance matrix automatically down-weighted the strongly disturbed stations, so that the inversion is controlled almost entirely by the low-noise stations. It usually improves results, but sometimes might produce unfavorable station geometry. To identify such cases, we recommend to have a look at the plot of standardized data together with the plot of the station geometry (panels (a) and (g) in Fig. 8.2).

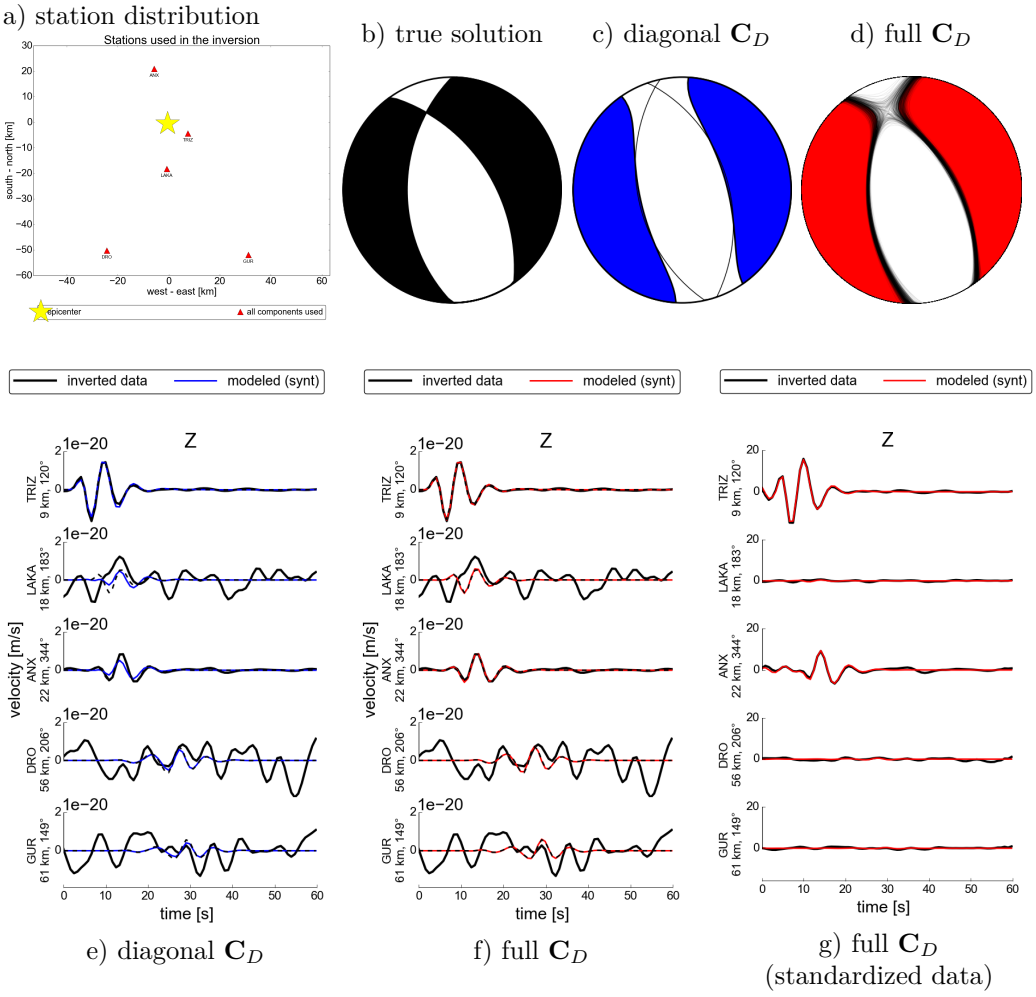

Figure 8.2: White noise synthetic test: (a) source-station configuration, (b) mechanism for which waveforms were generated ('true solution'), (c) best-fitting solution with a diagonal $\mathbf{C}_D$ (the same standard deviation for all stations), (d) best-fitting solution with full (i.e. block-diagonal) data covariance matrix $\mathbf{C}_D$ (Chapter 6). Waveform comparison for: (e) solution with a diagonal $\mathbf{C}_D$, (f) solutions with full $\mathbf{C}_D$–original seismograms and (g) solutions with full $\mathbf{C}_D$–multiplied by Cholesky decomposition of the $\mathbf{C}_D$ (see Section 6.1), 'standardized data'. Panels (e–g) show original waveforms without noise (dashed black lines), waveforms with the added white noise which were inverted (solid black lines), and modeled waveforms for the retrieved focal mechanism (colored solid line). Comparing panels (f) and (g) it is demonstrated that the covariance matrix strongly up-weighted the weak-noise stations.

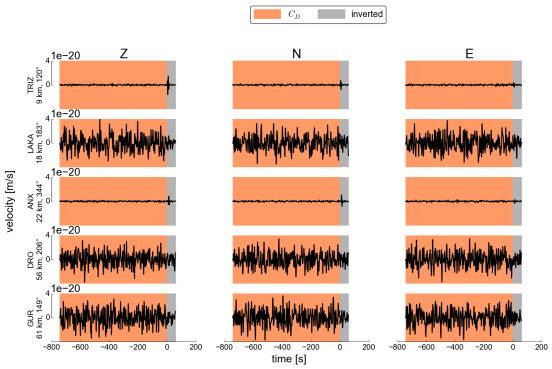

Figure 8.3: White noise synthetic test: noise in the seismic data. The covariance matrix $\mathbf{C}_D$ is calculated from a time window preceding the event (orange). It is at least ten times longer than the signal time window used in the inversion (gray).

(a) diagonal $\mathbf{C}_D$ (b) $\mathbf{C}_D$ from noise covariance

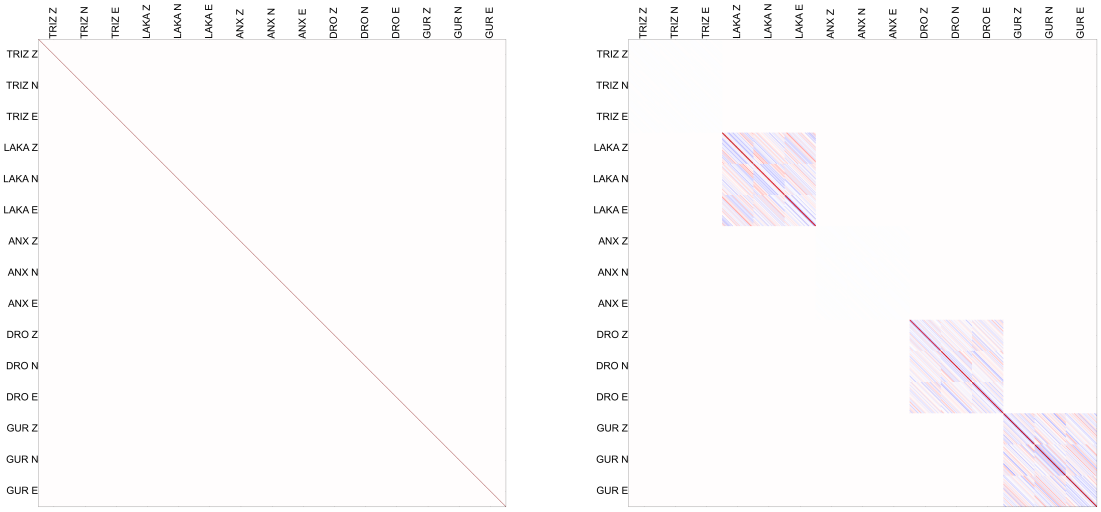

Figure 8.4: White noise synthetic test: Covariance matrices used. (a) A diagonal matrix with the same standard deviations for all stations. (b) Matrix from noise covariance function. The values for the stations with weak noise level are so low, that look like zero (white) block.

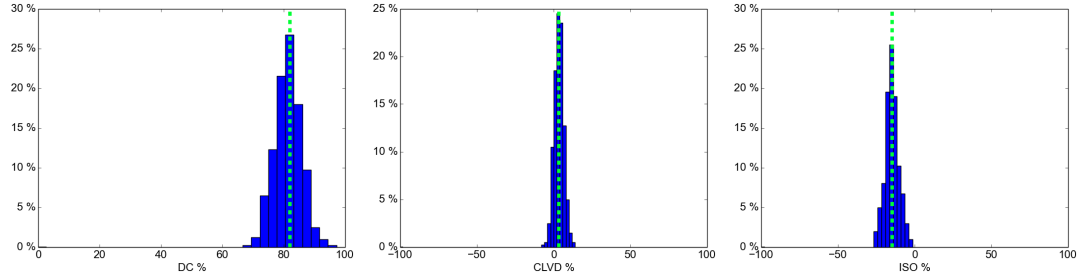

(a) double-couple part (b) CLVD part (c) isotropic part

Figure 8.5: White noise synthetic test: Uncertainty histograms for solution with full (i.e. block-diagonal) data covariance matrix $\mathbf{C}_D$. The green dotted line shows the best solution.

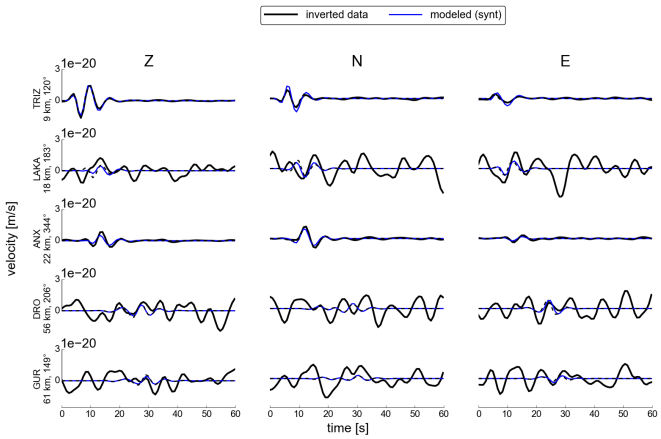

(a) original seismograms of solution with diagonal $\mathbf{C}_D$

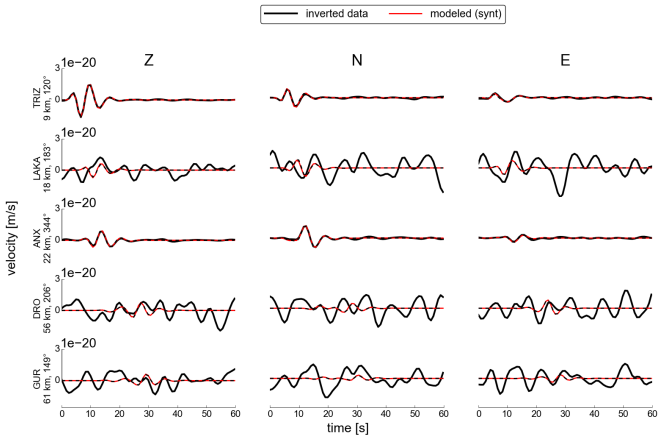

(b) original seismograms of solution with $\mathbf{C}_D$ from noise covariance

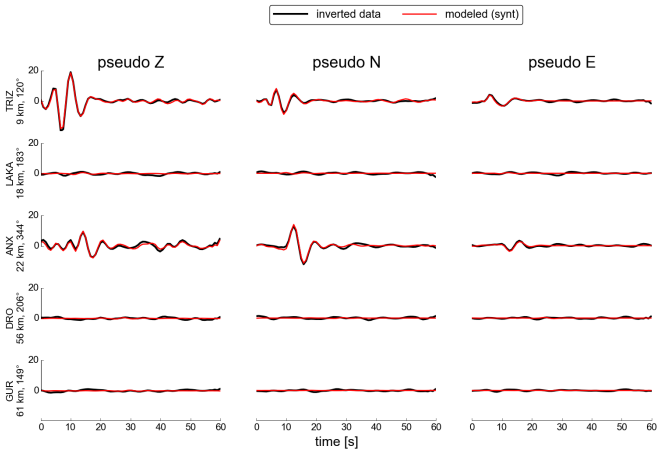

(c) 'standardized data' of solution with $\mathbf{C}_D$ from noise covariance—seismograms multiplied by Cholesky decomposition of the $\mathbf{C}_D$

Figure 8.6: White noise synthetic test: Waveform fit. In all panels, there are original waveforms without noise (dashed black lines), inverted waveforms with the added white noise (solid black lines), and modeled waveforms for the retrieved focal mechanism (color solid line).

8.1.3 Colored (correlated) noise

In real data we always encounter a frequency-dependent noise, and standard manual CMT inversions need to carefully select a frequency range with suitable signal-to-noise ratio. For example, in regional CMT inversions, we can usually use only frequency range below the microseism noise. In this synthetic test we study whether the covariance matrix of the data is able to avoid the noisy part of spectrum automatically.

We simulated waveform for the same focal mechanism as in the previous example and added coloured noise of the same spectral content to all stations. The noise is strong between frequencies 0.05–0.25 Hz, while it is negligible outside this frequency band. Again, the level of the strong noise is such that in manual processing that spectral range would be avoided. Then we down-sampled the waveforms to the rate 4 Hz, dropping frequencies above the Nyquist frequency, and then we filtered them by Butterworth filter between 0.10–0.50 Hz.

The results are shown in Figs 8.7–8.11. It shows that the new method with the data covariance matrix avoids using the noisy frequency range itself, so it indeed works as an automated filtering scheme.

In both synthetic tests we compare the new method (which uses the full data covariance matrix $\mathbf{C}_D$, described in Chapter 6) with solution using diagonal $\mathbf{C}_D$, which assumes the same standard deviation for all stations. The method with diagonal $\mathbf{C}_D$ is equivalent to simple minimization of difference between the observed and simulated data in L^2 norm, which is common in MT inversion. In this sense, the new method represents improvement compared to the common approach. We observe that the new method finds the best solution closer (both in time and space) to the 'right' centroid position than the method with a diagonal $\mathbf{C}_D$.

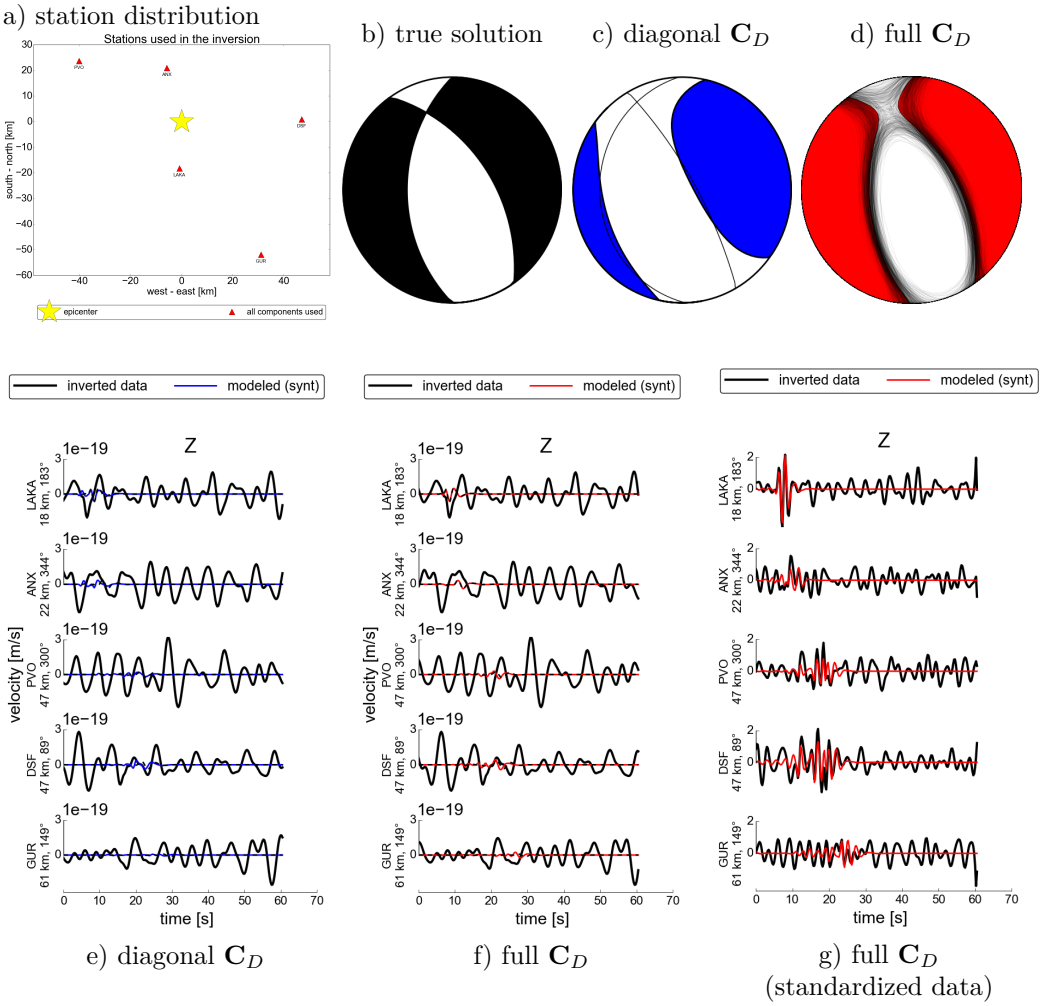

Figure 8.7: Same as Fig. 8.2, but for colored noise synthetic test: Strong noise in the frequency band 0.05–0.25 Hz at all stations. The inverted frequency band is 0.10–0.50 Hz, so only its higher part is not disturbed (noise free). The inversion with the covariance matrix $\mathbf{C}_D$ (panel d) provides a solution close to the right one, contrasting with a wrong solution with a diagonal $\mathbf{C}_D$ (panel c). Comparing panels (f) and (g) it is obvious that the covariance matrix serves as an automatic frequency filter enhancing the undisturbed part of the spectrum, thus improving the inversion.

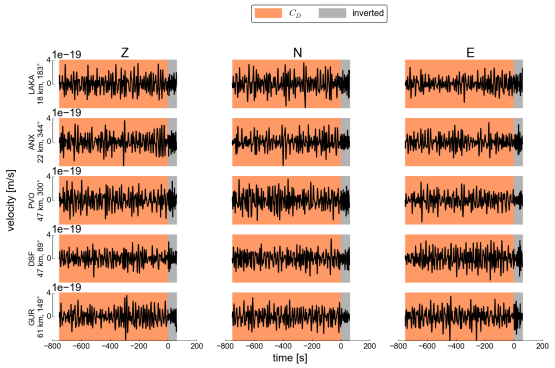

Figure 8.8: Colored noise synthetic test: The covariance matrix $\mathbf{C}_D$ is calculated from a time window preceding the event (orange). It is at least ten times longer than the signal time window used in the inversion (gray).

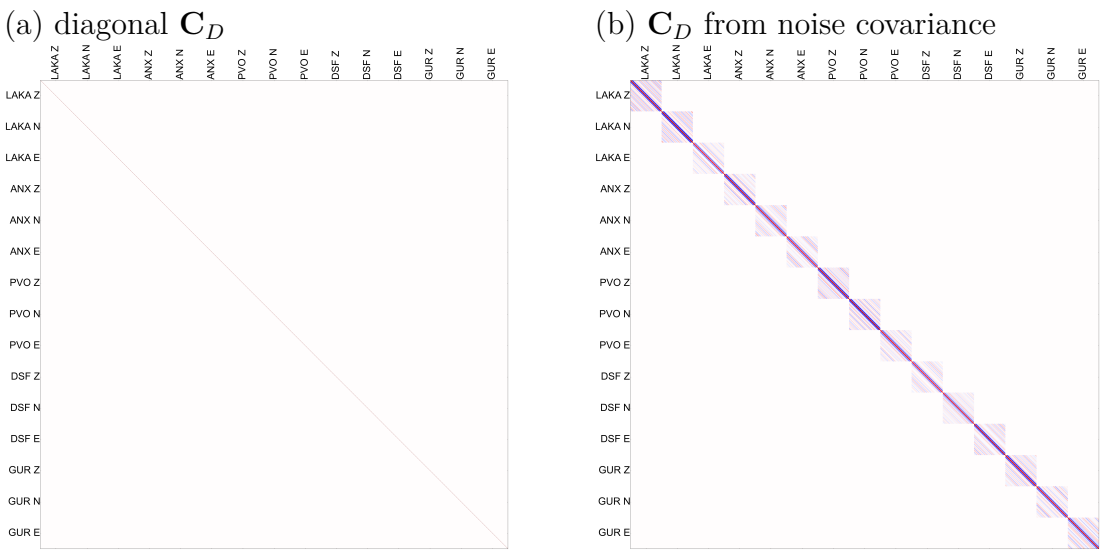

Figure 8.9: Colored noise synthetic test: Covariance matrices used. (a) A diagonal matrix with the same standard deviations for all stations. (b) Matrix from noise covariance function.

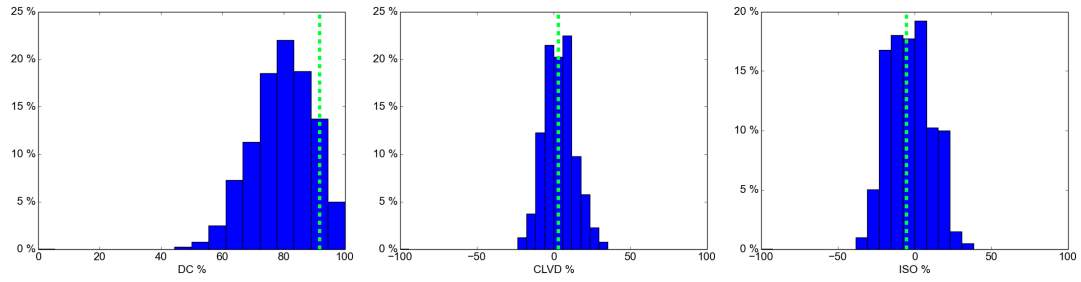

(a) double-couple part (b) CLVD part (c) isotropic part

Figure 8.10: Colored noise synthetic test: Uncertainty histograms for solution with full (i.e. block-diagonal) data covariance matrix $\mathbf{C}_D$. The green dotted line shows the best solution.

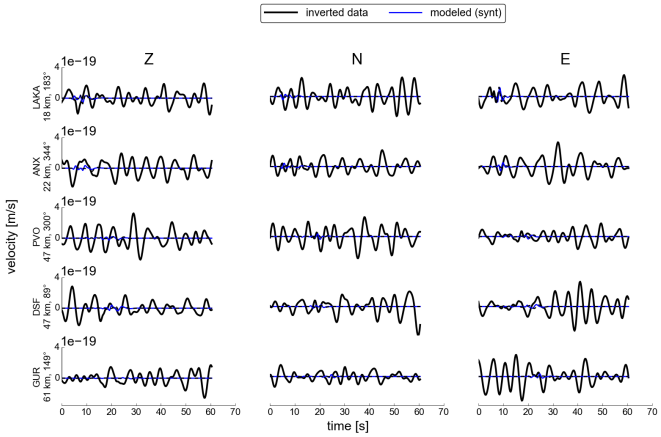

(a) original seismograms of solution with diagonal $\mathbf{C}_D$

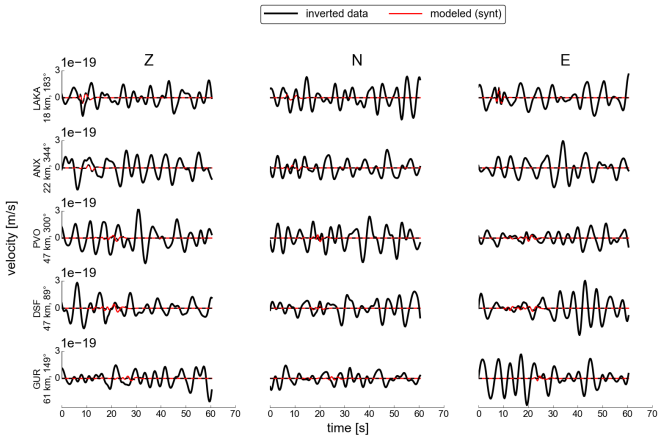

(b) original seismograms of solution with $\mathbf{C}_D$ from noise covariance

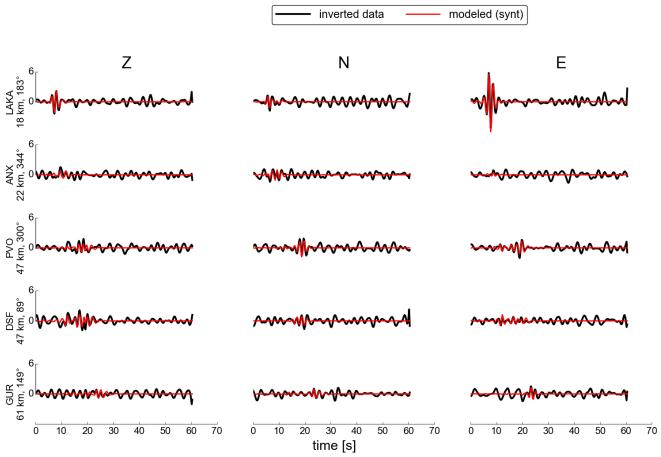

(c) 'standardized data' of solution with $\mathbf{C}_D$ from noise covariance—seismograms multiplied by Cholesky decomposition of the $\mathbf{C}_D$

Figure 8.11: Colored noise synthetic test: Waveform fit. In all panels, there are original waveforms without noise (dashed black lines), inverted waveforms with the added white noise (solid black lines), and modeled waveforms for the retrieved focal mechanism (color solid line).

8.2 Inversion of real events — Comparison with Swiss MT catalog

This section is based on Section 5 in Vackář et al. [2017].

In order to evaluate the performance of the proposed algorithm, we systematically compare CMT solutions using this approach with an independent methodology. As a reference event data set we have selected all (139) events with magnitude ≥ 3 from the Swiss earthquake catalogue from from 1999 to June 2015 (see `http://arclink.ethz.ch/fdsnws/event/1/query?starttime=1999-01-01T01:00:00&endtime=2015-07-01T00:00:00&minmagnitude=3.0&format=text&nodata=404`). We have chosen the year 1999 as this was the start of the Swiss Digital Seismic Network (SDSNet), the broadband component of the Swiss Seismic Network [Swiss Seismological Service (SED) at ETH Zurich, 1983]. We compare the results from our method with moment tensor solutions obtained from the scmtv module from SeisComP3 package [Hanka et al., 2010] (hereafter called as 'manual processing'). For both methods, a similar set of 1-D Green's Functions, optimized for the Alpine region [Diehl et al., 2009], is used. Local and Regional MT catalogues for Switzerland have been produced by the SED in the past [Bernardi et al., 2004; Braunmiller et al., 2002], though at the SED these methods have been discontinued and now are replaced by the scmtv approach. For both the methods, all broadband data that is available in the archives of the SED are used. This includes data not just from Switzerland, but also from foreign networks that provide realtime data to the SED, see Dedication of the thesis on page iii for details. Sensors used in the inversion are restricted to broadband sensors ranging from 40s–120s, though the majority of 120s.

The manual processing uses the workflow implemented within the routine catalogue curation at the Swiss Seismological service. The methodology is based on the linear least squares inversion of Dreger [2003]. The methodology assumes that the isotropic component is zero, the epicentral coordinates are fixed (though the depth can vary), and the source time function is fixed, so it is an MT rather than CMT approach. A limited set of predefined parameters is used to select stations and prepare the data, which is automatically implemented depending on the events' Local Magnitude (ML) as contained in the earthquake catalogue. These include channel types (broadband), candidate stations (based on epicentral distance) and narrow band filter ranges. These parameters can be modified though this is rarely necessary and hence rarely done. An automatic algorithm can be applied to select the optimal set of stations and event depth that produces the best MT, taking into account the Variance Reduction and the % Double Couple of the solution, whilst retaining as many stations as possible. Interactively, the solution can be tweaked to select and remove individual station components.

Of the 139 candidate events, MT solutions were obtained for 40 events. The remaining events could not provide a high quality solution for various reasons: too few station components provide high waveform fits with high Variance Reduction due to high background noise, too few stations are available (a small event is located at edges of the network, or the event occurred during the start of the network when station density was sparse). These 40 events were also processed by our new automated code.

The automated procedure followed using the proposed algorithm; all broadband stations within a radius controlled by the M_L magnitude (obtained during catalogue creation at the Swiss Seismological Service) were used. The maximum epicentral distance was limited according to ad hoc formula $r < 2^{2 \cdot M_L}$ km. Moreover, stations closer than 2 km were removed, because they make inversion unstable in many cases. Stations components, where instrumental disturbances were detected automatically by the MouseTrap code [Vackář et al., 2015], were removed. Also eliminated were records with data gaps in the period required for the earthquake and the noise analyses. The code does not remove any station with high noise because we wanted to test practical ability of the covariance matrix to manage datasets with noisy stations. We require at least 2 stations which have at least 5 usable components, otherwise the event was removed.

Prior to the inversion, the mean was subtracted from the records and 4-pole Butterworth bandpass filter was applied restricting the frequency range to 0.02–0.15 Hz. Moreover, for stations with epicentral distance larger than 100 km, the high frequency limit was restricted in such a way that the minimum wavelength is no more than 5 times shorter than the source to station distance for a reference S-wave velocity 3 km/s. The restriction is to prevent errors arising from inaccurate Earth model resulting in Green's function modeling errors [Hallo and Gallovič, 2016] as well as limited frequency range of the sensor. The centroid position was searched on a grid with sampling 1 km (both in horizontal and vertical direction).

For each event, the procedure calculates the CMT in 4 cases: (i) deviatoric MT using a diagonal covariance matrix (the same variance for all stations, i.e. we just minimize L^2 norm between observed and synthetic waveforms), (ii) deviatoric MT using the data covariance matrix $\mathbf{C}_D$ created just from autocovariance, (iii) deviatoric MT using $\mathbf{C}_D$ including crosscovariance between components of single stations, and (iv) full MT using $\mathbf{C}_D$ including crosscovariance between components. We observed some difference between the first case with diagonal covariance matrix (i) and the others, but the difference between the cases with $\mathbf{C}_D$ calculated from noise covariance (ii–iv) was usually insignificant; only occasionally we observed some small improvement (particularly in higher DC-percentage, which we assume for tectonic earthquakes, and in higher variance reduction) in the cases with crosscovariance (iii–iv). For comparison with manual processing, we have chosen the case with crosscovariance and deviatoric MT (iii), because the manual solution uses deviatoric MT too.

Comparison of the automatic and manual processing is illustrated in Fig.8.12. The comparison is quantified by measuring the difference in the orientation of the DC parts of the moment tensors using Kagan's angle [Kagan, 1991], and the difference in depth and moment magnitude M_W. The majority of the automatically processed events (over 70 %) have similar focal mechanism as that obtained in the manual SeisComP3 processing, as expressed by their Kagan angle 0°–20°. Events with large Kagan angle were inspected manually (the first three lines of Tab. 8.1); in all cases, there was another problem with the event, e.g. large azimuthal gap, a not-detected disturbance in inverted waveforms, unstable mechanism strongly varying with depth with almost the same variance reduction, or a combination of these problems. The difference in moment magnitude is below 0.05 at the majority of the events, and within 0.15 in more than 90 % cases. We also compared the inverted centroid depth, and found the difference lower than 2.5 km for 44 %

of the events. Taking into account that the station set was usually different in both methods we consider these results as a good agreement.

In addition to this comparison we also summarize our new automatic solutions for all 139 inverted events of Swiss Digital Seismic Network including also events having no counterpart in the manual processing. At each inverse problem we have to decide whether we trust the solution or not. Although some objective measures, like variance reduction or condition number, might be helpful in this point, the decision is always partly subjective and depends on specific application. For the described procedure, we empirically set up a criterion which defines reliable ("trusted") solutions based on variance reduction VR, condition number CN (square root of the ratio of the maximal to the minimal eigenvalue of the matrix $\mathbf{G}_i^T \mathbf{C}_D^{-1} \mathbf{G}_i$ in Eq. 3.1), double-couple percentage DC, and standard deviation of the following parameters: double-couple and CLVD percentage, moment magnitude M_w, centroid time t, and centroid position x, y, z. The standard deviation of parameters is measured from the points sampling the calculated PPDF. The criterion to consider the solution as reliable is

$$\begin{aligned} VR > 0.5 \ \wedge \ CN < 8 \ \wedge \ DC > 50\,\% \ \wedge \\ \wedge \ \frac{\sigma_{DC} + \sigma_{CLVD}}{100\,\%} + \frac{\sigma_{M_w}}{1} + \frac{\sigma_t}{1\ \mathrm{s}} + \frac{\sigma_x + \sigma_y + \sigma_z}{1\ \mathrm{km}} < 2\ . \end{aligned} \tag{8.1}$$

The formula indicates trust in solutions with good waveform fit, which are well resolved (measured by the condition number), with dominant DC part (assuming tectonic origin), and with small uncertainty. The variance reduction is calculated using the standardized data ($\boldsymbol{d}'_{obs}$ and $\boldsymbol{d}'$, Section 6.1).

From the 139 events there were 24 events skipped, because too few stations were available. Of the 115 remaining events, there were 45 events which passed the criterion (Eq. 8.1). These events, together with their solutions, are plotted in Fig. 8.13 and the statistic of some of their parameters is plotted in Fig. 8.14. There is also detailed output of the ISOLA-ObsPy code for one example event in the Attachment A.1. Most of the trusted events have their variance reduction in the range 0.8-0.9 and condition number between 2–4. From this set, 32 events have their counterpart in the manual processing and 13 events were newly obtained. The 70 untrusted events include also 8 events previously manually processed. We inspected in detail all the removed and newly added events one by one. In case of 8 untrusted events, in most cases we consider that our result is not really reliable. This does not necessary mean that the result from the manual processing is not reliable too, the proper selection of stations and components as well as some other operations in manual processing may help in these specific cases. Inspecting visually all 13 newly obtained events, we confirmed all. We speculate that the reason why manual solutions cannot be made is because of the inflexibility of the manual method to accommodate narrow bandpasses in noisy records, which is a key feature of the proposed method.

The results for the removed and newly added events are listed in Tab. 8.1 and a list of all results linked with detailed output for each event is available at `http://geo.mff.cuni.cz/~vackar/CH_catalog/`. For each event, it includes several automatically generated plots and tables in form of a HTML page: centroid location, moment tensor and its decomposition including uncertainty visualization, quality measure VR and CN, uncertainty histogram for several parameters, list and map of used station, waveform fit, noise, and spectral plots,

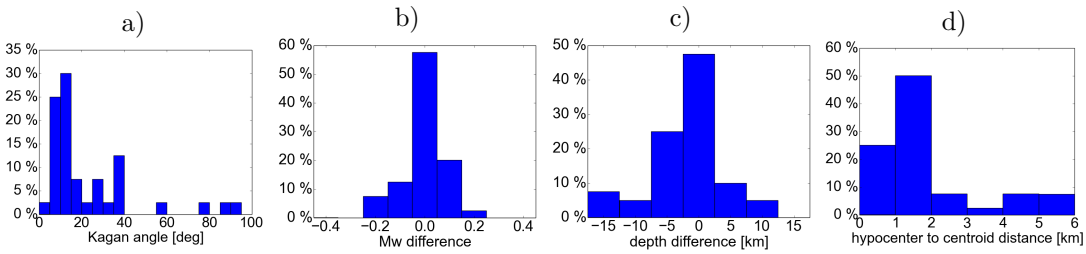

Figure 8.12: Statistics of the comparison between the new automatic processing of 36 earthquakes recorded in Swiss Digital Seismic Network and their manual processing in scmtv module of SeisComP3. Similarity of the solutions is expressed by (a) Kagan's angles, (b) differences in moment magnitude, and (c) differences in centroid depth, and (d) centroid position. All the events are shallow earthquakes with hypocenter depth up to 35 km, magnitudes are between 3.0–5.0.

data covariance matrix plot, and figures of the grid of solutions showing posterior probability density function, centroid time, variance reduction, condition number and the best solution at each grid point.

Table 8.1: Specific events. There are listed events where the manual and automated solution strongly disagree (# 1–3), where the automated solution is labeled as untrusted although the manual solution exists (# 4–11), where the automated solution is trusted although the manual solution does not exist (# 12–24), and where the solution is labeled as untrusted although we confirmed the automated solution by visual inspection (# 25). For the untrusted events the value which does not pass the criterion is shown in bold. Both numerical and graphical output for event # 25 in shown in the supplement of this thesis as an example of automated output of the code. The detailed output for all events including those not-listed in this table is available at `http://geo.mff.cuni.cz/~vackar/CH_catalog/`.

#	t	Mw	# stat	# comp	DC	VR	CN	stdev	trust	Kagan	visual	comment
1	2010-08-11 01:28:55	3.3	14	36	76	0.56	2	0.08	1	77.1	problem	fitting just stations in one direction
2	2010-06-30 11:53:44	3.6	17	37	87	0.59	2	0.03	1	86.0	OK	azimuthal gap $\sim 180°$
3	2007-03-23 05:01:38	3.3	6	14	68	0.70	2	0.78	1	58.9	uncert.	not-detected disturbance
4	2011-10-29 04:13:34	4.0	17	42	**16**	0.54	2	0.01	0	27.2	uncert.	azimuthal gap $> 180°$
5	2009-09-11 06:34:38	3.1	20	49	**11**	**0.33**	4	0.55	0	36.5	problem	$\mathbf{C}_D$ problem: an event in before-event noise
6	2009-01-04 15:30:31	3.8	18	52	**45**	**0.47**	3	0.01	0	22.0	problem	problem with near-by station
7	2003-08-22 09:30:09	3.2	15	45	85	**0.33**	3	1.18	0	36.3	uncert.	
8	2003-08-01 03:20:23	3.5	17	44	100	**0.37**	**71**	0.00	0	34.6	OK	problem with near-by station
9	2002-05-31 16:50:33	3.3	9	21	**23**	0.79	7	0.04	0	36.2	problem	problem with near-by station
10	2000-06-03 15:14:10	3.5	9	24	99	**0.40**	2	0.06	0	35.7	uncert.	
11	1999-12-31 04:55:53	4.1	13	37	**41**	0.73	3	0.02	0	93.0	uncert.	azimuthal gap $> 270°$
12	2015-06-15 03:14:47	3.0	15	33	81	0.61	2	0.52	1		OK	
13	2008-06-17 19:48:07	3.0	7	19	98	0.89	7	0.52	1		OK	
14	2006-10-20 00:11:58	3.5	7	16	88	0.52	3	0.14	1		OK	
15	2004-06-21 23:10:02	3.4	11	26	68	0.76	2	0.25	1		OK	
16	2004-02-23 17:31:21	4.5	20	55	97	0.68	2	0.01	1		OK	
17	2004-02-18 14:31:58	3.2	8	21	87	0.54	2	1.24	1		OK	
18	2003-03-22 13:36:15	3.9	17	46	60	0.68	3	0.06	1		OK	azimuthal gap $> 270°$
19	2002-01-18 11:14:54	3.4	3	9	82	0.82	9	0.80	1		uncert.	
20	2001-10-01 06:36:22	3.8	11	31	79	0.88	5	0.03	1		OK	OK
21	2001-07-09 22:50:02	3.1	5	11	80	0.79	3	1.21	1		OK	OK
22	2001-03-17 00:29:59	3.4	14	35	93	0.72	7	0.11	1		OK	OK
23	2000-06-10 05:51:02	3.4	9	21	88	0.62	2	0.43	1		OK	OK
24	2000-06-09 05:06:06	3.2	2	6	54	0.75	7	1.11	1		uncert.	unstable
25	2013-12-27 07:08:28	3.4	21	61	62	**0.29**	3	1.86	0		OK	fit decreased by distant stations

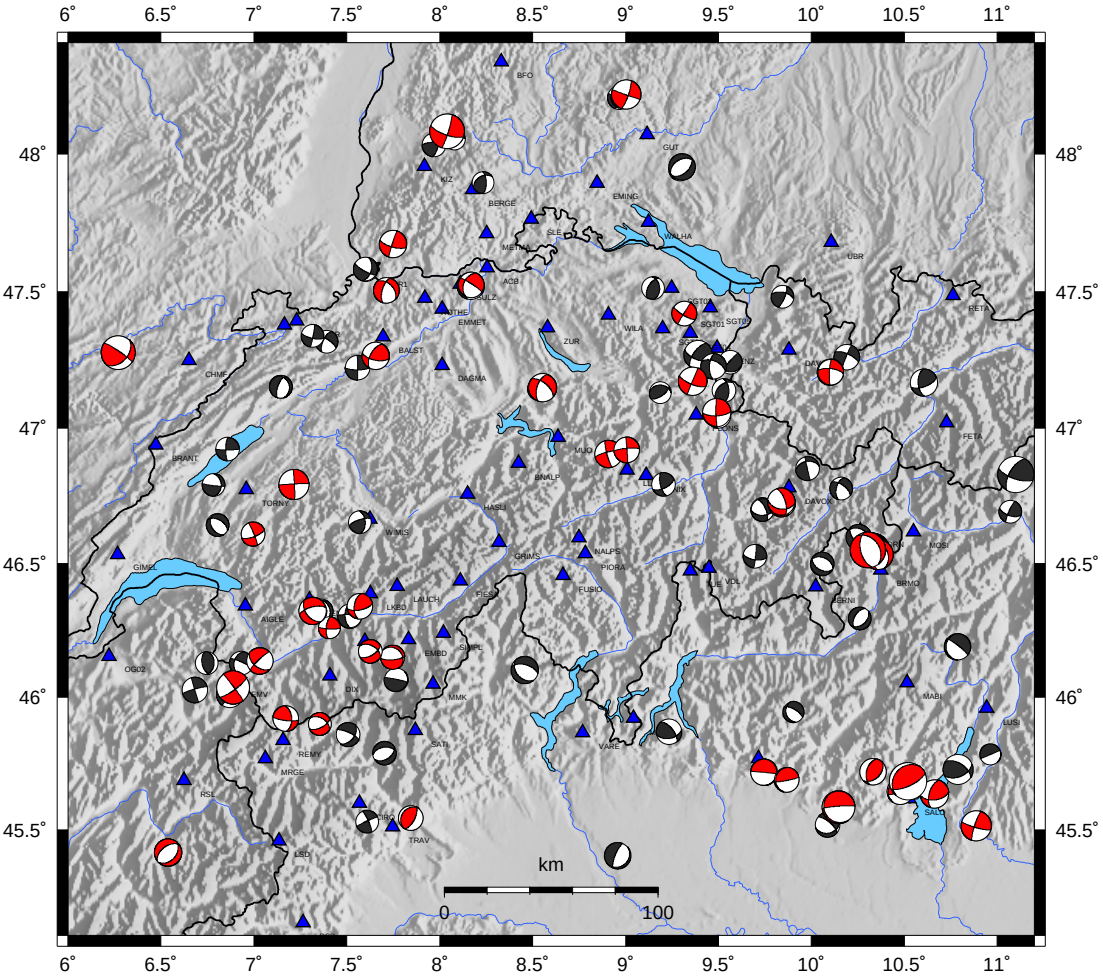

Figure 8.13: Map of all events with a CMT solution calculated by the proposed method. Events which passed the criterion (Eq. 8.1), i.e. "trusted events", are shown in red, the others in black. The stations available from the SED data archives at arclink.ethz.ch are shown by blue triangles. Note that only a specific subset of the stations was used in the inversion of each MT. Magnitudes are between 3.0–5.0, hypocenter depths are up to 35 km.

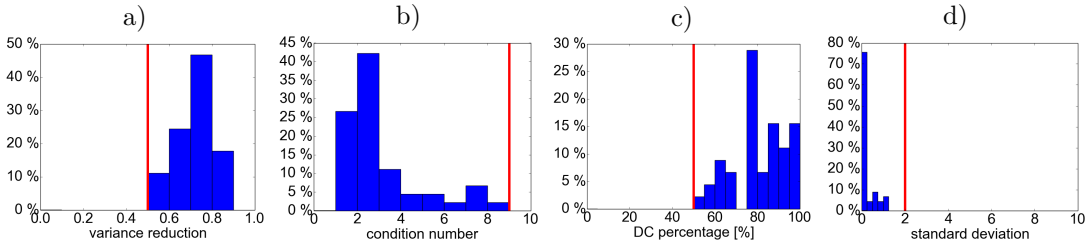

Figure 8.14: Statistics of quality measures for 45 earthauakes of Swiss earthquake catalogue whose focal mechanisms were newly obtained by the automatic processing and evaluated as reliable by the automated criterion (Eq. 8.1). Note reasonable reliability of the new solutions, expressed by their (a) high values of the variance reduction, (b) low condition number, (c) low DC percentage, and (d) low combined standard deviation of CMT parameters (see Eq. 8.1). The cut-of value of the criterion is shown by the red line.

9. Future directions

In this thesis we developed and tested a new method for fully automated CMT inversion. The method is programmed in Python and our code is freely available. For its applicability to wider range of seismic events and to make it more user-friendly, some extensions and new features, which were out of scope of this thesis, are welcomed. This further development does not need to be done by the author himself only, but can be done be other developers. The code is open source, so anyone can download the source code and modify it, and also to suggest to incorporate his modified version to the original one. The development is welcomed in the following areas.

- Our method assumes that the seismic noise is the main source of the uncertainty and the data covariance matrix reflect just the properties of before-event noise. For more general use, it would be useful to combine our approach (covariance matrix from the before-event noise covariance) with some other methods reflecting Green's function uncertainty, such as hierarchical error estimation [Bodin et al., 2012; Dettmer et al., 2012] or analytical calculation of the covariance matrix [Hallo and Gallovič, 2016].

- Now we solve the inverse problem of the seismic source in the point source approximation. This is correct approach for small events, where more details can be hardly detected, but for larger events, it would be useful to add a possibility of a more detailed description of the source, e.g. multi-point source approximation [Zahradník and Sokos, in press], possibly in a DC-constrained MT mode.

- Now we look for the solution in the CMT description. We intend to add more possibilities, e.g. shear-tensile source [Vavryčuk, 2011].

- Before the inversion, we test the presence of some instrument disturbances in the data. Now, we detect only one kind of disturbance which can be modeled as an instrument response to a spurious step in input acceleration. There are also similar disturbances which can be described as instrument response to a step in the input velocity [Zahradník and Plešinger, 2010], and also mixed disturbances. We plan to implement detection of these disturbances of the second type in the future, including diagnostics of a joint occurrence of both kinds, as well as detection of clipped records.

- The calculation of Green's functions may be also improved. Now, code Axitra [Bouchon, 1981; Coutant, 1989] is used. Because of its limitations (layered 1-D velocity model only), we plan to make easy use of other codes, includind 3-D, for this task. Definitely, the Green's function calculation should not be included in our code for CMT inversion, but just an interface for running third party codes and reading their outputs should be developed.

- We also want to incorporate the first-motion polarities in the inversion as an additional MT constraint.

Conclusion

This thesis is focused on development of a new, fully automated method for a centroid moment tensor (CMT) inversion. This task covers a wide range of topics, e.g. data selection and retrieval, disturbance detection, seismogram preparation and filtration, station weighting, solution of the inverse problem, uncertainty assessment, result plotting and output presentation etc.

In the beginning of the PhD work, we dealt with a closely related topic, a velocity model, which is a prerequisite for the CMT inversion [Vackář et al., 2014]. We studied how an existing model can be improved to explain the observed seismic waves including leaking modes. Than we focused on the main theme, with a special focus on data quality control, disturbance detection, and uncertainty assessment [Vackář et al., 2015, 2017]. We accented this topic because we wanted to have a robust method with reliable outputs. Therefore, the main results of the work are three papers [Vackář et al., 2014, 2015, 2017], a code for automated CMT inversion freely available at `http://geo.mff.cuni.cz/~vackar/isola-obspy/`, and this thesis.

Our newly developed method and code for the CMT inversion is innovative in the following aspects: (i) the CMT inversion is fully automated, no user interaction is required, although the details of the process can be visually inspected later, using many figures which are automatically plotted. (ii) The automated process includes detection of disturbances. The detection, although not including all types of disturbances, and further development is welcome, avoids most of problems which can cause misleading results. (iii) The data covariance matrix calculated from before-event noise is used. It works as an automated frequency filter and station weighting according to the noise level. (iv) Bayesian approach is used, so not only the best solution is obtained, but also the posterior probability density function. (v) A space-time grid search effectively combined with the least-squares inversion of moment tensor components speeds up the inversion and allows to visually inspect solution variability over the grid.

Some of these features were used by other authors, but the combination of them is novel. To the best of our knowledge, automated MT solution using a Bayesian approach was published just by Stähler and Sigloch [2014] for teleseismic events. The combination of an analytical solution for the MT components with a spatial-temporal grid-searching was suggested by the same authors, but we do not know any other study using it in practice. We did not find also any other Bayesian method eliminating disturbances in seismograms, although hierarchical weights [Dettmer et al., 2014] could overcome this issue. Other works using Bayesian inversion of MT or CMT, which are not automated, include Duputel et al. [2012a], Mustać and Tkalčić [2016], and Wéber [2006]. We differ not only in automation and analytical determination of MT components, but also in construction of the data covariance matrix using a non-parametric approach.

We have demonstrated usefulness of the data covariance matrix in terms of automatically identifying a set of stations and frequency ranges most suitable for the waveform inversion. In this sense, our new method is more efficient than various existing procedures in which the inversion is repeatedly performed in different frequency ranges, either manually, or automatically (as an example of the latter,

see Frequency range tests in Dias et al. [2016]). Our proposed approach seems to be useful for weak events and records with low signal-to-noise ratio, where the seismic noise is a dominant source of errors. It is important to keep in mind, that such uncertainties correspond just to noise in data, and do not reflect the errors in Green's functions or any other sources of errors. So the obtained uncertainties are usually underestimated in real cases. For more general use, it would be useful to combine our approach (covariance matrix from before-event noise covariance) with some other methods reflecting Green's function uncertainty.

The automated procedure has been tested by comparison with manually processed moment tensors of all events greater than M$\geq$3 in the Swiss catalogue over 16 years using data available at the Swiss data center at arclink.ethz.ch. The quality of the results of the presented automated process is comparable with careful manual processing of data.

Bibliography

Bernardi, F., J. Braunmiller, U. Kradolfer, and D. Giardini (2004). Automatic regional moment tensor inversion in the European-Mediterranean region. *Geophys. J. Int.* **157** (2), 703–716.

Beyreuther, M., R. Barsch, L. Krischer, T. Megies, Y. Behr, and J. Wassermann (2010). ObsPy: A Python toolbox for seismology. *Seismol. Res. Lett.* **81**, 530–533.

Bodin, T., M. Sambridge, H. Tkalčić, P. Arroucau, K. Gallagher, and N. Rawlinson (2012). Transdimensional inversion of receiver functions and surface wave dispersion. *J. Geophys. Res. Solid Earth* **117** (B2).

Boore, D. M. (2003). Analog-to-digital conversion as a source of drifts in displacements derived from digital recordings of ground acceleration. *Bull. Seism. Soc. Am.* **93**, 2017–2024.

Boore, D. M., C. D. Stephens, and W. B. Joyner (2002). Comments on baseline correction of digital strong-motion data: Examples from the 1999 Hector Mine, California, earthquake. *Bull. Seism. Soc. Am.* **92** (4), 1543–1560.

New manual of seismological observatory practice (NMSOP-2) (2012). In: *IASPEI, GFZ German Research Centre for Geosciences, Potsdam*. Ed. by P. Bormann. doi: 10.2312/GFZ.NMSOP-2.

Bouchon, M. (1981). A simple method to calculate Green's function for elastic layered media. *Bull. Seism. Soc. Am.* **64** (1), 93–107.

Bouchon, M. and K. Ali (1977). Discrete wave number representation of seismic source wave fields. *Bull. Seism. Soc. Am.* **67**, 259–277.

Braunmiller, J., U. Kradolfer, M. Baer, and D. Giardini (2002). Regional moment tensor determination in the European-Mediterranean area – initial results. *Tectonophysics* **356**, 5–22.

Brokešová, J. and J. Málek (2010). New portable sensor system for rotational seismic motion measurements. *Review of Scientific Instruments* **81** (8), 084501.

Brokešová, J. (2008). Teoretické základy Fourierovy spektrální analýzy [Theoretical basis of Fourier spectral analysis]. Available at `http://geo.mff.cuni.cz/vyuka/Brokesova-FourierovaSpektralniAnalyza.pdf`.

Cauzzi, C., B. Edwards, D. Fäh, J. Clinton, S. Wiemer, P. Kästli, G. Cua, and D. Giardini (2014). New predictive equations and site amplification estimates for the next-generation Swiss ShakeMaps. *Geophys. J. Int.* **200** (1), 421–438.

Cesca, S., S. Heimann, K. Stammler, and T. Dahm (2010). Automated procedure for point and kinematic source inversion at regional distances. *J. Geophys. Res. Solid Earth* **115** (B6).

Cholesky, A.-L. (1910). Sur la résolution numérique des systèmes d'équations linéaires. Online and analyzed on BibNum (in French) (in English—for English, click 'A télécharger'). URL: `http://bibnum.education.fr/mathematiques/algebre/sur-la-resolution-numerique-des-systemes-d-equations-lineaires` (visited on 04/19/2018).

Coutant, O. (1989). Program of numerical simulation AXITRA. *Res. Rep. LGIT (in French), Universite Joseph Fourier, Grenoble.*

Dainty, A. M. (1971). Leaking modes in a crust with a surface layer. *Bull. Seism. Soc. Am.* **64** (1), 93–107.

Delorey, A. A., J. Vidale, J. Steim, and P. Bodin (2008). Broadband sensor nonlinearity during moderate shaking. *Bull. Seism. Soc. Am.* **98**, 1595–1601.

Dettmer, J., S. Dosso, and C. Holland (2007). Uncertainty estimation in seismo-acoustic reflection travel-time inversion. *J. acoust. Soc. Am.* **122**, 161–176.

Dettmer, J., S. Molnar, G. Steininger, S. Dosso, and J. Cassidy (2012). Trans-dimensional inversion of microtremor array dispersion data with hierarchical autoregressive error models. *Geophys. J. Int.* **188** (2), 719–734.

Dettmer, J., R. Benavente, P. R. Cummins, and M. Sambridge (2014). Trans-dimensional finite-fault inversion. *Geophys. J. Int.* **199** (2), 735–751.

Dias, F., J. Zahradník, and M. Assumpção (2016). Path-specific, dispersion-based velocity models and moment tensors of moderate events recorded at few distant stations: Examples from Brazil and Greece. *J. South Amer. Earth Sci.* **71**, 344–358.

Diehl, T., E. Kissling, S. Husen, and F. Aldersons (2009). Consistent phase picking for regional tomography models: application to the greater Alpine region. *Geophys. J. Int.* **176**, 542–554.

Dreger, D. S. (2003). TDMT_INV: Time domain seismic moment tensor inversion. In: *International Geophysics*. Vol. 81. Elsevier, 1627.

Duputel, Z., L. Rivera, Y. Fukahata, and H. Kanamori (2012a). Uncertainty estimations for seismic source inversions. *Geophys. J. Int.* **190** (2), 1243–1256.

Duputel, Z., L. Rivera, H. Kanamori, and G. Hayes (2012b). W phase source inversion for moderate to large earthquakes (1990–2010). *Geophys. J. Int.* **189** (2), 1125–1147.

E., F. and D. D. S. (2000). Performance test of an automated moment tensor determination system for the future "Tokai" earthquake. *Earth Planets Space* **52**, 383–392.

Edwards, B. and D. Fäh (2013). A stochastic ground-motion model for Switzerland. *Bull. Seism. Soc. Am.* **103**, 78–98.

Ekström, G., M. Nettles, and A. Dziewoński (2012). The global CMT project 2004–2010: Centroid-moment tensors for 13,017 earthquakes. *Phys. Earth Planet. In.* **200-201**, 1–9. issn: 0031-9201.

Fujita, M. and K. Nishimura (1993). Estimation of crustal structure in central and west Japan from waveform modeling of regional *PL* waves. *Pure appl. Geophys.* **140**, 569–592.

Gilbert, F. (1964). Propagation of transient leaking modes in a stratified elastic waveguide. *Rev. Geophys.* **2**, 123–153.

Graizer, V. (2010). Strong motion recordings and residual displacements: What are we actually recording in strong motion seismology? *Seismol. Res. Lett.* **81**, 635–639.

Haddon, R. A. W. (1984). Computation of synthetic seismograms in layered earth models using leaking modes. *Bull. Seism. Soc. Am.* **74** (4), 1225–1248.

Halbert, S. (2012). SEED Reference Manual (Standard for the Exchange of Earthquake Data), SEED Format Version 2.4, Appendix A: Channel Naming. url: http://www.fdsn.org/seed_manual/SEEDManual_V2.4_Appendix-A.pdf (visited on 03/09/2018).

Hallo, M. and F. Gallovič (2016). Fast and cheap approximation of Green function uncertainty for waveform-based earthquake source inversions. *Geophys. J. Int.* **207** (2), 1012–1029.

Hanka, W., J. Saul, B. Weber, J. Becker, P. Harjadi, Fauzi, and G. S. Group (2010). Real-time earthquake monitoring for tsunami warning in the Indian Ocean and beyond. *Natural Hazards and Earth System Sciences (NHESS)* **10** (12), 2611–2622.

Hazewinkel, M., ed. (2001). Cholesky factorization, Encyclopedia of Mathematics. url: http://www.encyclopediaofmath.org/index.php?title=Cholesky_factorization&oldid=37467 (visited on 04/19/2018).

Helmberger, D. V. and G. R. Engen (1980). Modeling the long-period body waves from shallow earthquakes at regional ranges. *Bull. Seism. Soc. Am.* **70**, 1699–1714.

Herrmann, R. B. (2004). Modal summation, Computer Programs in Seismology, version 3.30. url: http://www.eas.slu.edu/eqc/eqccps.html.

Holt, W. and T. Wallace (1990). Crustal thickness and upper mantle velocities in the Tibetan Plateau region from the inversion of regional Pnl waveforms: Evidence for a thick upper mantle lid beneath southern Tibet. *J. Geophys. Res. Solid Earth* **95** (B8), 12499–12525.

Hunter, J. D. (2007). Matplotlib: A 2D graphics environment. *Computing in Science and Engineering* **9**, 90–95.

Iwan, W. D., M. A. Moser, and C. Y. Peng (1985). Some observations on strong-motion earthquake measurement using a digital accelerograph. *Bull. Seism. Soc. Am.* **75**, 1225–1246.

Javelaud, E. H., T. Ohmachi, and S. Inoue (2011). A quantitative approach for estimating coseismic displacements in the near field from strong-motion accelerographs. *Bull. Seism. Soc. Am.* **101**, 1182–1198.

Javelaud, E. H., T. Ohmachi, and S. Inoue (2012). Estimating small permanent rotation from strong-motion records: What is comparison with external measurements telling us? *Bull. Seism. Soc. Am.* **102**, 2257–2263.

Jian, P.-R., T.-L. Tseng, W.-T. Liang, and P.-H. Huang (2018). A new automatic full-waveform regional moment tensor inversion algorithm and its applications in the Taiwan area. *Bull. Seism. Soc. Am.* **108** (2), 573–587.

Kagan, Y. Y. (1991). 3-D rotation of double-couple earthquake sources. *Geophys. J. Int.* **106** (3), 709–716.

Kanamori, H. (1993). W phase. *Geophys. Res. Lett.* **20** (16), 1691–1694.

Kanamori, H. and L. Rivera (2008). Source inversion of W phase: speeding up seismic tsunami warning. *Geophys. J. Int.* **175**, 222–238.

Karagianni, E. E., C. B. Papazachos, D. G. Panagiotopoulos, P. Suhadolc, A. Vuan, and G. F. Panza (2005). Shear velocity structure in the Aegean area obtained by inversion of Rayleigh waves. *Geophys. J. Int.* **160**, 127–143.

Käufl, P., A. Valentine, R. de Wit, and J. Trampert (2015). Robust and fast probabilistic source parameter estimation from near-field displacement

waveforms using pattern recognition. *Bull. Seism. Soc. Am.* **105** (4), 2299–2312.

Kolínský, P. (2004). Surface waves dispersion curves of Eurasian earthquakes: the SVAL program. *Acta Geodyn. Geomater.* **1** (2), 165–185.

Krischer, L., T. Megies, R. Barsch, M. Beyreuther, T. Lecocq, C. Caudron, and J. Wassermann (2015). ObsPy: a bridge for seismology into the scientific Python ecosystem. *Computational Science and Discovery* **8** (1).

Křížová, D., J. Zahradník, and A. Kiratzi (2013). Resolvability of isotropic component in regional seismic moment tensor inversion. *Bull. Seism. Soc. Am.* **103** (4), 2460–2473.

Latorre, D., J. Virieux, T. Monfret, V. Monteiller, T. Vanorio, J.-L. Got, and H. Lyon-Caen (2004). A new seismic tomography of Aigion area (Gulf of Corinth, Greece) from the 1991 data set. *Geophys. J. Int.* **159**, 1013–1031.

Lee, E.-J., P. Chen, T. H. Jordan, and L. Wang (2011). Rapid full-wave centroid moment tensor (CMT) inversion in a three-dimensional earth structure model for earthquakes in Southern California. *Geophys. J. Int.* **186** (1), 311–330.

Lee, S.-J., W.-T. Liang, H.-W. Cheng, F.-S. Tu, K.-F. Ma, H. Tsuruoka, H. Kawakatsu, B.-S. Huang, and C.-C. Liu (2013). Towards real-time regional earthquake simulation I: real-time moment tensor monitoring (RMT) for regional events in Taiwan. *Geophys. J. Int.* **196** (1), 432–446.

Liu, Q., J. Polet, D. Komatitsch, and J. Tromp (2004). Spectral-element moment tensor inversions for earthquakes in southern California. *Bull. Seism. Soc. Am.* **94**, 1748–1761.

Minson, S., M. Simons, and J. Beck (2013). Bayesian inversion for finite fault earthquake source models I—theory and algorithm. *Geophys. J. Int.* **194**, 1701–1726.

Mustać, M. and H. Tkalčić (2016). Point source moment tensor inversion through a Bayesian hierarchical model. *Geophys. J. Int.* **204** (1), 311–323.

Málek, J., J. Brokešová, and J. Vackář (2017). Mid-European seismic attenuation anomaly. *Tectonophysics* **712**, 557–577.

Nakano, M, H Kumagai, and H Inoue (2008). Waveform inversion in the frequency domain for the simultaneous determination of earthquake source mechanism and moment function. *Geophys. J. Int.* **173** (3), 1000–1011.

Novotný, O., J. Zahradník, and G.-A. Tselentis (2001). Northwestern Turkey earthquakes and the crustal structure inferred from surface waves observed in western Greece. *Bull. Seism. Soc. Am.* **91** (4), 875–879.

Novotný, O., J. Janský, V. Plicka, and H. Lyon-Caen (2008). A layered model of the upper crust in the Aigion region of Greece, inferred from arrival times of the 2001 earthquake sequence. *Stud. Geophys. Geod.* **52**, 123–131.

Novotný, O., E. Sokos, and V. Plicka (2012). Upper crustal structure of the western Corinth gulf, Greece, inferred from arrival times of the January 2010 earthquake sequence. *Stud. Geophys. Geod.* **56**, 1007–1018.

Novotný, O., J. Vackář, and E. Sokos (2015). Dispersion of Love waves from the 2010 Efpalio earthquake in the Corinth Gulf region, Greece. *J. Seismolog.* **19**, 801–806.

Oliver, J. and M. Major (1960). Leaking modes and the PL phase. *Bull. Seism. Soc. Am.* **50** (2), 165–180.

Patton, H. J. and D. I. Doser (1988). Inversion of regional Pnl and surface-wave data for source parameters of a Borah Peak aftershock. *Geophys. Res. Lett.* **15** (5), 459–462.

Phinney, R. (1961). Propagation of leaking interface waves. *Bull. Seism. Soc. Am.* **51** (4), 527–555.

Pillet, R. and J. Virieux (2007). The effects of seismic rotations on inertial sensors. *Geophys. J. Int.* **171**, 1314–1323.

Pondrelli, S., A. Morelli, G. Ekström, S. Mazza, E. Boschi, and A. M. Dziewonski (2002). European–Mediterranean regional centroid-moment tensors: 1997–2000. *Phys. Earth Planet. In.* **130** (1), 71–101.

Rigo, A., H. Lyon-Caen, R. Armijo, A. Deschamps, D. Hatzfeld, K. Makropoulos, P. Papadimitriou, and I. Kassaras (1996). A microseismic study in the western part of the Gulf of Corinth (Greece): implications for large scale normal faulting mechanisms. *Geophys. J. Int.* **126**, 663–688.

Rueda, J. and J. Mézcua (2005). Near-real-time seismic moment-tensor determination in Spain. *Seismol. Res. Lett.* **76**, 455–465.

Saikia, C. K. and L. J. Burdick (1991). Fine structure of P nl waves from explosions. *J. Geophys. Res. Solid Earth* **96** (B9), 14383–14401.

Sambridge, M. (1999). Geophysical inversion with a neighbourhood algorithm – I. Searching a parameter space. *Geophys. J. Int.* **138** (2), 479–494.

Sambridge, M. (2014). A Parallel Tempering algorithm for probabilistic sampling and multimodal optimization. *Geophys. J. Int.* **196**, 357–374.

Sambridge, M. and K. Mosegaard (2002). Monte Carlo methods in geophysical inverse problems. *Rev. Geophys.* **40** (3), 1009.

Savage, B. and D. V. Helmberger (2004). Site response from incident *Pnl* waves. *Bull. Seism. Soc. Am.* **94** (1), 357–362.

Scognamiglio, L., E. Tinti, and A. Michelini (2009). Real-time determination of seismic moment tensor for the Italian region. *Bull. Seism. Soc. Am.* **99**, 2223–2242.

SeisComP3.org. SeisComP3 documentation. url: `https://www.seiscomp3.org/wiki/doc/applications/arclink` (visited on 01/24/2017).

Shakal, A. F. and C. D. Petersen (2001). Acceleration offsets in some FBA's during earthquake shaking (abstract). *Seismol. Res. Lett.* **72**, 233.

Shaw, P. and J. Orcutt (1984). Propagation of PL and implications for the structure of Tibet. *J. Geophys. Res. Solid Earth* **89**, 3135–3152.

Silver, P. G. and T. H. Jordan (1982). Optimal estimation of scalar seismic moment. *Geophys. J. Int.* **70** (3), 755–787.

Sokos, E. and J. Zahradník (2008). ISOLA a Fortran code and a Matlab GUI to perform multiple-point source inversion of seismic data. *Computers and Geosciences* **34**, 967–977.

Sokos, E. and J. Zahradník (2013). Evaluating centroid-moment-tensor uncertainty in the new version of ISOLA software. *Seismol. Res. Lett.* **84**, 656–665.

Sokos, E., J. Zahradník, J. J. A. Kiratzi and, F. Gallovič, O. Novotný, J. Kostelecký, A. Serpetsidaki, and G.-A. Tselentis (2012). The Jan-

uary 2010 Efpalio earthquake sequence in the western Corinth Gulf (Greece). *Tectonophysics* **530**, 299–309.

Somerville, P., K. Irikura, R. Graves, S. Sawada, D. Wald, N. Abrahamson, Y. Iwasaki, T. Kagawa, N. Smith, and A. Kowada (1999). Characterizing crustal earthquake slip models for the prediction of strong ground motion. *Seismol. Res. Lett.* **70** (1), 59–80.

Stähler, S. and K. Sigloch (2014). Fully probabilistic seismic source inversion-Part 1: Efficient parameterisation. *Solid Earth* **5** (2), 1055–1069.

Stähler, S. and K. Sigloch (2016). Fully probabilistic seismic source inversion-Part 2: Modelling errors and station covariances. *Solid Earth* **7** (6), 1521–1536.

Su, S. and J. Dorman (1965). The use of leaking modes in seismogram interpretation and in studies of crust-mantle structure. *Bull. Seism. Soc. Am.* **55** (6), 989–1021.

Swiss Seismological Service (SED) at ETH Zurich (1983). National Seismic Networks of Switzerland; ETH Zürich. Other/Seismic Network. doi: 10.12686/sed/networks/ch.

Šílený, J. (1998). Earthquake source parameters and their confidence regions by a genetic algorithm with a 'memory'. *Geophys. J. Int.* **134** (1), 228–242.

Tan, Y., A. Song, S. Wei, and D. Helmberger (2010). Surface wave path corrections and source inversions in southern California. *Bull. Seism. Soc. Am.* **100** (6), 2891–2904.

Tarantola, A. (2005). Inverse problem theory and methods for model parameter estimation. siam.

Tichelaar, B. and L. Ruff (1989). How good are our best models? Jackknifing, bootstrapping, and earthquake depth. *Eos, Transactions American Geophysical Union* **70** (20), 593–606.

Triantafyllis, N., E. Sokos, A. Ilias, and J. Zahradník (2016). SCISOLA: automatic Moment Tensor solution for Seiscomp3. *Seismol. Res. Lett.* **87** (1), 157–163.

Vackář, J., J. Zahradník, and E. Sokos (2014). Strong fast long-period waves in the Efpalio 2010 earthquake records: explanation in terms of leaking modes. *J. Seismolog.* **18**, 81–91.

Vackář, J., J. Burjánek, and J. Zahradník (2015). Automated detection of long-period disturbances in seismic records; MouseTrap code. *Seismol. Res. Lett.* **86**, 442–450.

Vackář, J., J. Burjánek, F. Gallovič, J. Zahradník, and J. Clinton (2017). Bayesian ISOLA: new tool for automated centroid moment tensor inversion. *Geophys. J. Int.* **210** (2), 693–705.

Vallée, M., J. Charléty, A. M. G. Ferreira, B. Delouis, and J. Vergoz (2011). SCARDEC: a new technique for the rapid determination of seismic moment magnitude, focal mechanism and source time functions for large earthquakes using body-wave deconvolution. *Geophys. J. Int.* **184** (1), 338–358.

Vavryčuk, V. (2011). Tensile earthquakes: Theory, modeling, and inversion. *J. Geophys. Res. Solid Earth* **116** (B12).

Vavryčuk, V. (2015). Moment tensor decompositions revisited. *J. Seismolog.* **19** (1), 231–252.

Vecsey, L., J. Plomerová, P. Jedlička, and V. Babuška (2017). Significance of data-quality control in passive seismic experiments exemplified on CZ broad-band seismic pool MOBNET in the AlpArray collaborative project. In: *EGU General Assembly 19*. Vienna, Austria.

Wéber, Z. (2006). Probabilistic local waveform inversion for moment tensor and hypocentral location. *Geophys. J. Int.* **165** (2), 607–621.

Wielandt, E. and T. Forbriger (1999). Near-field seismic displacement and tilt associated with the explosive activity of Stromboli. *Ann. di Geofis.* **42**, 407–416.

Wiens, D. A., S. H. Pozgay, P. J. Shore, A. W. Sauter, and R. A. White (2005). Tilt recorded by a portable broadband seismograph: The 2003 eruption of Anatahan Volcano, Mariana Islands. *Geophys. Res. Lett.* **32**, L18305.

Wikipedia contributors (2018). Gaussian integral — Wikipedia, The Free Encyclopedia. url: `https://en.wikipedia.org/w/index.php?title=Gaussian_integral&oldid=834139068` (visited on 05/04/2018).

Zahradník, J. and S. Custódio (2012). Moment tensor resolvability: application to Southwest Iberia. *Bull. Seism. Soc. Am.* **102** (3), 1235–1254.

Zahradník, J. and A. Plešinger (2005). Long-period pulses in broadband records of near earthquakes. *Bull. Seism. Soc. Am.* **95**, 1928–1939.

Zahradník, J. and A. Plešinger (2010). Toward understanding subtle instrumentation effects associated with weak seismic events in the near field. *Bull. Seism. Soc. Am.* **100**, 59–73.

Zahradník, J., J. Janský, and V. Plicka (2008). Detailed waveform inversion for moment tensors of M∼4 events; examples from the Corinth Gulf, Greece. *Bull. Seism. Soc. Am.* **98**, 2756–2771.

Zahradník, J. and E. Sokos (in press). ISOLA code for multiple-point source modeling. In: *Moment Tensor Solutions—A Useful Tool for Seismotectonics*. Ed. by S. D'Amico. Springer. url: `http://geo.mff.cuni.cz/~jz/papers/ISOLA_bookchapter.pdf`.

List of Figures

List of Tables

List of Abbreviations

2-D two-dimensional

3-D three-dimensional

CLVD Compensated Linear Vector Dipole

CMT Centroid Moment Tensor

CN Condition Number

DC Double Couple

DFT Discrete Fourier Transformation

DWN Discrete Wave-Number

FFT Fast Fourier Transformation

GPS Global Position System

GUI Graphic User Interface

HTML HyperText Markup Language

ISO Isotropic (component of MT)

LSQ Least-Squares Method

MT Moment Tensor

PGA Peak-Ground Acceleration

PGD Peak-Ground Displacement

PGV Peak-Ground Velocity

PPD Posterior Probability Density

PPDF Posterior Probability Density Function

SED Swiss Seismological Service

STF Source Time Function

VR Variance Reduction

List of Publications

Here we list all publications where the author of this thesis is a coauthor.

Three of them, Vackář et al. [2014, 2015, 2017], are focused on the field of the PhD study of the main author. The first one [Vackář et al., 2014] is reprinted as Chapter 2. The second one [Vackář et al., 2015] is included as Chapter 5. The most recent one [Vackář et al., 2017] covers most of topics of the thesis, so it is split into corresponding chapters, creating main parts of Chapters 3, 6, and 8. These chapters include not only the text published in the paper, but they are extended also by some additional texts, derivations, formulas, and tests.

J. Vackář, J. Zahradník, and E. Sokos [2014]. Strong fast long-period waves in the Efpalio 2010 earthquake records: explanation in terms of leaking modes. *J. Seismolog.* **18**, 81–91

O. Novotný, J. Vackář, and E. Sokos [2015]. Dispersion of Love waves from the 2010 Efpalio earthquake in the Corinth Gulf region, Greece. *J. Seismolog.* **19**, 801–806

J. Vackář, J. Burjánek, and J. Zahradník [2015]. Automated detection of long-period disturbances in seismic records; MouseTrap code. *Seismol. Res. Lett.* **86**, 442–450

J. Vackář, J. Burjánek, F. Gallovič, J. Zahradník, and J. Clinton [2017]. Bayesian ISOLA: new tool for automated centroid moment tensor inversion. *Geophys. J. Int.* **210** [2], 693–705

J. Málek, J. Brokešová, and J. Vackář [2017]. Mid-European seismic attenuation anomaly. *Tectonophysics* **712**, 557–577

A. Attachment

A.1 Automatically generated HTML report

This attachment shows automatically generated output for a real case inversion: Sargans (CH) $M_W = 3.7$ earthquake. This earthquake is an aftershock of $M_W = 4.1$ mainshock with almost the same mechanism.

Sargans (CH) M_W = 3.7 earthquake

Web version of this auto-generated report

Auto-generated CMT catalog for Swiss earthquakes

Method: Waveform inversion for **deviatoric part of** moment tensor (5 components) with the **data covariance matrix** based on real noise with **crosscovariance** between components.

Hypocenter location

Agency:	Swiss Seismological Service
Origin time:	2013-12-27 07:08:28
Latitude:	47.058° N
Longitude:	9.496° E
Depth:	6.2 km
Magnitude:	3.7

Results

Centroid location

	absolute	relative
Time	2013-12-27 07:08:28	0.30 s after origin time
Latitude	47.076° N	2000 m north of the epicenter
Longitude	9.509° E	1000 m east of the epicenter
Depth	6.2 km	0.0 km deeper than location

Moment tensor and its quality

Centroid position	
depth	6.2 km
Seismic moment	
scalar seismic moment M_0	1.35e+14 Nm
moment magnitude M_w	3.4
Moment tensor components	
M_{rr}	0.36 * 1e+14
$M_{\theta\theta}$	0.01 * 1e+14
$M_{\phi\phi}$	-0.37 * 1e+14
$M_{r\theta}$	0.06 * 1e+14
$M_{r\phi}$	-0.45 * 1e+14
$M_{\theta\phi}$	-1.10 * 1e+14
Moment tensor decomposition	
DC	62 %
CLVD	-38 %
strike	83 / 178
dip	64 / 80
rake	168 / 26
Quality measures	
condition number	3
variance reduction	29 %
VR (6 closest components)	62 %

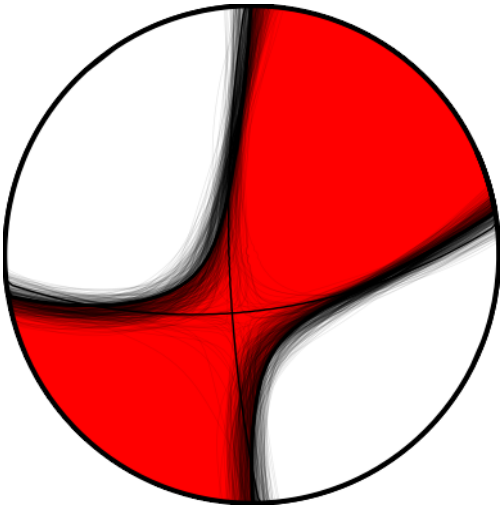

moment tensor
best solution and uncertainty

Histograms—uncertainty of MT parameters

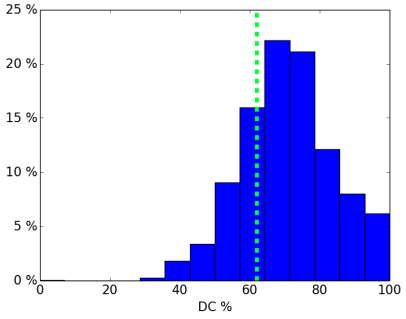

DC-part

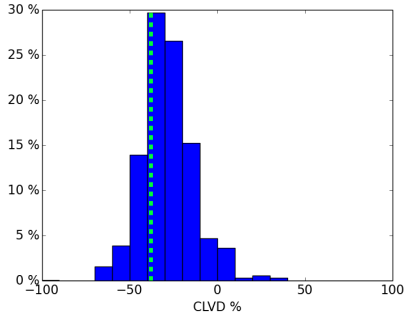

CLVD-part

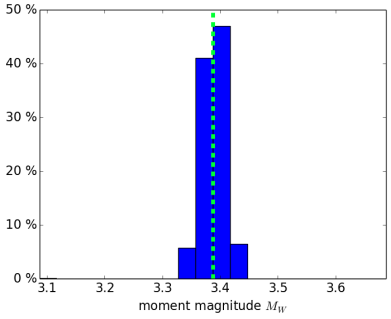

moment magnitude

Histograms—uncertainty of centroid position and time

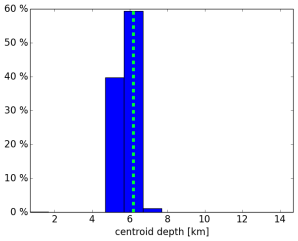

centroid depth

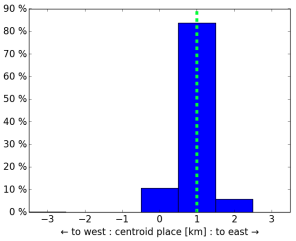

position east-west

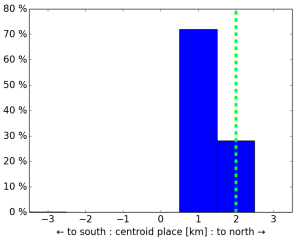

position north-south

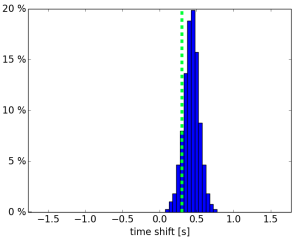

centroid time

Data used

Components used in inversion and their weights

station		component			distance *	azimuth	fmin	fmax
code	channel	Z	N	E	(km)	(deg)	(Hz)	(Hz)
CH:PLONS	HH	1.0	1.0	1.0	9	-96	0.02	0.15
CH:LIENZ	HH	1.0	1.0	1.0	26	-0	0.02	0.15
CH:SGT04	HH	1.0	1.0	1.0	34	-19	0.02	0.15
OE:DAVA	HH	1.0	1.0	1.0	39	49	0.02	0.15
CH:PANIX	HH	1.0	1.0	1.0	39	-131	0.02	0.15
CH:SGT03	HH	1.0	1.0	1.0	41	-33	0.02	0.15
CH:DAVOX	HH	1.0	1.0	1.0	42	136	0.02	0.15
CH:SGT05	HH	1.0	1.0	1.0	43	-4	0.02	0.15
CH:SGT01	HH	1.0	1.0	1.0	44	-18	0.02	0.15
CH:LLS	HH	1.0	1.0	1.0	44	-122	0.02	0.15
CH:SGT02	HH	1.0	1.0	1.0	54	-20	0.02	0.15
CH:WILA	HH	1.0	1.0	1.0	60	-48	0.02	0.15
CH:VDL	HH	1.0	1.0	1.0	64	-177	0.02	0.15
CH:MUO	HH	1.0	1.0	1.0	66	-98	0.02	0.15
MN:TUE	HH	1.0	1.0	1.0	66	-170	0.02	0.15
CH:FUORN	HH	1.0	1.0	1.0	76	129	0.02	0.15
CH:NALPS	HH	---	---	1.0	77	-132	0.02	0.15
CH:ZUR	HH	1.0	1.0	1.0	77	-63	0.02	0.15
CH:BERNI	HH	1.0	1.0	1.0	82	150	0.02	0.15
CH:WALHA	HH	1.0	1.0	1.0	82	-20	0.02	0.15
GR:UBR	HH	1.0	1.0	1.0	83	34	0.02	0.15

Mouse detection

NALPS HHZ: MOUSE detected, ignoring component in inversion (time of onset: 22.3 s, amplitude: 4.51e-07 m s^-2, fit: 0.93)
NALPS HHN: MOUSE detected, ignoring component in inversion (time of onset: 17.0 s, amplitude: 2.38e-07 m s^-2, fit: 0.94)

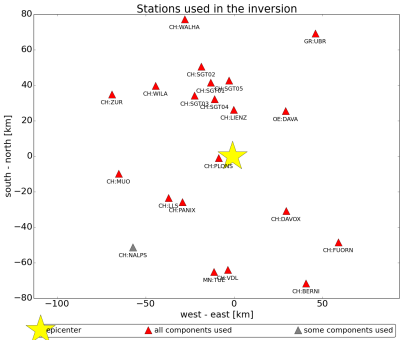

stations used

Data source

Network info: rzseddb.ethz.ch
Loading data from ArcLink server. host: arclink.ethz.ch

Noise and data covariance matrix

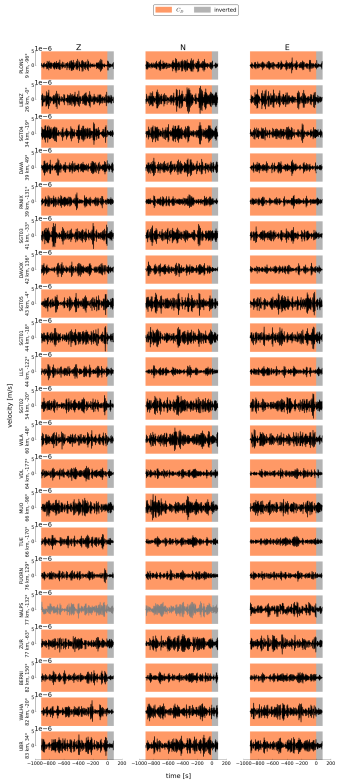

before-event noise

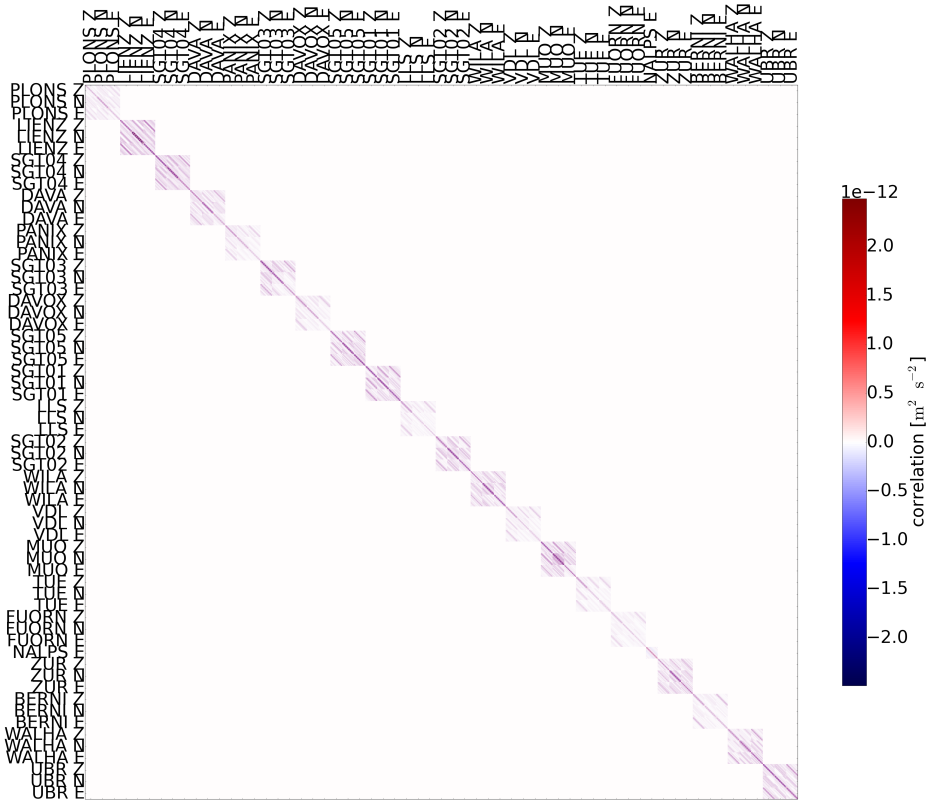

data covariance matrix

Waveforms

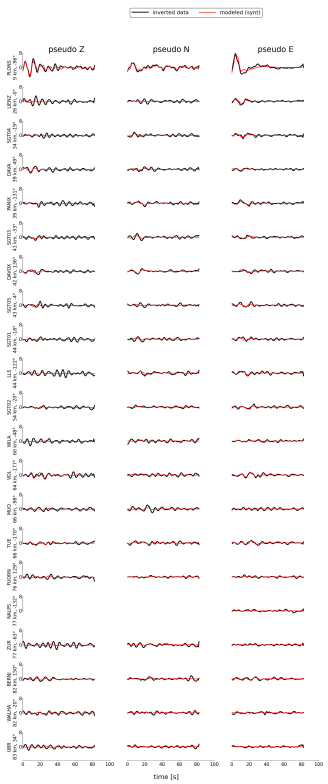

waveform fit
(filtered, normalized residua)

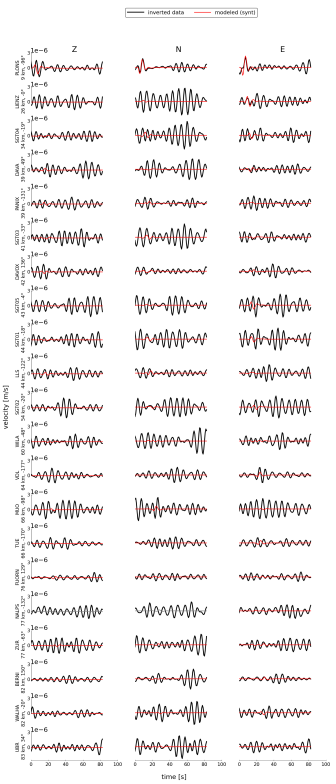

waveform fit
(non-filtered)

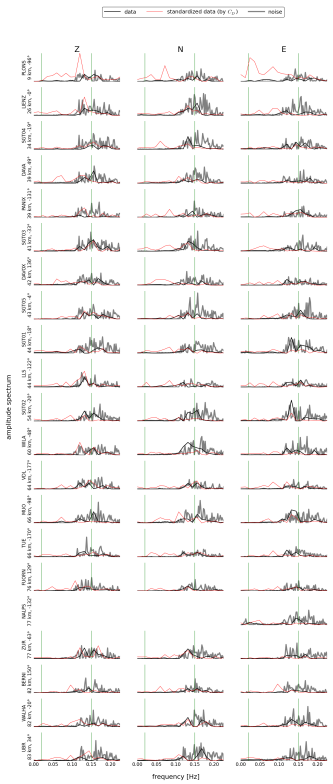

waveform spectra

Stability and uncertainty of the solution

Posterior probability density function (PPD)

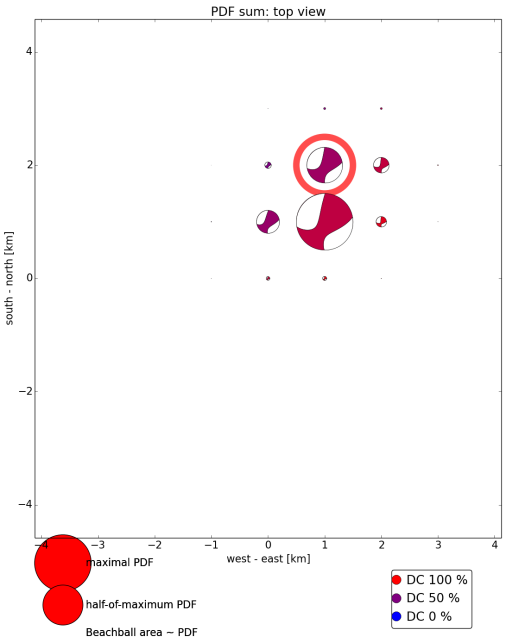

PPD: top view

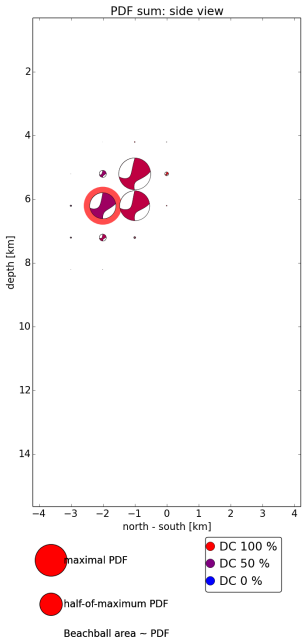

PPD: north-south view

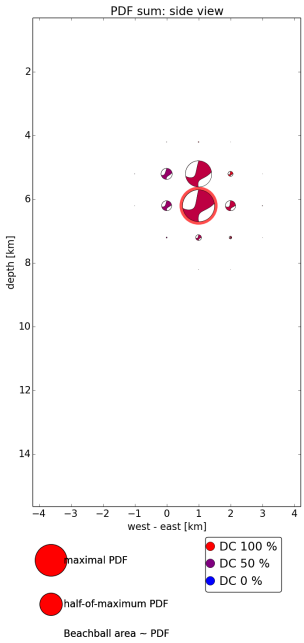

PPD: west-east view

Stability in space (side view)

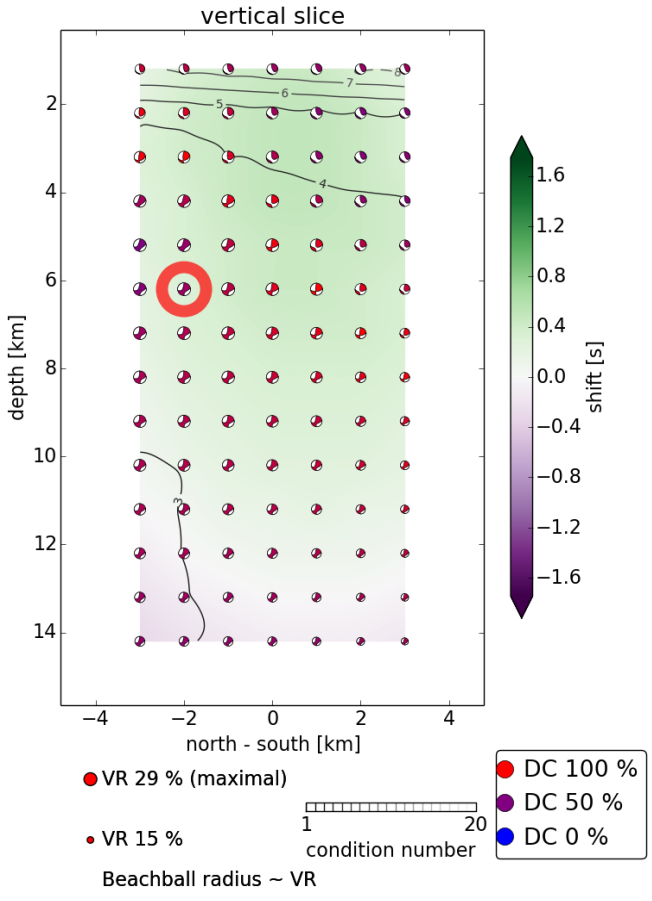

view from the east

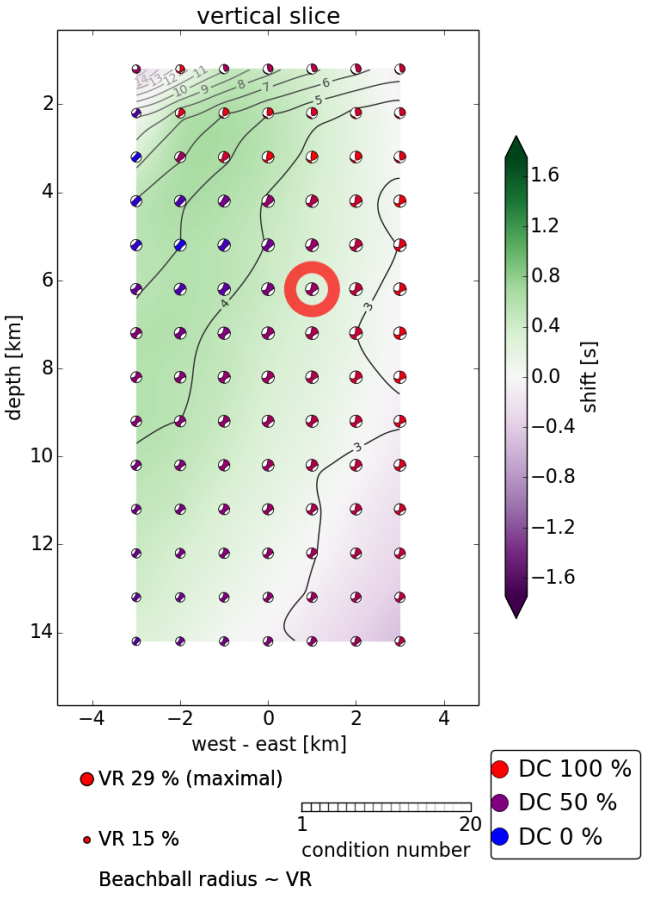

view from the south

Stability in space (top view)

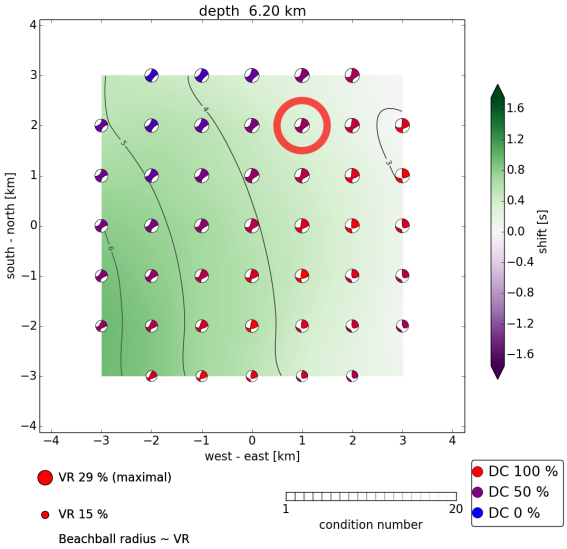

depth 6.2 km

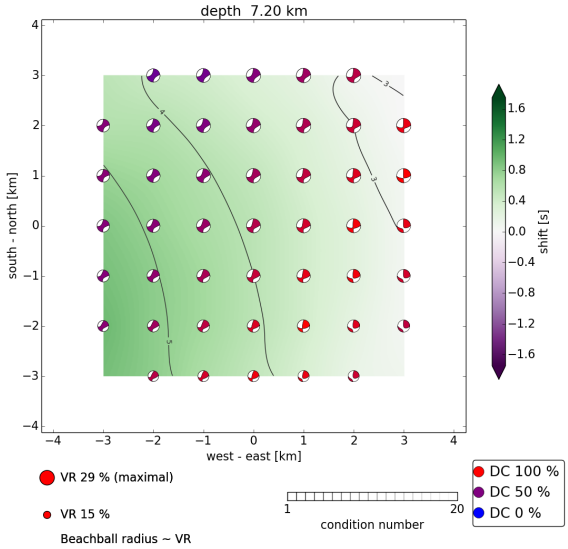

depth 7.2 km (other depths in the web version)

Calculation parameters

Grid-search over space

number of points:	630
horizontal step:	1000 m
vertical step:	1000 m
grid radius:	3.746 km
minimal depth:	1.000 km
maximal depth:	14.946 km

Grid-search over time

min:	-1.75 s (-35 samples)
max:	1.75 s (35 samples)
step:	0.07 s (1 samples)

Green's function calculation

Crustal model:	input/CH_catalog/crustal.dat
npts:	128
tl:	102.40
freq:	65
npts for inversion:	104

Sampling frequencies

Data sampling:	120.0 Hz, 200.0 Hz, 80.0 Hz, 100.0 Hz
Common sampling:	20.0 Hz
Decimate factor:	16 x
Sampling used:	1.2 Hz